PONTIFÍCIA UNIVERSIDADE CATÓLICA
DO RIO DE JANEIRO

Cíntia Aparecida Pires da Costa

MeV ion and keV electron irradiation effects on prebiotic materials: radiolysis and sputtering

Tese de Doutorado

Thesis presented to the Programa de Pós-Graduação em Física of PUC-Rio in partial fulfillment of the requirements for the degree of Doutor em Ciências - Física.

Advisor: Prof. Enio Frota da Silveira

Rio de Janeiro
September 2021

PONTIFÍCIA UNIVERSIDADE CATÓLICA
DO RIO DE JANEIRO

Cíntia Aparecida Pires da Costa

MeV ion and keV electron irradiation effects on prebiotic materials: radiolysis and sputtering

Thesis presented to the Programa de Pós-Graduação em Física of PUC-Rio in partial fulfillment of the requirements for the degree of Doutor em Ciências - Física. Approved by the Examination Committee:

Prof. Enio Frota da Silveira
Advisor
Departamento de Física - PUC-Rio

Dr. Hermann Rothard
Centre de Recherche sur les Ions, les Matériaux et la Photonique

Prof. Pedro Luis Grande
UFRGS

Prof. María Colín García
UNAM

Prof. Lucas Maurício Sigaud
UFF

Prof. Carla Göbel Burlamaqui de Mello
Departamento de Física - PUC-Rio

Rio de Janeiro, September 29th, 2021

Címtia Aparecida Pires da Costa

Received the title of Bachelor of Science degree in Physics and obtained her M.Sc. Degree in Physics from the Pontifícia Universidade Católica do Rio de Janeiro in 2014 and 2016.

Bibliographic data

da Costa, Cíntia Aparecida Pires

MeV ion and keV electron irradiation effects on prebiotic materials: radiolysis and sputtering / Cíntia Aparecida Pires da Costa; advisor: Enio Frota da Silveira – Rio de Janeiro: PUC, Departamento de Física, 2021.

v., 158 f : il. color. ; 30 cm

Tese (doutorado) – Pontifícia Universidade Católica do Rio de Janeiro, Departamento de Física, 2021.

Inclui referências bibliográficas.

1. Física – Tese. 2. Aminoácido; Feixes de íons; 3. Feixes de elétrons; FTIR; 4. CASINO; 5. Raios cósmicos I. da Silveira, Enio Frota. II. Pontifícia Universidade Católica do Rio de Janeiro. Departamento de Física. III. Título.

CDD: 530

To my nephew Miguel

Acknowledgments

To my advisor, professor Enio Frota da Silveira, for his guidance and support. Without him I would not have accomplished what I needed to reach this far. I guess, like Isaac Newton, I was lucky to have had a (literally) giant's shoulder to stand on.

To my family for all the unconditional support throughout my academic career. In particular, to my brother Lucas, and my parents Marlene and Elizeu.

To my dearest friends, Fernanda Abrantes, Lucianno Defaveri and Francisco Freitas for being my carioca family. In special, I would like to thank Lucianno for helping me countless times on revision of papers and part of the present thesis.

To my beloved friends Jean Pereira, and João Silveira for always being there for me, and especially for all the laughter during the most difficult times.

To my friends and colleagues at the Van de Graaff laboratory and in our research group. In particular, Pablo Oliveira, Vinicius Pessanha, Rodrigo Pereira, Rafael Martinez, Igor Ulrichsen, and Felipe Ptak for all the help and support. More than just working together, it was a great pleasure being around you.

To Lucas Sigaud, Allan Vieira, and Jade Barreto for being such good Zoom drinking buddies between the completion of chapters.

To the Van de Graaff Laboratory staff, especially Nilton Gomes, Sérgio Xavier, Edson Joaquim, and Suellen Tozetti for being so patient and helpful. Whithout your assistance, this work would not be possible.

To the professors, and the administrative staff of the Physics Department at PUC-Rio. Especially, Giza, Eduardo Rodrigues, Marcia Arjona, and Julinho (Malvino Garcia) for all their assistance.

To Lucas Simões, Rafael Sales and professor Luíz Mendes for the collaboration and hospitality, especially during the experiments at UFBA.

To Anne Bittencourt and Nathalia Carballo for keeping me (almost) sane during graduate years.

To Daniel Linhares for English revision in parts of this manuscript.

To the funding agencies CNPq and FAPERJ for the financial support that made this research possible. This study was financed in part by the Coordenação de Aperfeiçoamento de Pessoal de Nível Superior - Brasil (CAPES) - Finance Code 001.

Abstract

da Costa, Cíntia Aparecida Pires; da Silveira, Enio Frota (Advisor). **MeV ion and keV electron irradiation effects on prebiotic materials: radiolysis and sputtering**. Rio de Janeiro, 2021. 319p. PhD. Dissertation- Departamento de Física, Pontifícia Universidade Católica do Rio de Janeiro.

The presence of amino acids in comets and meteorites raises questions about how they have been formed in cosmic environments, as well as how long they can survive in outer space; radioresistance is essential information to predict half-lives and make advances on the origins of life studies. The main objective of the current work is to determine, via infrared spectrometry, destruction cross sections of common amino acids exposed to energetic ion and electron radiation. Before sample irradiation, valine vibrational band strengths and their infrared spectral dependence on temperature (10 – 400 K) were analyzed. Apparent destruction cross sections (σ_d^{ap}) and sputtering yields (Y_0) for glycine, valine and phenylalanine, irradiated by MeV H^+, He^+ and N^{q+} ions and keV electrons, were measured. From experimental data: i) an approximately linear dependence between the apparent destruction cross section and the electronic stopping power (S_e) is found: $\sigma_d^{ap} = \sigma_d + Y_0 / N_0 = a\, S_e^n$ (where n ~ 1) for MeV projectiles and for samples at room temperature; ii) σ_d^{ap} preliminary results relative to multi-charged nitrogen ion beams are discussed; and iii) destruction cross section of valine irradiated by keV electrons, as well as its dependence on incident beam energy, on sample thickness and on sample temperature are presented. As a theoretical contribution, the evolution of organic matter damage by charged projectiles, particularly for electron beams, the CASINO-extended model was developed. When compared to experimental results, the model predictions underestimate the damage caused by electron beams, evidence that sputtering and probably some sample characteristics (as crystallographic structure) are involved. As astrophysical implications, cosmic ray half-lives for valine and phenylalanine are estimated to be about 10 million years in the interstellar medium; solar wind half-life at 1 au from the Sun is ~ 3 days for glycine. Aiming to simulate realistic astrophysical materials bombarded by keV electrons, the half-life of valine embedded into water and CO_2 ices over a silicate substrate is also predicted.

Keywords

Amino acid; Ion beam; Electron beam; FTIR; CASINO; Cosmic rays.

Resumo

da Costa, Cíntia Aparecida Pires; da Silveira, Enio Frota (Orientador). **Efeitos induzidos pela irradiação com íons de MeV e elétrons de keV em materiais prebióticos: radiólise e sputtering**. Rio de Janeiro, 2021. 348p. PhD. Tese de Doutorado - Departamento de Física, Pontifícia Universidade Católica do Rio de Janeiro.

A presença de aminoácidos em cometas e meteoritos levanta questões sobre como estes foram formados em ambientes cósmicos, bem como de que maneira eles foram capazes de sobreviver no espaço sideral; radioresistência é uma informação essencial para prever meias-vidas e avançar os estudos sobre origens da vida. O principal objetivo deste trabalho é determinar, por meio de espectroscopia no infravermelho, as seções de choque de destruição de aminoácidos comuns expostos à radiação de íons e elétrons energéticos. As forças de banda vibracionais (*A-values*) e a dependência do espectro infravermelho com a temperatura da amostra (10 – 400 K) foram analisadas. Seções de choque de destruição aparente (σ_d^{ap}) e rendimentos de sputtering (Y_0) para glicina, valina e fenilalanina irradiadas por H^+, He^+ e N^{q+} íons de MeV e elétrons de keV foram medidos. Encontrou-se: i) uma dependência aproximadamente linear entre a seção de choque de destruição aparente e o poder de freamento eletrônico (S_e): $\sigma_d^{ap} = \sigma_d + Y_0 / N_0 = a\, S_e^n$ (onde n ~ 1) para projéteis de MeV e para amostras à temperatura ambiente; ii) resultados preliminares de σ_d^{ap} para feixes de nitrogênio multi-carregados; e iii) resultados de seção de choque de destruição de valina irradiada por elétrons de keV, bem como sua dependência com a energia de incidência do feixe, e com a espessura e temperatura da amostra. Como contribuição teórica, o modelo CASINO-estendido foi desenvolvido visando descrever a evolução da degradação de matéria orgânica por projéteis carregados, particularmente por feixes de elétrons. Comparadas aos resultados experimentais, as previsões do modelo subestimam o dano causado pelo feixe de elétrons, evidência de que efeitos de *sputtering* e provavelmente algumas características da amostra (como a estrutura cristalográfica) devem ser incluídos. Como implicações astrofísicas, meias-vidas para valina e fenilalanina irradiadas por raios cósmicos são estimadas em aproximadamente 10 milhões de anos no meio interestelar; da glicina, se irradiadas por vento solar a uma unidade astronômica do Sol, é ~ 3 dias. Visando simular materiais astrofísicos realistas bombardeados por elétrons de keV, a meia-vida de valina envolta por gelos de água e CO_2 e depositada sobre silicato é também prevista.

Palavras-chave

Aminoácido; Feixes de íons; Feixes de elétrons; FTIR; CASINO; Raios cósmicos.

Table of contents

"A scientist in his laboratory is not a mere technician: he is also a child confronting natural phenomena that impress him as though they were fairy tales."

Marie Skłodowska-Curie

1
Introduction

Degradation of organic material exposed to ionizing radiation has an enormous relevance in areas such as Medical Physics (Radiotherapy, production and application of radioisotopes), Radiological Security of nuclear plants and large accelerator laboratories, manned missions in the Solar System, and Astrochemistry (evolution of molecular species in the Universe). Although main lines concerning the interaction of energetic photons, electrons and ions with organic matter are under research since decades, specific information is still needed.

The focus of this work is in one of these specific systems: MeV ion and keV electron radiation impinging on prebiotic molecules. The scenario can be constrained as well, represented by the following question: what is the degradation rate of some common amino acids exposed to Solar Wind or to Galactic Cosmic Rays?

Indeed, the main amino acids (vital for living beings) and some other complex organic molecules (COMs) have been found in meteorites such as Murray, Murchison, Nogoya and Mokoia [1–3]. In particular, glycine (Gly) has been detected indirectly by the Stardust probe in dust traces of the comet 81P/Wild 2 [4], and directly, in considerable large quantities, in jets of the comet 67P/Churyumov-Gerasimenko by the Rosetta mission [5]. The detection of valine (Val) and phenylalanine (Phe) molecules has not been confirmed yet, but since these materials are present in meteorites, they might exist elsewhere in the outer space too. Moreover, if larger molecules such as PAHs (Polycyclic Aromatic Hydrocarbons) exist throughout diverse astronomical environments [6], the detection of amino acids in the interstellar medium is expected.

In space, those materials are exposed to several kinds of radiation. From an abiotic origin of life point of view, relevant questions appear, as: Does space radiation have a role in the synthesis of COMs? Is cosmic organic matter responsible for the existence of life as we know? Considering astronomical low temperature and pressure conditions, the "Chemistry of life" would not be able to occur spontaneously in these environments: some kind of catalyzer should be necessary.

The specific places where those materials are present are also very important. For instance, molecules within asteroids or comets are shielded from short-range radiation, being available then to be delivered in hospitable zones where more complex organic chemistry may happen until the development of life. Nevertheless, for this same example, such molecules could be exposed to radionuclide decay inside the considered celestial bodies [7–9]. Furthermore, the low albedo (dark gray) of these astrophysical specimens is probably related to the graphitization / carbonization of carbon-content material existing on their surfaces: ionizing radiation turns the condensed original material (e.g., CH_4, $HCONH_2$, CO_2) into carbon enriched compounds as polymeric C_nH_2 chains or tholins [10, 11].

It is significant, then, to explore how amino acids and analogous organics are affected by energetic ions and electrons, similar to those constituents of cosmic radiation, in order to estimate their radioresistance, and respective half-lives in astronomical environments.

1.1
Objectives

The main goals of the present work are:

(i) Determine glycine, valine and phenylalanine cross sections when these materials are irradiated by MeV ions and keV electrons.

(ii) Verify their cross section dependence on the beam stopping power, and discuss the respective effects of radiolysis and sputtering.

(iii) Study the projectile-material interaction, and the physical processes behind experimental results.

(iv) Estimate relevant parameters, such as A-values, sublimation rates, and half-lives, that might be useful for other research areas.

1.2

Manuscript structure

In Chapter 2, pertinent data reported in literature are briefly revised. Chapter 3 describes the experimental techniques employed at the current research, while the results are exhibited in Chapter 4. Chapter 5 presents a theoretical model developed for studying molecular degradation. In particular, it was employed for analyzing the interaction of keV electrons with materials composed by H, C, O and N (basic elements for organic matter). In Chapter 6 the experimental and theoretical results are discussed, as well as their possible implications. Finally, the main conclusions obtained are listed in Chapter 7.

2

Previous experimental research and objectives

In order to test radioresistance and applications in Radiotherapy and Astrochemistry connected with the origins of life, the degradation of organic materials by ionizing radiation has been object of vast literature. The following subsections only represent some selected experimental researches on this topic, relevant for the current work. They concern mainly different types of ionizing radiation able to degrade solid amino acids or similar organic compounds; a few gaseous examples are also presented. Information from irradiation with MeV ions and keV electrons are highlighted; afterwards, keV ion- and photon- induced degradation are shortly reported. The objectives of the current work are presented at the end of the chapter.

The radiolysis of amino acids has a vast literature. A selected number of publications or research in progress is listed below, Table 2.1, with the goal of giving the chronology of studies concerning MeV ion and keV electron irradiations with amino acids.

Table 2.1: Selected chronological summary of organic material studies.

Year	Material	Beam	Phenomenum	Who/Where
1971	Amino acids	-	Presence in meteorite	Murchison
1979	Tholins	-	Organic material in space	Carl Sagan
1980	Val	12 MeV S ions	Ion induced desorption	Erlangen Univ.
1988	Val	78 MeV I ions	Ion induced desorption	Uppsala Univ.
1992	Phe	MeV C ions	Ion induced desorption	PUC-Rio
1997	organics	Cosmic rays	Chemical evolution	Strazzulla
2009	Gly	-	Detected in a comet	Stardust
2012	Gly, Ala , Phe	MeV H+	Decomposition	Gerakines et al.
2013	Gly	MeV H+	Decomposition	PUC-Rio
2014	Gly	MeV heavy ions	Decomposition	GANIL, France
2014	Gly	keV electrons	Decomposition	Maté et al.
2016	Val	MeV ions	Decomposition	PUC-Rio
2019	Gly	keV electrons	Decomposition	PUC-Rio
2020	Val	MeV heavy ions	Decomposition	PUC-Rio/GANIL
2021	Phe	MeV ions	Decomposition - submitted	PUC-Rio
2021	Val	keV electrons	Decomposition - submitted	PUC-Rio
2021	Ala	keV electrons	Decomposition - in progress	PUC-Rio

2.1

MeV ions

Dück et al. (1980) [12] studied valine desorption induced by ^{16}O and ^{32}S ion beams in the 8 – 40 MeV energy range. They measured the dependence of desorbed secondary ion yields on incident energy and found out that: i) the desorbed ions increase with the increasing of the stopping power, and ii) the ratios between desorption yields of distinct ionic species from the same surface are not altered. Few years later, Salehpour et al. (1988) [13] measured valine bombarded by atomic and molecular MeV ions (C^+, O^+, Ar^+, C_2^+, O_2^+, CO^+, CO_2^+, CH^+, CH_3^+, CF^+, $C_3F_5^+$, and $C_4F_7^+$). They observed that desorption ion yields increase with the square of the projectile stopping power. In a similar research, Barros Leite et al. (1992) [14] measured relative yields of positive and negative secondary ions of phenylalanine bombarded by atomic and molecular MeV ion beams (C^+, O^+, CO^+, and CO_2^+). Differently from the previous studies, they reported desorption yields roughly proportional to the third power of the beam stopping power.

The damage of both valine and bovine insulin with 90 MeV $^{127}I^{14+}$ ions impinging on the samples was studied by Salehpour et al. (1984) [15] using time-of-flight mass spectrometry as the analytical technique. For positive and negative valine secondary ions, the measured damage cross sections are $(6.8 \pm 1.8) \times 10^{-13}$ cm^2 and $(4.4 \pm 1.5) \times 10^{-13}$ cm^2, respectively. Furthermore, the damage cross section for bovine insulin was found to be greater than the valine one (by a factor of ~ 7 for positive secondary ions). The finding was attributed to the fact that the molecular species have different sizes (valine is smaller), and when a piece of the bovine insulin molecule is damaged, it ceases to contribute to the characteristic peaks in the mass spectrum. In the current context, we would say that the sputtering yield decreases because the insulin concentration decreases with fluence in the sample surface.

Gerakines et al. (2012) [16] irradiated glycine, alanine, and phenylalanine (pure and mixed with water) with 0.8 MeV H^+ at 15, 100, and 140 K. They reported destruction cross section values of $(1.2 - 3.9) \times 10^{-15}$ cm^2 per proton impact. Except for pure phenylalanine, results show that cross sections at 15 K are about a factor 2 higher than the ones at 140 K. Concerning the irradiation of mixtures, they showed that H_2O + Gly (8.7:1), and H_2O + Phe (26:1) present higher destruction cross sections than the pure amino acids; while pure alanine behaves oppositely when compared to H_2O + Ala (11:1). For the cold DISM (Diffuse Interstellar Medium), they predicted half-lives from 0.6 to 0.96 million years for these compounds. In contrast, Pilling et al. (2013) [17] bombarded two different crystalline forms of glycine (α and β) with 1.0 MeV H^+ at 300 K. They reported that for α and β glycine, the respective destruction cross sections are 2.5 x 10^{-14} and 0.5 x 10^{-14} cm^2, with half-lives around 9 x 10^5 and 4 x 10^6 years, respectively; estimates of half-lives at the Earth's orbit show that cross sections are ten times lower than those in the DISM. The authors claim that, because of its greater half-life, crystalline β-glycine might be the most likely structure to form peptides in primitive Earth. Portugal et al. (2014) [18] also irradiated α-glycine at 14 and 300 K with 46 MeV $^{58}Ni^{11+}$. They reported the appearance of the daughter species OCN^-, CO, CO_2 and CN^-, at 14 K, and the possible occurrence of peptide bond formation during irradiation. Dissociation cross sections reported are huge: 3.4 x 10^{-13} cm^2 for samples at room temperature, and 2.4 x 10^{-12} cm^2 for cold glycine. For temperatures of 300 and 14 K, they predicted half-lives of 7.8 and 2.8 thousand years for the interstellar medium (ISM), and 0.84 and 3.6 thousand years for the solar system (SS), respectively.

The degradation at low temperature of the nucleobase adenine by MeV heavy ion beams was studied by Vignoli Muniz et al. (2017) [19]. The authors determined a power law relationship between the destruction cross section, σ_d, and the electronic stopping power, S_e: $\sigma_d \propto S_e^{1.17}$. The half-life of solid adenine in the ISM was estimated to be around 10 million years.

2.2
keV electrons

Howitt (1974) [20] irradiated L-valine and adenosine by electrons with energy between 200 and 650 keV. They measured damage cross sections of (1.6 – 3.2) x 10^{-17} cm^2 and (2.7 – 5.7) x 10^{-18} cm^2 for valine and adenosine, respectively. In both cases, the cross section values increase when the energy of the incident beam decreases; ionizing cross sections were found to be one order of magnitude lower than the damage ones. They stated that this difference between ionizing and damage cross sections might be misleading, suggesting the existence of intense secondary ionization during measurements and proposed that the damage cross section should be taken as an average of all the events that degrade the material.

Barnett et al. (2012) [21] studied the damage depth and induced chemistry by 0.1 – 2 keV electron radiation of the polycyclic aromatic hydrocarbon (PAH) pyrene ($C_{16}H_{10}$) embedded in water ice. UV-vis spectroscopy was employed to analyze quantitatively the endurance of the organic material. Measurements in function of sample thickness were performed to better understand the damage caused by the beam with respect to the sample depth. They observed a linear dependence between the damaged length and the deposited energy of about 110 nm keV^{-1}, which is reported to be 100% higher than predictions by Monte Carlo simulations with the CASINO code [22]. They concluded that simulations underestimate the damage caused by electrons with energies below 2 keV.

Glycine, at 20 K, irradiated by 2 keV electrons and 120 – 200 nm UV photons was investigated by Maté et al. (2014) [23]. Electron irradiation induced the formation of CO_2, CO and possibly OCN^-. While, UV radiation produced CO_2 and methylamine product species. They concluded that UV photons are more efficient to degrade glycine than 2 keV electrons, and that the use of keV electrons to mimic effects of cosmic rays should be taken with caution because of the low penetration range of electrons in the samples of astrophysical interest (analogues of interstellar grains).

Pilling et al. (2014) [24] studied the decomposition of α and β glycine, at 14 and 300 K, by 2 keV electrons. Dissociation cross sections were found to be five times higher for cold samples than for those at room temperature, but no relevant differences were observed in the degradation of the two crystalline forms. The reported cross sections are (3.5 – 20) x 10^{-17} cm^2. Later, Maté et al. (2015) [25] measured as well the destruction of glycine by 2 keV electrons for samples at different temperatures (20 – 300 K). They noticed that destruction cross sections for measurements of samples with temperatures below 90 K were about the same, but a factor of 2 higher for the sample at 300 K, which was the opposite of the Pilling et al. (2014) [24] finding. Maté et al. (2015) [25] claim that keV electrons could be used to simulate effects of cosmic rays with the condition that the sample is completely processed during measurements (so the penetration depth would not be an issue). Additionally to the previously reported products, they have included the presence of CN^- and perhaps amide bands I to III. Maté et al. (2015) [25] also shielded glycine samples with 150 nm of water ice, and concluded (contrarily to Barnett et al. (2012) [21]) that the CASINO code predictions describe well the electron penetration ranges. They estimated half-lives for several environments, and stated that the possibility of primeval glycine existing in present solar system bodies is unlikely. They obtained destruction cross sections in the (10 – 18) x 10^{-16} cm^2 range.

Souza-Corrêa et al. (2019) [26] measured the dissociation of α-glycine, at 40 – 300 K, when bombarded by 1 keV electrons. They reported similar behaviors to Maté et al. (2015) [25]: destruction cross section values are alike for samples below 80 K, and increase by a factor ~ 20 at room temperature. They measured cross section values between the ones observed by Pilling et al. (2014) [24] and Maté et al. (2015) [25], and reported the presence of the daughter species OCN^-, CO, and amides II and III.

The degradation of adenine, at 10 K, irradiated by 5 keV electrons was analyzed by Evans et al. (2011) [27]. They measured the destruction cross section as being (1.1 ± 0.3) x 10^{-16} cm^2, and estimated the adenine half-life to be about six million years within dense interstellar clouds.

2.3
Additional ionizing beams

Foti et al. (1991a, b) [28, 29] irradiated glycine with 3 keV He projectiles. They reported the possibility of selective sputtering yields of glycine products because dissimilar decay rates of the infrared bands representing the vibrations of C-H, COO^-, and NH_3^+ species were observed; since the latter was the one with the highest yield, they suggested that irradiation was responsible for carbonizing the sample. Huang et al. (1998a, b) [30, 31] reached the same conclusions after degrading glycine with 30 keV N and 8 keV Ar ions. They noticed the desorption of the species H_2, COO, and NH_3, which suggested that the dark material remaining after irradiation was result of carbonization of the sample surface.

Huang et al. (1998c) [32] also emphasize that glycine bombarded with keV ions shows higher desorption yields, when compared to other experiments of irradiation, due to the dominance of nuclear stopping power over the electronic one in this range of energy. In turn, Meshitsuka et al. (1964) [33] employed ^{60}Co γ-rays to destroy glycine at room temperature. Similarly, they proposed that carbon enrichment occurred during irradiation, because the species CO_2, NH_3, and H_2 were released in gas form.

Lago et al. (2004) [34] used UV photons of ~ 21 eV to dissociate gaseous glycine, L-alanine, L-proline and L-valine. For the four amino acids analyzed, they reported that neutral COOH was the most common fragment produced; in contrast, the most abundant ionic fragments observed were CH_2O^+ or NO^+ for glycine, $C_2NH_6^+$ or CO_2^+ for alanine, $C_4H_8N^+$ for proline, and $C_4H_{10}N^+$ for valine. They also concluded that mass spectra, of photon induced dissociation, of these materials agree with previous data regarding impact of 70 eV electrons [35, 36].

Pure and water-mixed glycine, at 30 K, irradiated by X-rays coming out from the beam line TEMPO, at the SOLEIL synchrotron, were analyzed by Pernet et al. (2013) [37]. They observed that, at first, glycine excitation or ionization would occur; then precursor molecules are dissociated into CH_2NH_2 and COOH groups, followed by the formation of CO_2 (by the detaching of H from COOH), and the formation of CH_3NH_2 (from the H attaching to the CH_2NH_2). In turn, the degradation of these products formed HCN, CH_2NH, and CO.

Cataldo et al. (2011) [38], aiming to simulate the decay of radionuclides inside asteroids and comets (depth > 20 m), reported the γ-radiolysis of the 20 basic amino acids existing in living beings. They predicted that the studied molecules are able to survive radiation doses up to 3 MGy, and state that this finding agrees with the presence of amino acids in meteorites.

2.4
Objectives

For MeV ions, one of the goals of the present work is to thoroughly investigate the destruction cross section dependence on the electronic stopping power for three amino acids: glycine, valine and phenylalanine. Because of its simplicity, glycine is the most likely amino acid to be found in the outer space and the most studied in literature; valine was chosen because it is another light amino acid, has chiral properties and was identified in meteorites. Phenylalanine contains a phenyl group (a benzene ring) and could introduce new features in the degradation analysis.

Concerning keV electrons, valine is used as typical bioorganic material. The analysis of its radiolysis helps to understand why data on literature exhibit cross section values so disperse. With this in mind, the cross section dependences on projectile energy, on target thickness, on crystalline state and on temperature are all evaluated. A theoretical model is also developed and proposed to analyze the interaction of keV electrons with organic compounds.

Since all amino acids, except glycine, present chirality properties, studies with polarized light are very relevant; for example, to analyze the radioracemization resistance and the enantiomeric enrichment in meteorites. However, this is beyond the scope of the present work.

3
Materials and Methods

Information about the analyzed amino acids, and the methods used to perform the experiments are presented. Specifically, it is described: i) pertinent properties of glycine, valine and phenylalanine; ii) how the samples have been produced; iii) the Fourier Transform Infrared (FTIR) spectroscopy analytical technique; and iv) details about how the ion and electron beams have been prepared for the irradiations.

3.1
Amino acids properties

Among the hundreds of amino acids known, there are 20 of them with vital biological importance (existing in proteins and living cells [39]). They are formed by a standard structure of a central or chiral carbon (the α-carbon) simultaneously linked to an amine group, a hydrogen atom, a carboxylic acid group, and a side chain R, Fig. 3.1(a). The lateral R chain is the component that distinguishes the amino acid species. For Gly, R is just another hydrogen atom, while for Val or Phe, R is an isopropyl group or a phenylpropanoic group, respectively – Fig. 3.1(b).

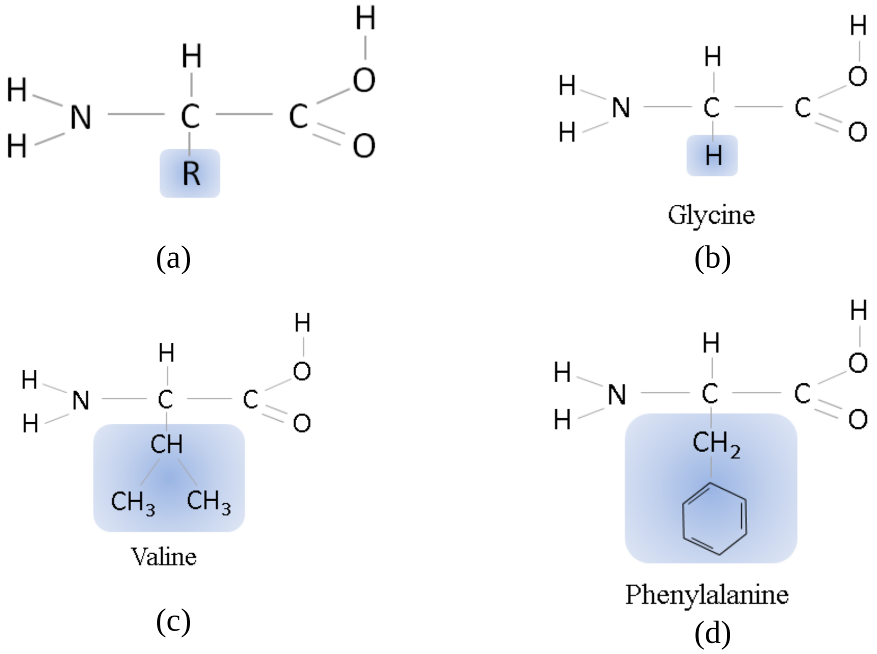

(a) (b)

(c) (d)

Figure 3.1: (a) Amino acids basic structure. Schematic structures of: (b) glycine, (c) valine, and (d) phenylalanine with highlighted side chains.

Glycine, valine and phenylalanine are amino acids necessary to life as we know. Val and Phe are essential amino acids, meaning they need to be ingested by the living organism, while glycine can be synthesized by its own cells. Gly and Val are classified as aliphatic and apolar, while Phe has an aromatic ring and hydrophobic characteristics [40]. In the solid sample film, the molecules of these amino acids interact by London forces (induced dipoles). This happens due to the deformation of electronic clouds of each molecule when they are close to one another; their electrospheres repel themselves, grouping electrons on a specific side of the molecule, consequently leaving the opposite side positive [41], see schematic representation in Fig. 3.2(a). If a proton migrates from the carboxyl to the amine group, the molecule is then called a zwitterion [40]; see Fig. 3.2(b) for valine as an example, which is probably the more stable molecular configuration in the films produced.

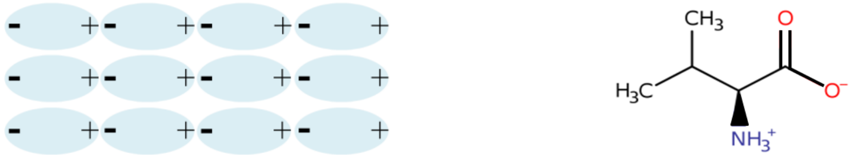

(a) (b)

Figure 3.2: (a) Schematic drawing of induced dipoles in a solid. (b) Valine in zwitterionic form. Notice that when the hydrogen migrates, the dipole stops being temporary (induced) to become permanent.

Gly is the only non-chiral amino acid. Val and Phe have chirality properties, though there is no significant distinction between their degradation when bombarded by MeV ions [42]. In the current work, the FTIR technique was not used for identification of materials, but as a means to follow the evolution of molecular populations in function of beam fluences, via Beer-Lambert Law.

Salam phase transitions

In 1991, the Nobel Prize laureate Abdus Salam suggested that D-amino acids might change “spontaneously” their molecular configurations into L-amino acid ones. The suggestion is based on Bose-Einstein condensates and on parity violation of electroweak force in phase transitions and would explain why life uses only the L-enatiomers as constituints of peptide chains and, therefore, of proteins [43, 44]. Since then, the subject has been the focus of academic debate

[45]. Valine and alanine have been chosen for most experiments and theoretical calculations. The prediction is that the transition would occur below the critical temperature of 250 to 270 K.

Table 3.1 displays the main characteristic absorption bands and their possible assignments for glycine, valine, and phenylalanine.

Table 3.1: Glycine, valine and phenylanine selected attribution bands.

Gly		**Val**		**Phe**	
Wavenumber (cm^{-1})	**Assignment**	**Wavenumber (cm^{-1})**	**Assignment**	**Wavenumber (cm^{-1})**	**Assignment**[f]
3160	$\nu_{as}\ NH_3$ [a,b,c]	3150, 3050	$\nu_{as}\ NH_3^+$	3293, 3064	ν OH
3004	$\nu_{as}\ CH_2$ [b,c]	2960, 2940	$\nu_{as}\ CH_3^+$	3030	$\varphi\ \nu$ CH
2969	$\nu_s\ CH_2$ [c]	2880, 2850	$\nu_{as}\ CH_3^+$	2960 sh	Overtones and combination
2893	$\nu_s\ NH_3^+$ [b]	2109	$\delta CH_3 + \rho\ NH_2$ [d]	2925 sh	Overtones and combination
2794	$\nu\ NH_3$, $\nu\ CH_2$ [a]	1640	$\nu\ CO_2^-$ [e]	2885 sh	Overtones and combination
2610	$\nu_{as}\ NH_3^+$, ν CN, $\nu\ CH_2$ [a,b]	1520, 1430, 1390	$\nu_s\ COO^+$	2858 sh	Overtones and combination
2526	$\nu\ NH_3$, $\nu\ CH_2$ [a]	1340, 1320	COO^+/CO	2796 sh	Overtones and combination
2124	$\nu_{as}\ NH_3^+$, $\tau\ NH_3^+$ [b]	775	$\delta\ CO_2$	2715 sh	Overtones and combination
1333	ν CC, $\omega\ CH_2$, $\omega\ NH_3$ [a,b,c]			1310 sh	$\omega\ CH_2$
1132	$\rho\ NH_3$ [a,c]			1261	$\delta\ CH_2$
1113	ρ NH3 + [b,c]			912	ν_s CC
1034	ν CN [a,c]				

[a] Maté et al. (2011) [46]; [b] Guan et al. (2010) [47]; [c] Holtom et al. (2005) [48]; [d] Kumar [49]; [e] Façanha Filho et al. (2008) [50]; [f] Mejía et al. (2021) [51].

ν = stretch, δ= bend, ω = wag, τ = torsion, ρ = rock, s = symmetric, as = asymmetric, φ = phenyl ring; sh = shoulder.

3.2

Sample preparation

Two techniques of samples production were employed in the present work, each one with its specific purpose. On the one hand, the main method, vacuum deposition, was used for the majority of the cases, since it is an easy way to produce large quantities of samples and to control film thicknesses. On the other hand, drop casting was only performed for valine samples, in order to compare data acquired in different laboratories. Infrared spectroscopy is applied in sample quality control.

3.2.1

Vacuum deposition

Deposition of amino acids films was performed onto IR transparent ZnSe or KBr substrates. Figure 3.3 shows how the selected material (powder of glycine, valine or phenylalanine), purchased from Sigma Aldrich – purity > 98%, are placed in a molybdenum boat of an Edwards thermal evaporator model E306.

The residual gas in the deposition chamber, Fig. 3.3 (a), is pumped down to pressures of ~ 10^{-6} torr; a current of ~ 30 A flows through the Mo boat, Fig. 3.3 (b), which warms the amino acid. The sublimated material condensates at the substrate surface facing the Mo boat, Fig. 3.3(c). The substrate holder accepts up to 21 circular 13 mm diameter disks; this set-up provides a nearly isotropic deposition of films (variations within 20% in sample thickness).

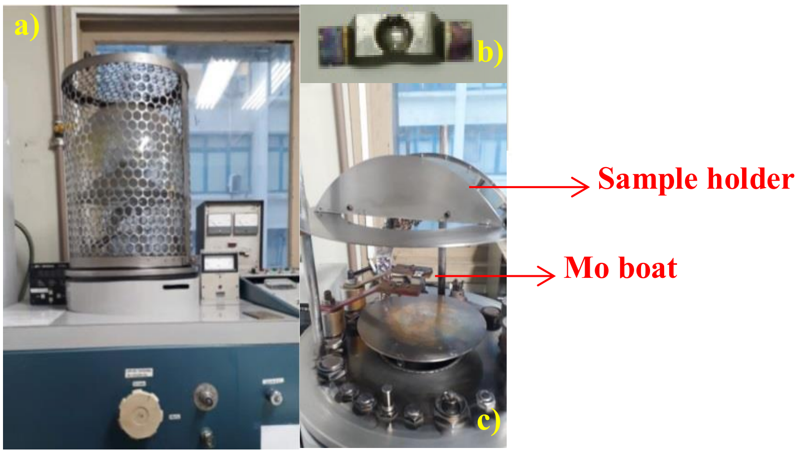

Figura 3.3: (a) Edwards E306 evaporation system. (b) Molibdenum boat where the amino acids are placed. (c) Semi-disc that supports the substrates.

3.2.2

Drop casting

The amino acid valine was dissolved in a mixture of water (40%) and ethanol (60%) until complete homogeneity, $C \approx 0.054$ g/mol. Drops of this solution were deposited over a ZnSe substrate, which, in turn, was placed above a hot plate at

100 °C in order to evaporate the solvent, Fig. 3.4. KBr substrates are not suitable for this technique, since this salt is highly hygroscopic.

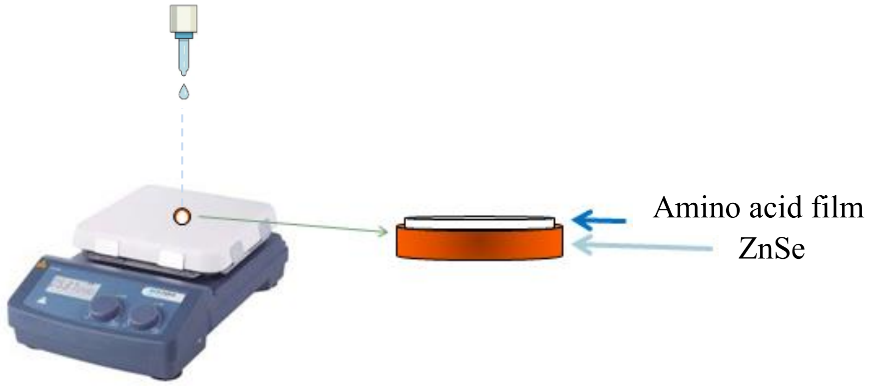

Figura 3.4: Representation of valine solution deposition into ZnSe substrate.

3.3

Sample characterization by infrared spectroscopy

The sample analysis was followed by infrared spectroscopy in transmission mode by a JASCO-4200 spectrometer, Fig. 3.5 (a), which employs a Michelson interferometer. A source of IR polychromatic light (High-intensity ceramic source for the present equipment) impinges on a beam splitter, which ideally reflects 50% of the light to a moving mirror and transmits the other 50% to a fixed mirror, Fig. 3.5 (b). The combined light of both reflection mirrors crosses the sample, and the detector measures the transmitted light (the light that is not absorbed by the sample); the optical path difference between the arms of the interferometer generates an interference pattern.

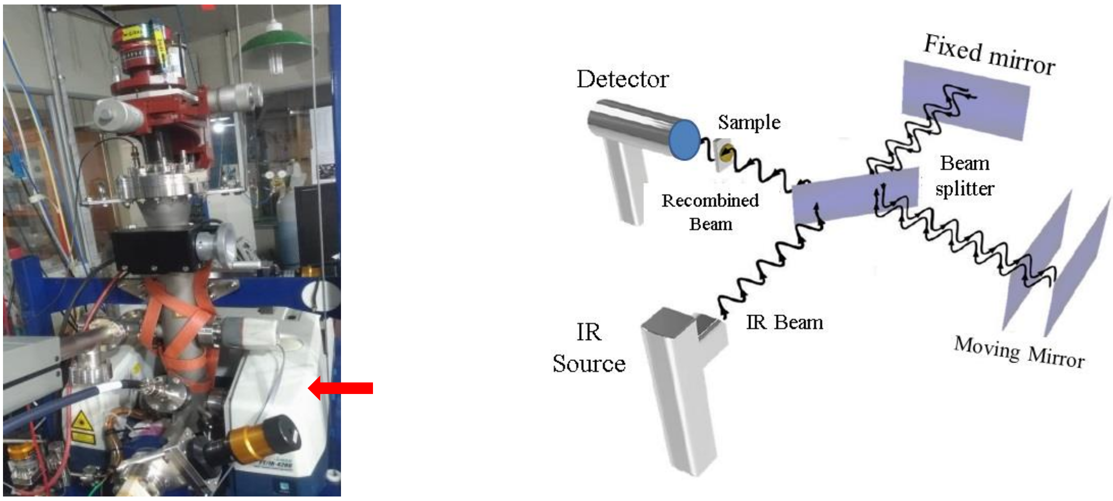

Figura 3.5: (a) Infrared spectrometer coupled to the analyzing chamber. (b) Schematic drawing of the Michelson interferometer inside the spectrometer.

Since one of the mirrors moves, the final interferogram is the sum of the interference patterns obtained for several monochromatic light frequencies. The Fourier transform of this interferogram, which results from the path differences (steps of the mirror), is the infrared spectrum of the material [52].

The IR technique has the restriction of only being useful to analyze materials with non-null dipole moment, or the ones that have an induced dipole moment. The radiation energy at Mid-IR (4000-400 cm^{-1}) corresponds to the difference between the ground state and the first excited state of the vibrational modes of many organic materials with covalent bonds [53].

Figures 3.6 (a) and (b) are examples of IR spectra of valine prepared by vacuum deposition and drop casting, respectively, as described in Section 3.2.

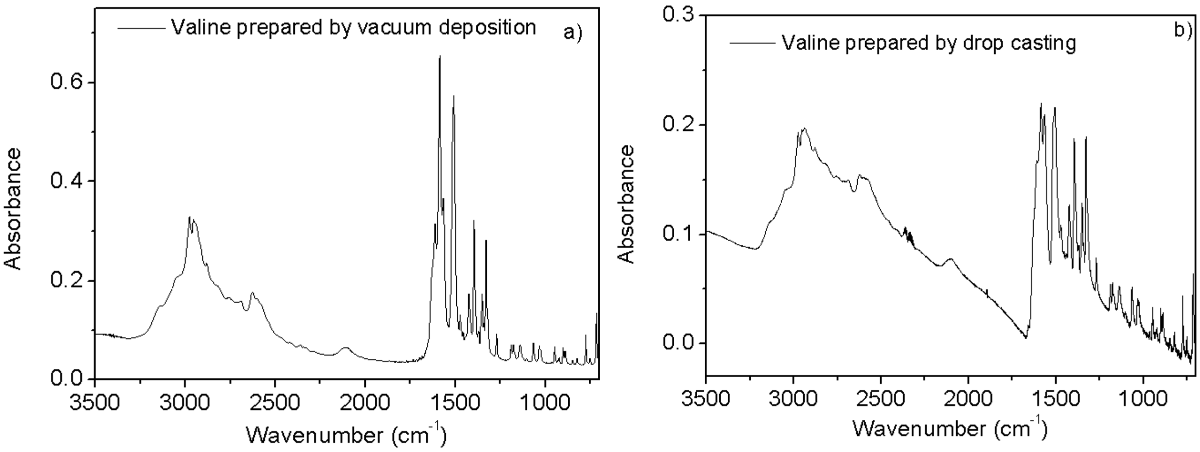

Figure 3.6: Infrared spectra of valine prepared by (a) vacuum deposition, and (b) drop casting.

The main differences of spectra in Fig. 3.6 lay on band heights and broadnesses, which indicate that each method produces samples at slightly distinct crystalline states. In Fig. 3.6 (b) there is a peak of gaseous CO_2, ~ 2350 cm^{-1}, present in the air during spectrum acquisition.

3.4
MeV ions

The ionic beams employed in the present work were obtained by a Van de Graaff generator, model KN4000 – High Voltage Engineering Corporation, able to reach high voltages, up to 4 MV, in an electrode charged by an insulator belt (schematic drawing of beam line at PUC-Rio is shown in Fig. 3.7(a)). The generator is equipped with a gas injection system with four bottles at ~ 300 psi of different gases (usually H_2 in two of them, He and N_2) for the production of ion beams. This system inserts the selected gas into an ion source bulb, where electric fields that oscillate at the radiofrequency range ionize the gas. Base residual pressure inside the ion acceleration channel is usually around 1 x 10^{-6} torr, so that a small leak of ionized gas is needed to create the desired beam; in general, working pressure values vary between 2 – 5 10^{-6} torr at the accelerator (at the analyzing chamber pressures are lower, see Section 3.4.1).

After that, the acceleration potential is designated and set at the high voltage terminal of the acceleration tube, fixing the ion energy and velocity. The ions are vertically accelerated, and at the end of the vertical pipeline there is a metallic grid (connected to an ammeter), and KBr pellets glued on a window glass - flange, which is monitored by a camera; so, it is possible to measure the beam current and observe its intensity and profile (since KBr fluoresces when it is hit by the ions). Remote controls are used to optimize the beam: i) *Beam source*, up to 7.5 kV, generates a potential difference to extract the ions from the created plasm inside the ion source; ii) *Source focus*, up to 30 kV, focuses the beam at the entrance of the accelerating tube; and iii) *Tube focus*, up to 40 kV, focuses the accelerated ions inside the tube (striped region on Fig. 3.7).

Since the ion source simultaneously produces several ionic species, a 90° analyzing magnet is employed to choose the wanted beam (by selecting the charge and momentum of the projectile). Then, a second magnet leads the beam to the FTIR research line.

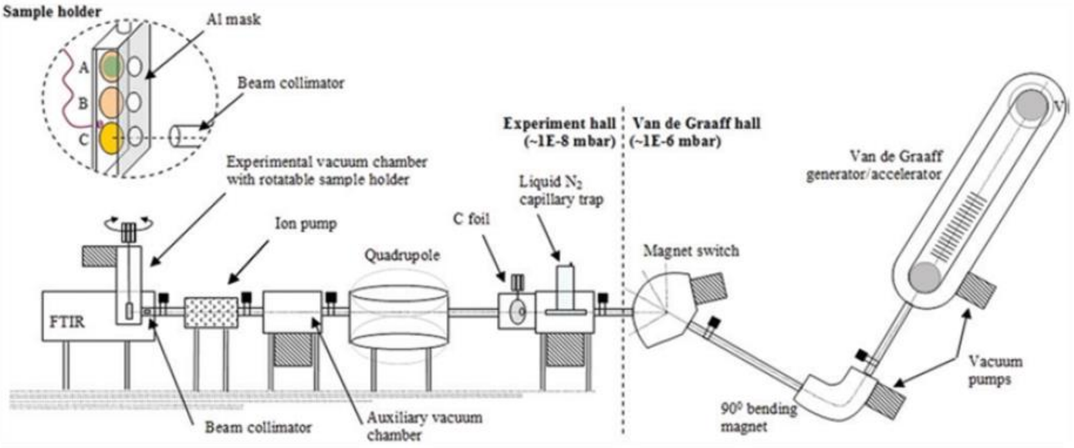

Figura 3.7: Illustration of the FTIR beam line connected to the Van de Graaff accelerator at PUC-Rio, adapted from Pilling et al. (2013) [17].

3.5
keV electrons

Electron beams were produced by an electron gun, Kimball Physics FRA-2X1-2, Fig. 3.8 In order to obtain approximately constant fluxes, the electron gun was operated in the Emission Current Control (ECC) mode.

Figura 3.8: Electron guns, Kimball Physics FRA-2X1-2.

Figure 3.9 presents the circuit that composes the electron gun. Beams are produced by thermionic emission of electrons. A tantalum cathode is connected to a tungsten filament, through which a current flows due to the potential difference V_{ES}. The electrons ejected from the filament are then accelerated by the potential difference between the cathode and the anode. The grid, that has a potential V_{VG} varying from 0 – 100 V in relation to the cathode, is able to generate an electric field in order to deflect the electrons trajectories, focusing the beam on the aimed spot. As the target, the filament is at a V_{EE} potential in relation to the ground, so the voltage source of the electron gun defines the energy of the incident beam on the sample surface. The beam shape is expected to have a Gaussian profile, but it is large enough to irradiate the sample almost homogeneously; 0.26 and ~ 0.5 cm^2 being the irradiated sample area and the beam spot area, respectively. However, due to the incidence at 40° with the target's normal, the flux is reduced by a factor of cos(40°).

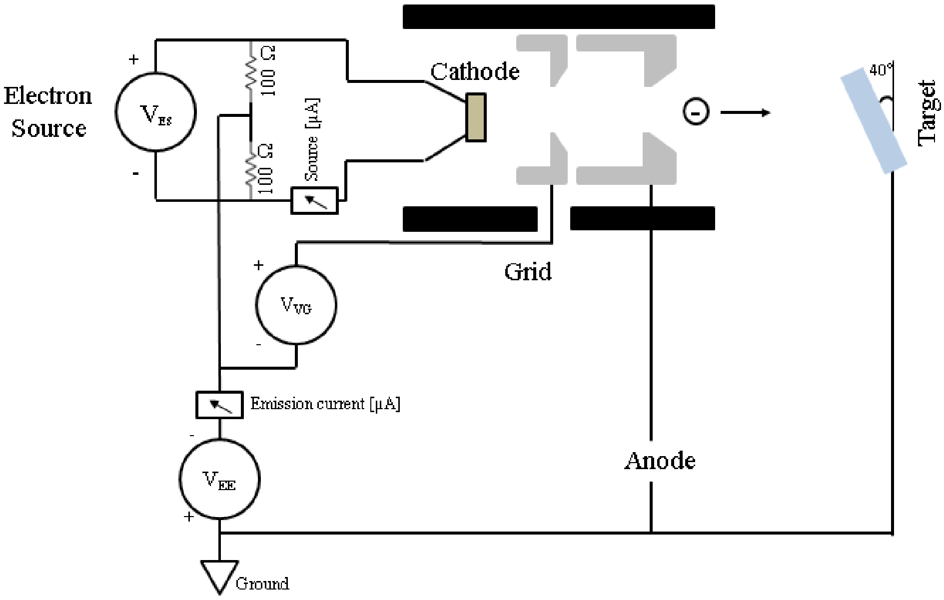

Figura 3.9: Kimball Physics electron gun schematic circuit.

keV electron and MeV ion beam fluences were measured using the relation of Eqs. (3.1) (a) and (b), respectively:

$$F = \phi t, \tag{3.1}$$

$$F = \frac{i}{eA} t, \tag{3.1a}$$

$$F = \frac{Q}{eA}, \tag{3.1b}$$

where ϕ is the beam flux, t the irradiation time, i the beam current, ***e*** the electron charge, Q the integrated charge during irradiation, and A the sample irradiated area.

For the ion beams, A = 0.95 cm^2, and the integrated charge was measured by a digital current integrator (ORTEC 439). A sweeping system, provided by an electromagnet, guarantees the uniform irradiation of ionic projectiles. Calibrations are performed at the beginning of experiments, when the beam hits the Faraday cup and a collimator ring (both connected to current integrators). Even if the beam currents provided by the Van de Graaff accelerator are not constant, the ratio between the number of ions impinging on the FC and on the reference collimator does not vary too much during long-lasting experiments; this is the reason why it is better to calculate fluence with Eq. (3.1b).

For the keV electron beams, fluence can be easily determined since the current furnished by the electron gun is very stable; the work current is fixed (usually around 30 nA), and the exposure time and the bombarded area are known (a collimator masks the sample). It is however necessary to control the secondary electron emission from the collimator, FC and sample.

3.6
Analysis chamber

The FTIR analysis chamber is the destination of one of the ion beam transport lines connected to the switching magnet. In order to get 10^{-9} mbar in this ultra-high vacuum (UHV) chamber, one dry mechanical (without oil), two turbomolecular and one ionic pumps are responsible for the pumping down system. However, working pressures are typically in the lower 10^{-7} mbar due to frequent openings and two ZnSe windows, fixed with o-ring gaskets, where the FTIR spectrometer is coupled. The chamber, represented in Fig. 3.8, has glass windows to help beam alignment (when it is possible), and feedthrough outlets to connect cables to measure beam current.

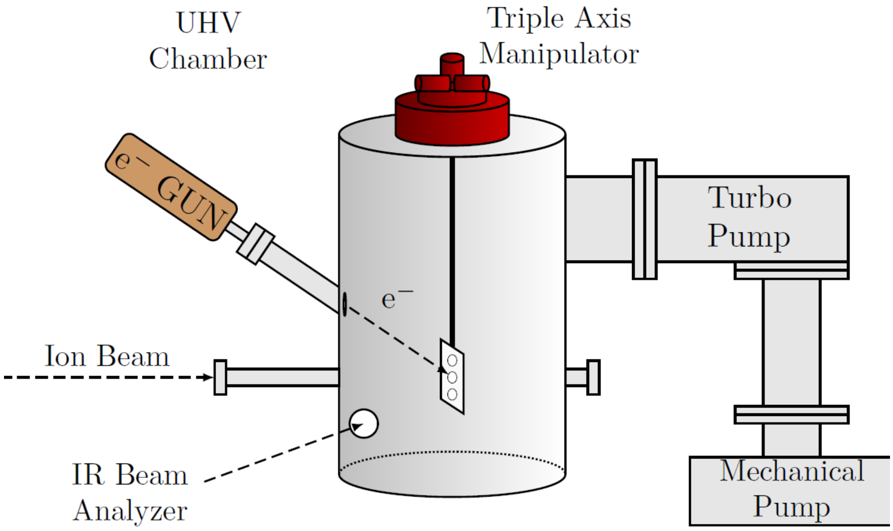

Figura 3.10: Schematic drawing of UHV analyzing chamber [54].

As shown in Figs. 3.11 (a) and (b), this chamber supports two alternative sample holders for experiments at room and cryogenic temperatures, respectively. The former, as depicted in Fig. 3.10, has its own micrometer system in three axes to centralize the sample at the best position for irradiation and IR characterization. It also possess slots for three samples, but one was used to place a Faraday cup (FC) to measure the beam current impinging on the sample during measurements. This sample holder is able to turn 360°, though only 90° rotation is necessary to alternate, back and forth, exposition to ionizing projectiles and to the analytical infrared beam. Both beams are expected to be aligned at the center of the sample, the center of the IR windows and the center of the ion beam port. The FC is located at the lateral of the sample holder, and it is coupled to a rotating flange; this is actually the case for MeV ions from the Van de Graaff accelerator, where the incidence is normal. For the keV electron beam (with 40° incidence), the FC is placed at the sample spot, Fig. 3.11 (c); this set-up is not practical because it implies opening the vacuum system at least twice for each experiment, one for measuring and calibrating beam current in the FC, and another for placing the sample.

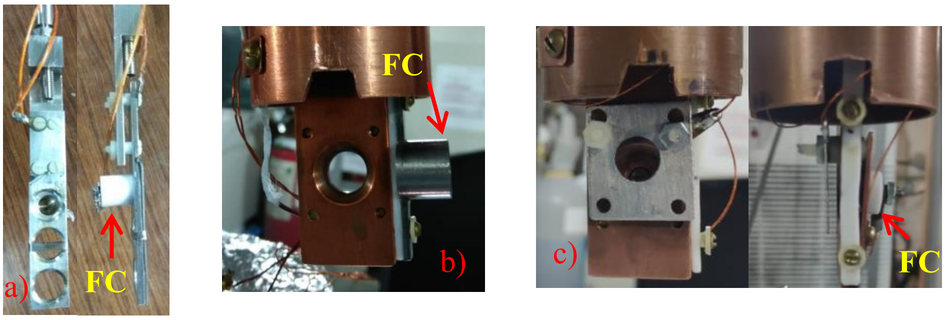

Figure 3.11: (a) Sample holder for measurements at room temperature: front and lateral view – the Faraday cup occupies one of the sample positions. Sample holder for measurements at cryogenic temperatures: (b) for irradiation with ions (normal incidence – FC on the lateral), and (c) for irradiation with electrons (40° incidence – FC placed on the sample site for calibration with the reference isolated plate).

To minimize the emission of secondary electrons, measurements with MeV ions and keV electrons (for cold samples) were biased with +90 V and +70 V, respectively; samples irradiated at 300 K by keV electrons were bombarded without any polarization. A grounded metallic grid, ~ 80% transmission, was also placed above the film samples bombarded with keV electrons at 300 K in order to avoid charge accumulation at the target surface (although experiments with and without the grid yielded the same degradation results).

4

Results

In this chapter, the obtained experimental results are presented. Data cover distinct beams (ion/electron, energy, current and charge state), as well as several sample characteristics (amino acid species, crystalline state, thickness, and temperature).

4.1

Sample characterization

4.1.1

Amino acid’s band strength (A-value)

4.1.1.1

Valine

Six L-valine films with distinct thicknesses were prepared by vacuum deposition onto ZnSe substrates (see section 3.2.1) and characterized by infrared spectroscopy at 1 atm and room temperature. Figure 4.1 shows the obtained spectra.

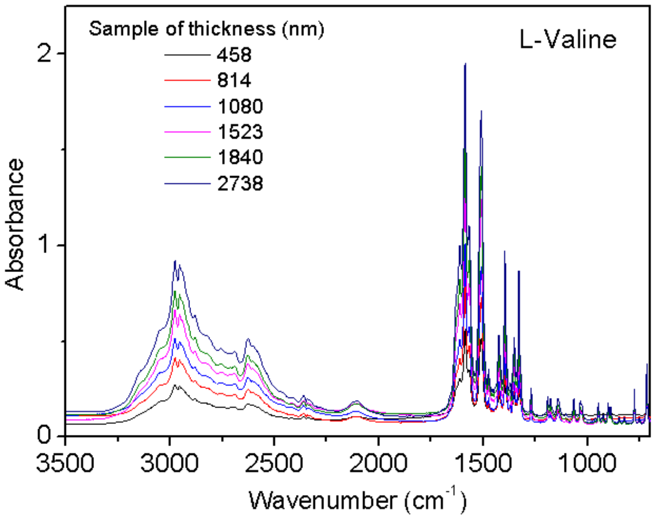

Figure 4.1: L-valine infrared spectra of six distinct samples; thicknesses measured by profilometry.

After IR characterization, samples were measured by profilometry (Bruker, Dektak XT), Figures 4.2 (a) – (c). The parameters used were: 2 mm as length of scan, 0.666 µm/pt resolution, 3000 points measured, 200 µm/s scan velocity, 10 s scan duration and 2 mg the applied tip force. Figure 4.2 (d) is a picture of a valine sample taken from the profilometer’s camera; the white region corresponds to the ZnSe substrate and the dark one, on the right, to a thick valine film.

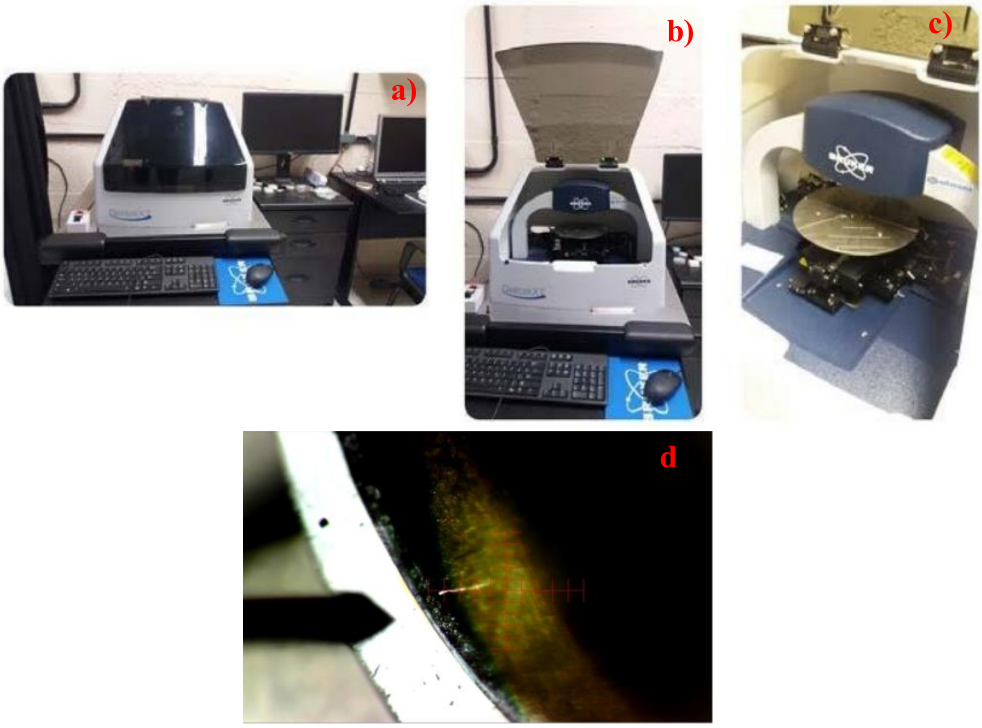

Figure 4.2: a) – c) DEKTAK 3 profilometer at the Van de Graaff Laboratory [55] d) Picture from profilometer’s camera; white region corresponds to the sample substrate, while the dark region to the deposited valine film.

The height profile of a multi-deposited sample is shown in Figure 4.3, with the level zero being at the substrate surface. The thicknesses (ℓ) are given by the average height of the plateau in the green region; in Fig. 4.3, ℓ ~ 2513 nm. It is worth noticing that there is more than one step, which means that, after each deposition, the position of the sample slightly changed and the sample holder masked the pellet in a different region. The most important region is at the center of the sample, where the IR beam crosses it – that is the reason why the average of heights is performed in the selected green region.

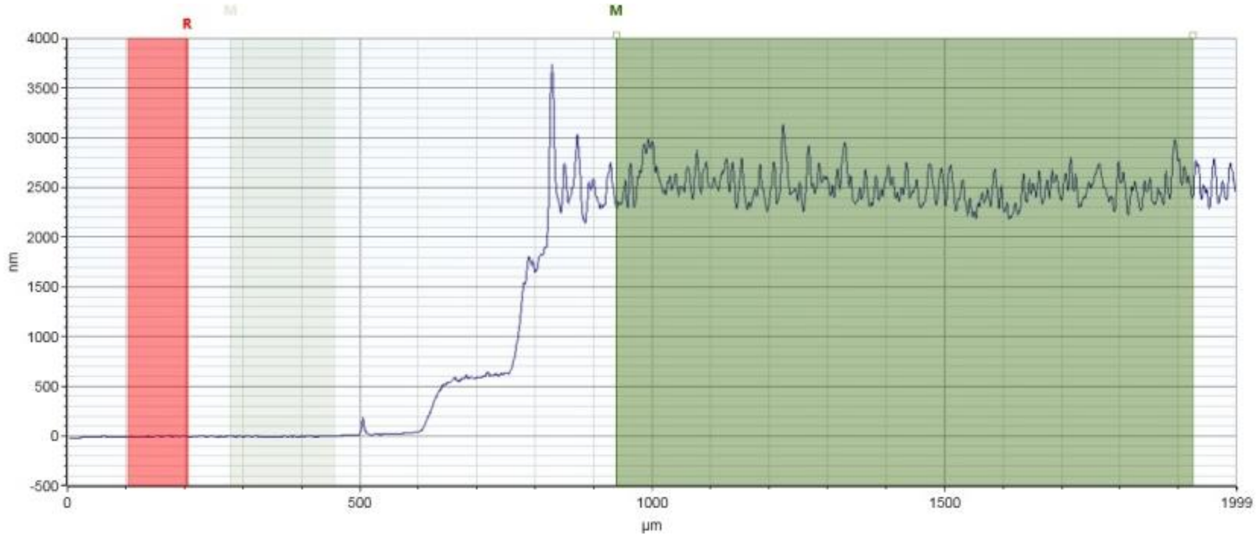

Figure 4.3: Example of valine height profile, calibration fixing the level zero at the substrate surface. Thickness is the average height of hills and valleys of the green region; in this case ~ 2513 nm.

Combining infrared absorbances with profilometry information, it is possible to determine the A-value of any desired wavelength region. A-values of selected valine bands were calculated and displayed in Table 4.1. By matching Beer-Lambert law, Eq. (4.1), with the relationship between the column density and sample thickness, Eq. (4.2), Eq. (4.3) enables the calculation of the A-values of each band,

$$\mathrm{N} = \ln(10)\frac{\mathrm{S}}{\mathrm{A}_\nu} \tag{4.1}$$

$$\mathrm{N} = \frac{\rho\, \mathrm{N_A}\, \ell}{\mathrm{M}} \tag{4.2}$$

$$\ell = \frac{\ln(10)\,\mathrm{M}}{\rho\ \mathrm{N_A}}\frac{\mathrm{S}}{\mathrm{A}_\nu} \tag{4.3}$$

where N is the column density, S the integrated infrared absorbance on the selected wavelength region, A_ν the A-value or band strength of the same selected region, ρ the material density, N_A the Avogadro's number, ℓ the sample thickness measured by profilometry and M the molecular weight.

Present experimental data provide the sample thickness dependence on its respective integrated absorbance. As an example, Figure 4.4 shows this correlation for the band 957-937 cm^{-1} (CN stretch [49]). As a check, it should be noticed that the origin (0,0) is located in the extrapolation of the fitted line with

Eq. (4.3), according to the Beer-Lambert law; the error bars have been considered in the fitting. Table 4.1 summarizes the A-values for the six bands of interest.

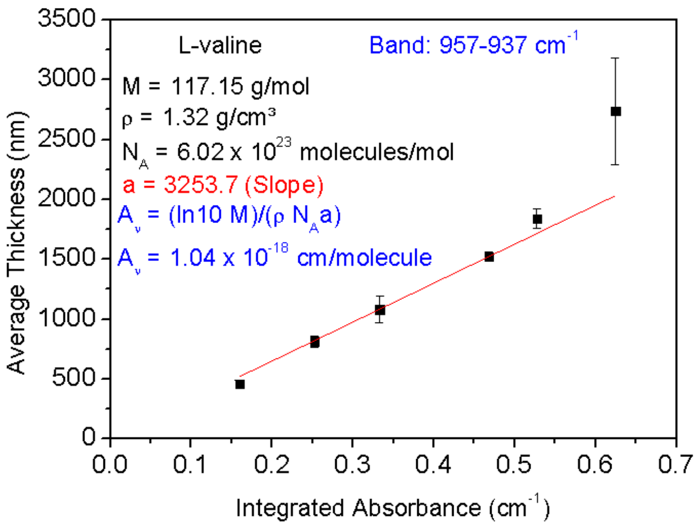

Figure 4.4: Valine sample average thickness as a function of its respective integrated infrared absorbance for band 957-937 cm^{-1}. A_v obtained by the fitted slope and the equation 4.3. Extrapolation of the fitting includes the origin (0,0).

Table 4.1: L-Val integrated infrared selected bands and their respective measured A_v in this work. Highlighted band 957-937 cm^{-1} is the one presented in Figure 4.4.

Integrated region (cm^{-1})	$\mathbf{A_v}$ (cm/molecule)
3190-2430	3.11 x 10^{-16}
1651-1470	1.55 x 10^{-16}
1650-1301	2.19 x 10^{-16}
1408-1380	1.10 x 10^{-17}
957-937	**1.04 x 10^{-18}**
726-705	3.37 x 10^{-18}

4.1.1.2
Phenylalanine

The same procedure outlined in the previous section was applied for phenylalanine (Phe) samples. Figure 4.5 shows the IR spectra of five Phe samples with distinct thicknesses.

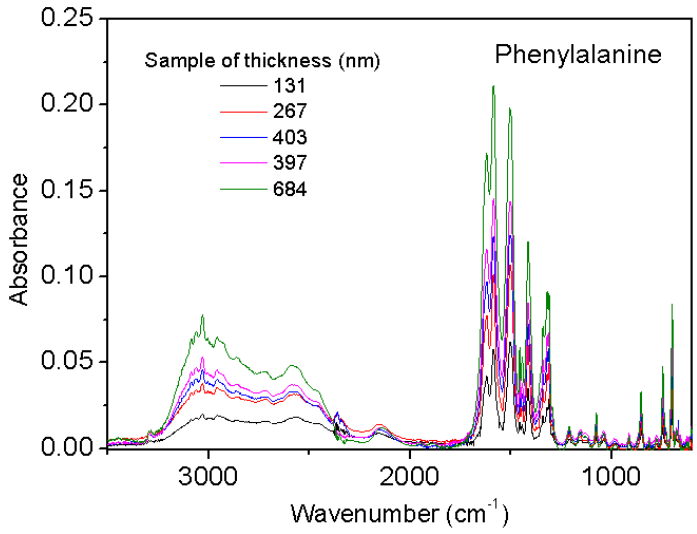

Figure 4.5: Phenylalanine infrared spectra of samples with five distinct thicknesses.

Figure 4.6 shows Phe thicknesses, measured by profilometry, as a function of IR integrated absorbances for the 879-834 cm^{-1} band (C C N sym str [51]) for five samples. The linear fitting with equation (4.3) allows the experimental determination of A_v. Again, error bars and the origin were considered on the fitting. Results for other bands are presented at Table 4.2. Supressing the middle point in the fitting, an offset of about 40 nm is obtained.

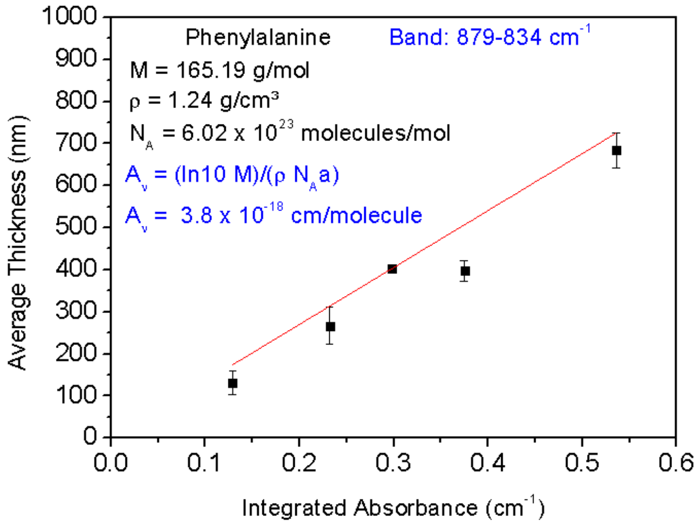

Figure 4.6: Phenylalanine sample average thickness as a function of the integrated infrared absorbance for the 879-834 cm^{-1} band. A_v is obtained by fitting data with Equation 4.3.

Table 4.2: Phe integrated infrared chosen regions and their calculated A_v. Highlighted 879-834 cm^{-1} band is the one presented in Figure 4.6.

Integrated region (cm^{-1})	**A_v** (cm/molecule)
2680-2400	2.00 x 10^{-17}
1650-1550	5.40 x 10^{-17}
1545-1465	4.45 x 10^{-17}
1430-1380*	11.7 x 10^{-18}
1360-1280	1.95 x 10^{-17}
879-834	**3.80 x 10^{-18}**

* Mejía et al. (2021) [51].

4.1.2

L-Valine sublimation rate

Three L-valine samples, prepared simultaneously by vacuum deposition, were heated at 90, 100, and 110 °C in a lab oven (Nova Ética 400 – 1ND). Figure 4.7 shows the obtained infrared spectra before the thermal processing, p = 1 atm.

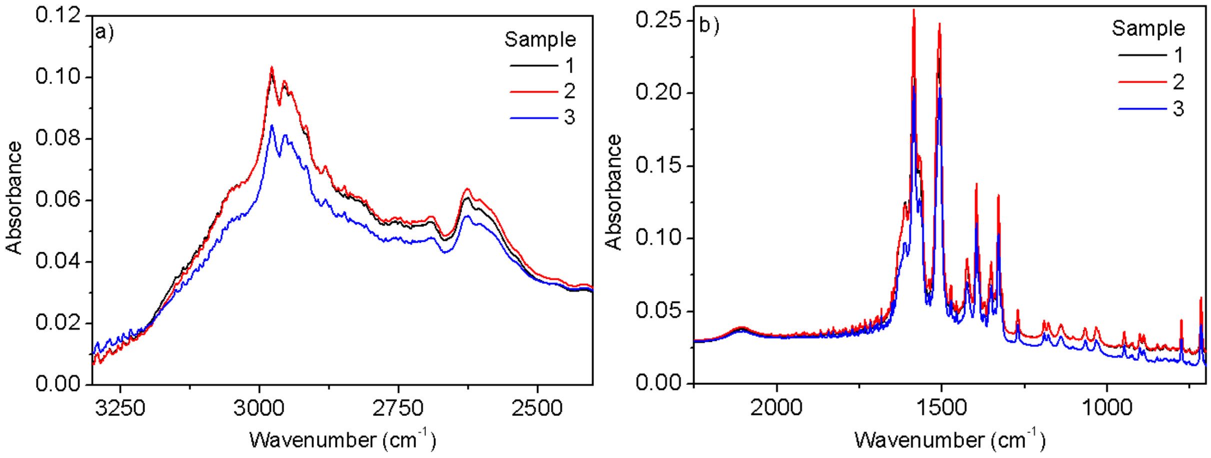

Figure 4.7: Infrared spectra of three non-processed valine samples.

Samples 1, 2 and 3 were 236, 243 and 186 nm thick before being thermally processed at 90, 100 and 110 °C, respectively. Thicknesses were calculated based on A_v of the 3190-2430 cm^{-1} band, as described in the previous section. Figures 4.8 a) – d) show a zoom of the 1651-1470 cm^{-1} spectral region of non-processed samples and their evolution in time when heated at 90, 100, and 110 °C, respectively. The experimental procedure consisted in leaving the samples a designated time in the oven and then measure their IR spectra, which means that spectra were always acquired at room temperature.

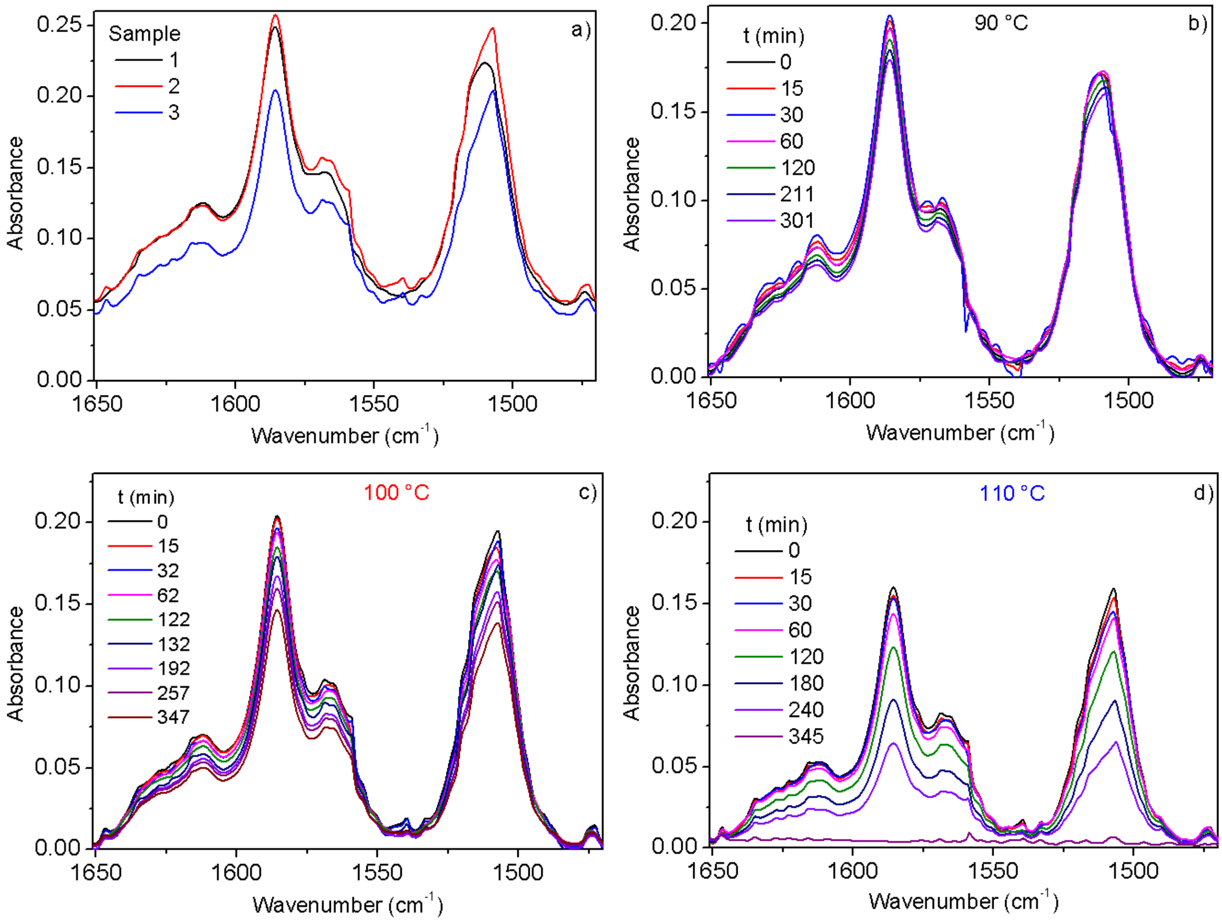

Figure 4.8: Zoom at 1651-1470 cm^{-1} spectral region of a) three non-processed L-valine samples, and their respective evolution in time when heated at b) 90 °C, c) 100 °C, and d) 110 °C.

The same procedure was followed for the region 3190-2430 cm^{-1}. Figures 4.9 a) – d) show the non-processed and the absorbance decreases for heating at 90, 100 and 110 °C, respectively.

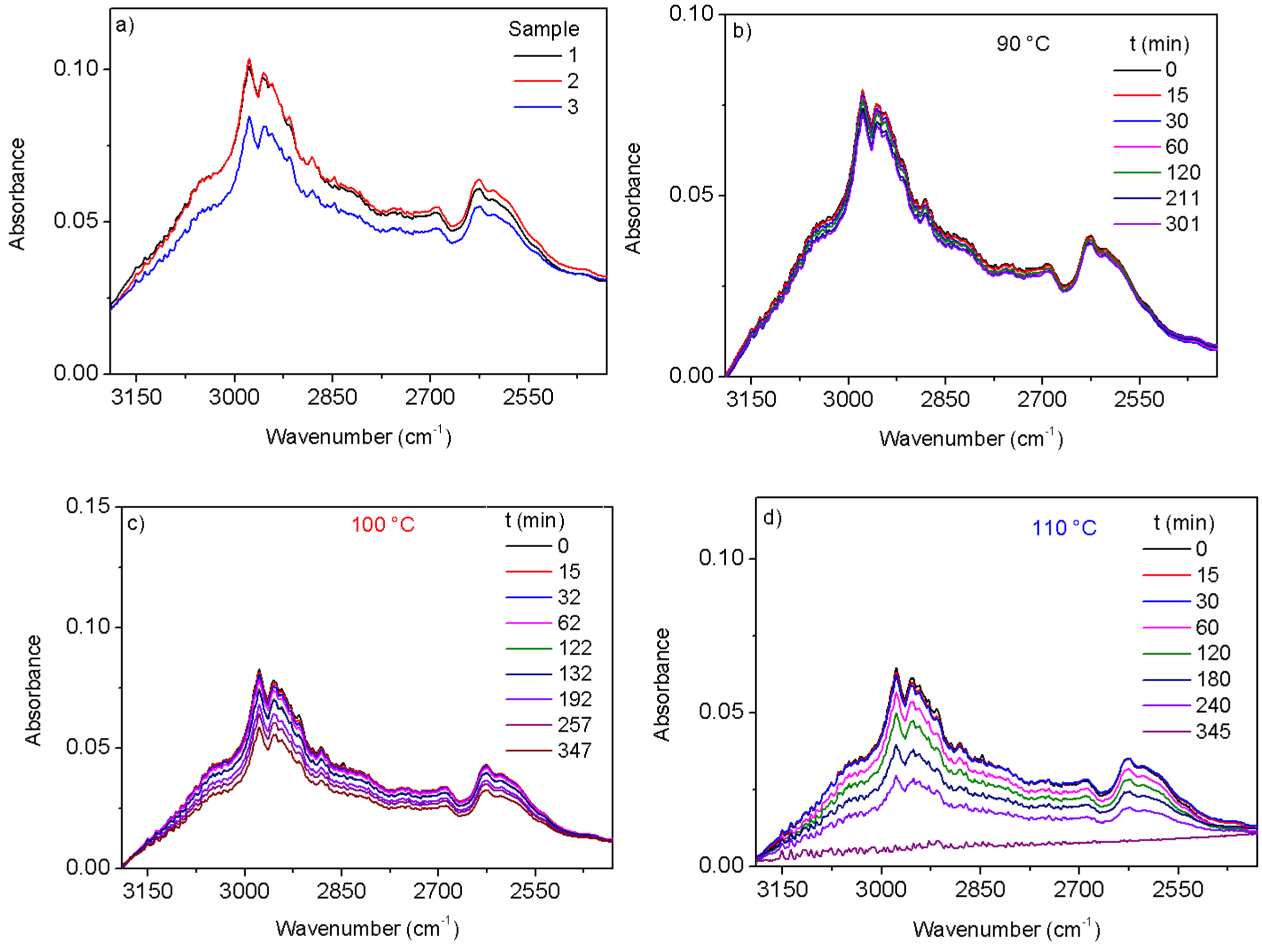

Figure 4.9: Zoom at 3190-2430 cm^{-1} region of a) three non-processed L-valine samples, and their evolutions in time when heated at b) 90 °C, c) 100 °C, and d) 110 °C.

Sample IR absorbances decrease faster as the oven temperature increases. The sample heated at 110 °C was the only one to completely vanish after the end of the measurements (~ 6 h). The decay of both bands (1651-1470 and 3190-2430 cm^{-1}), as seen in Figs 4.8 and 4.9, appear to be the same, i. e., the sublimation does not seem to be selective for branches of the molecule, otherwise decrease rates would be band dependent. A relevant conclusion is that heating does not dissociate the molecules, otherwise some non-volatile products like tholins [10] would stay in the sample and their IR bands would be seen; indeed, Figs. 4.8 and 4.9 d) show that no residual material remains after heating. Actually, tholins are a family of compounds; their characterization may include several bands.

4.1.3

Dependence on temperature of L-Valine IR spectra

An L-Valine sample, prepared by vacuum deposition, was placed in a sample holder connected to a cold head and inserted into a vacuum chamber, p ≈ 10^{-7} mbar (sections 3.2.1 and 3.4.1). Infrared spectra were acquired in function of sample temperature. Experimental data comprehend IR spectra of samples at 300, 250, 200, 150, 100, 80, 60 and 40 K (cooling down), and the same path backwards (heating up). The acquiring procedure was: i) after each run, a new temperature was set in the controller; ii) wait for the cryostat head to reach this temperature; iii) the new acquisition was initiated after 30 min, ensuring thermal equilibrium between the sample and the cold head. For the next step, the same sample was annealed in a lab oven (MARCONI, MA 033/3) at 120 °C for 12 hours and the same procedure was repeated (cooling down from 300 to 40 K, and then heating up from 40 to 300 K while following the IR changes).

Before and after thermally processing the sample, five IR absorbance regions were followed: 3200-2400, 1650-1300, 1280-1260, 1165-1120, and 960-930 cm^{-1}; from 300 – 100 K IR spectra were taken at steps of 50 K, and from 100 – 40 K measurements were done at intervals of 20 K, as shown in Figures 4.10 (a) – (e). Notice that, when the temperature decreases: i) peaks become more resolved, ii) the positions of some bands blueshift (towards higher wavenumbers) slightly as the temperature decreases, and iii) at the end of the excursion (when the sample is at room temperature again) the spectrum is identical to the initial one. Furthermore, spectra at the same temperature have the same features, no matter if the sample is being cooled or heated (within the upper limit of 300 K). Changes in band positions are also restored when sample goes back to 300 K, which indicates that no phase transition occurred in these annealing procedures.

a) 3200-2400 cm^{-1}

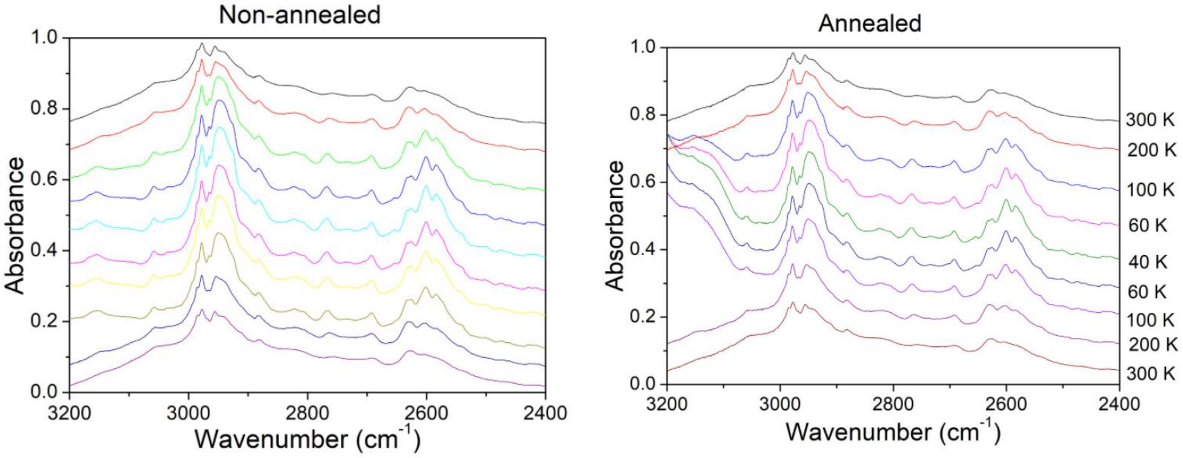

b) 1650-1300 cm^{-1}

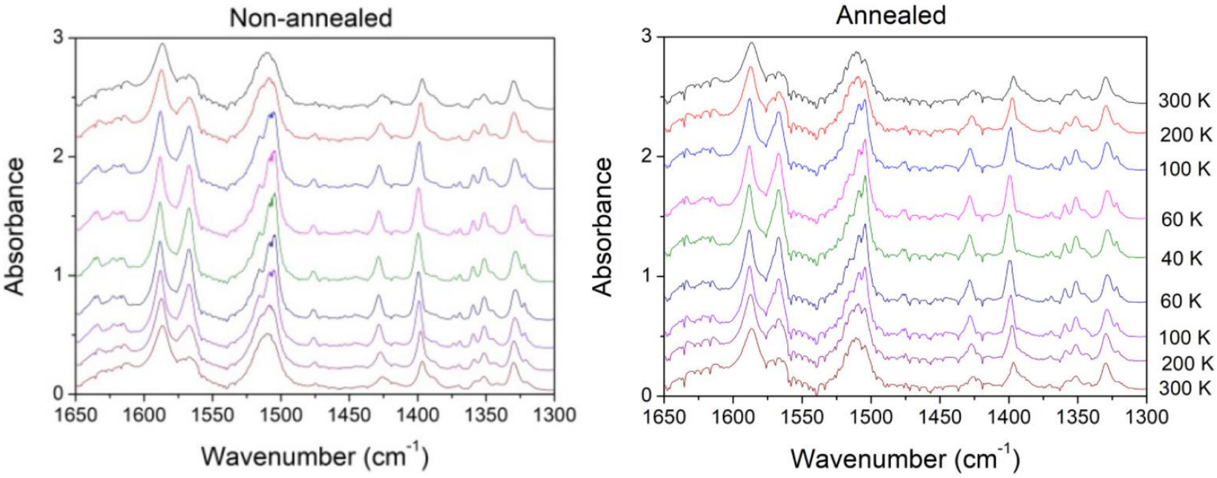

c) 1280-1260 cm^{-1}

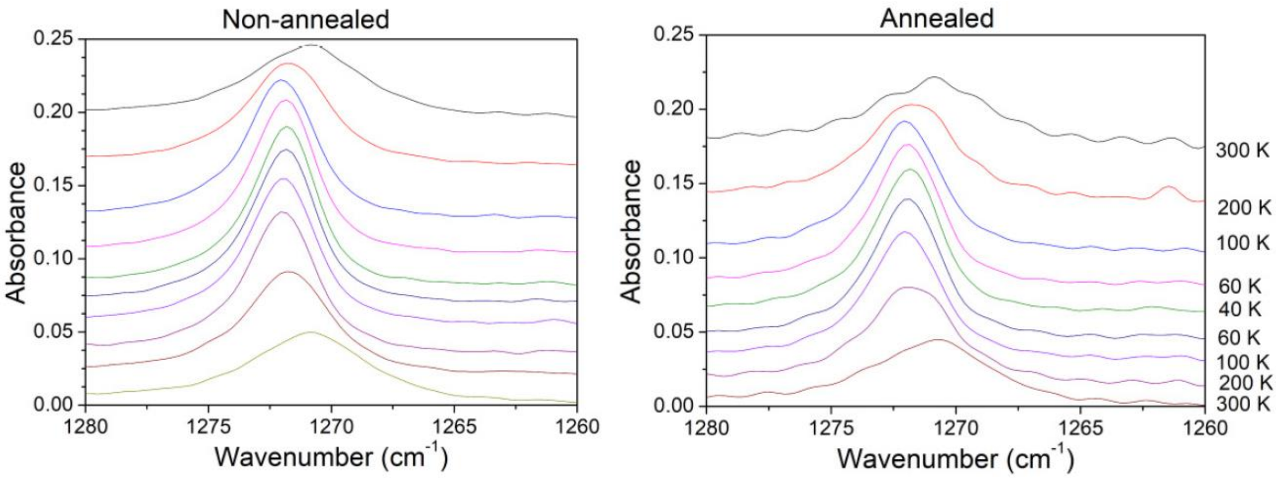

d) 1165-1120 cm^{-1}

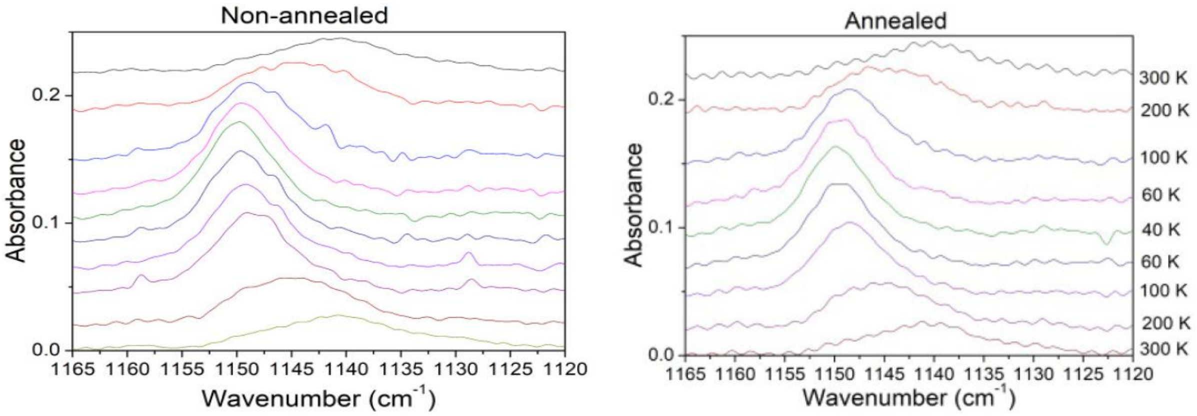

e) 960-930 cm^{-1}

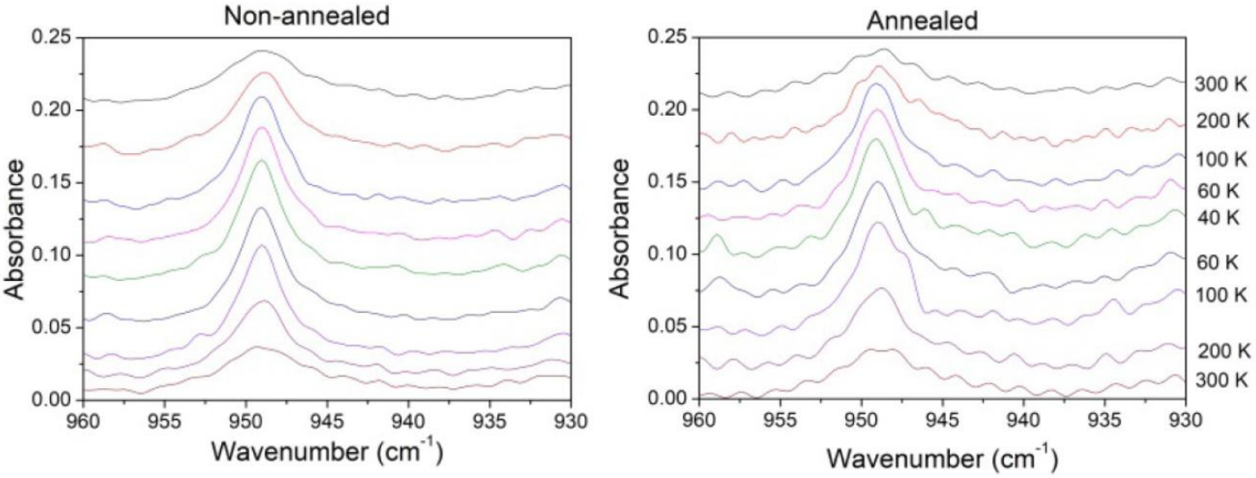

Figure 4.10: Non- and annealed valine sample IR regions a) 3200-2400, b) 1650-1300, c) 1280-1260, d) 1165-1120, and e) 960-930 cm^{-1}. Absorbance in arbitrary units. Adapted from da Costa & da Silveira (2019) [56].

4.2

Degradation of amino acids by ion beams

The next three subsections describe how glycine, valine and phenylalanine, in an increasing molecular complexity order, were processed by different ion beams, and under specific experimental conditions (sample preparation and laboratory where measurements took place, in particular).

4.2.1

Glycine

Three glycine samples, ~200 nm thick, prepared by vacuum deposition onto KBr substrates as described in section 3.2.1, were irradiated by 1.8 MeV H^+

and 1.5 MeV He^+ and N^+ ions produced by the Van de Graaff accelerator, see Section 3.4. Samples were placed in a vacuum chamber, residual gas pressure ~ $5x10^{-7}$ mbar, and bombarded with the aforementioned ions at room temperature. The evolutions of the 2663-2392 (peaks 2610 and 2527), 2179-2095 (2137), 1350-1315 (1332), 1158-1092 (1125), and 1047-1016 (1031) cm^{-1} bands with fluence, F, were followed by infrared spectroscopy. Figure 4.11 (a) shows the spectrum of a virgin (non-processed) glycine sample, while Figures 4.11 (b) and (c) display the absorbance decrease of the bands as the 1.5 MeV N^+ beam fluence increases. Spectra of glycine samples irradiated with other beams are quite similar, so only the N^+ data is displayed as an example.

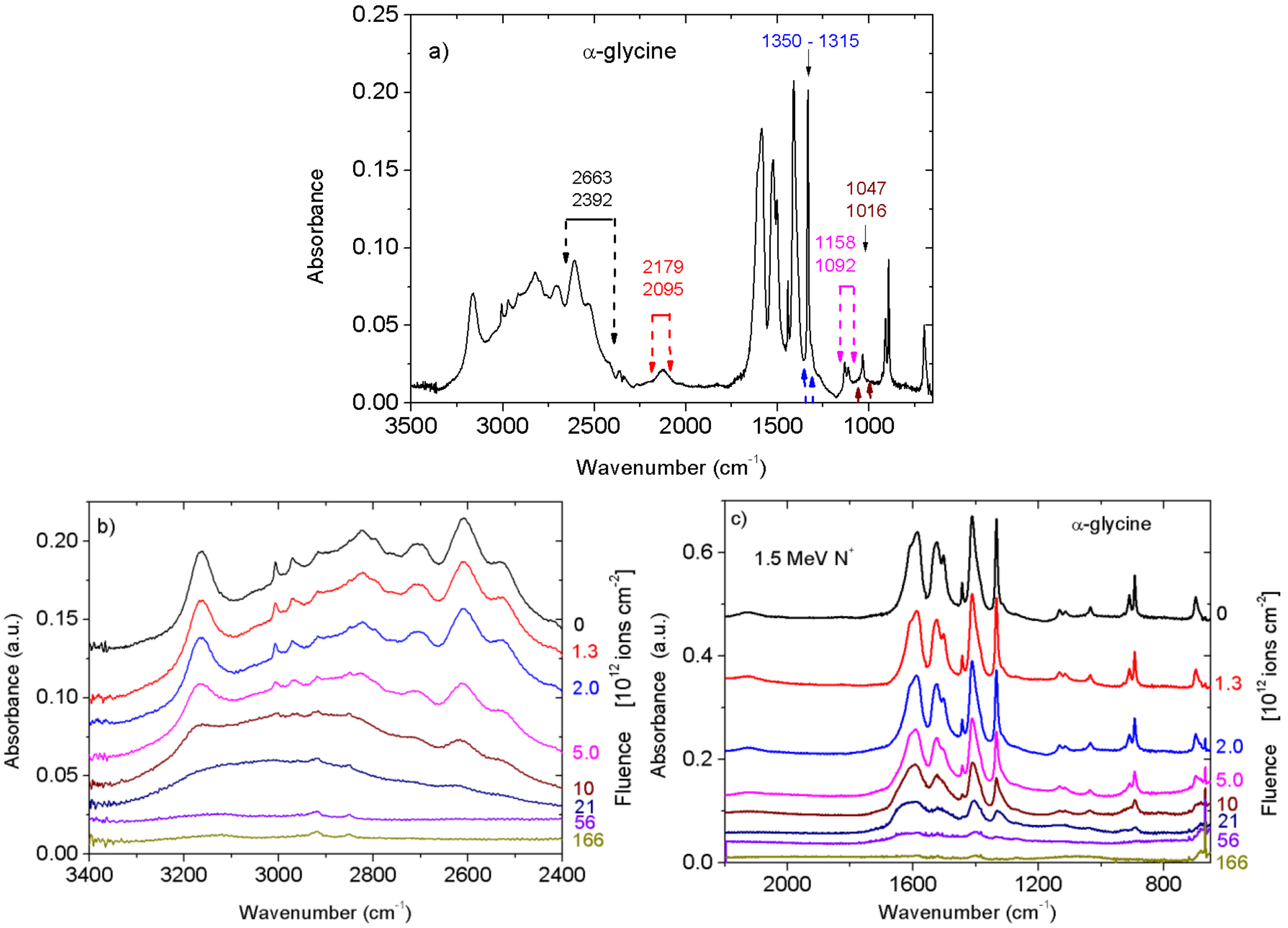

Figure 4.11: Glycine IR spectra of a) a non-processed sample, highlighted regions with dashed arrows indicate the bands followed in the analysis; IR regions b) 3400-2400 cm^{-1}; and c) 2200-700 cm^{-1} where, top to bottom, the 1.5 MeV N^+ beam fluence increases [54] .

The main phenomena occurring during the irradiation are radiolysis and sputtering. Either by molecular dissociation or ejection, the number of precursor molecules decreases as the beam fluence increases, which means that there are less molecules vibrating and, therefore, IR bands have lower signals (Beer-

Lambert law). Figures 4.12 (a) and (b) present the integrated absorbance evolution for the five selected regions, in function of N and He beams fluence, respectively; both beams had the same kinetic energy, 1.5 MeV. It is possible to note that, except for the end of band 2137 (red dots), the general decay behavior of the bands is the same for both beams. As highlighted in Figure 4.12 (b), some bands level off at non-zero absorbance values for distinct reasons such as the formation of products (pdt), which are daughter species, contamination with rotational water outside the chamber (H_2O), and background (bkg) problems when the peak areas become too small; the latter requires special attention since measurement errors are bigger at the end of experiments (higher fluences) because of low band signals. Solid lines on the figures are fittings with the expression $S(F) = S_0 \exp(-\sigma F) + S_\infty$, and the obtained destruction cross sections will be discussed in Chapter 6.

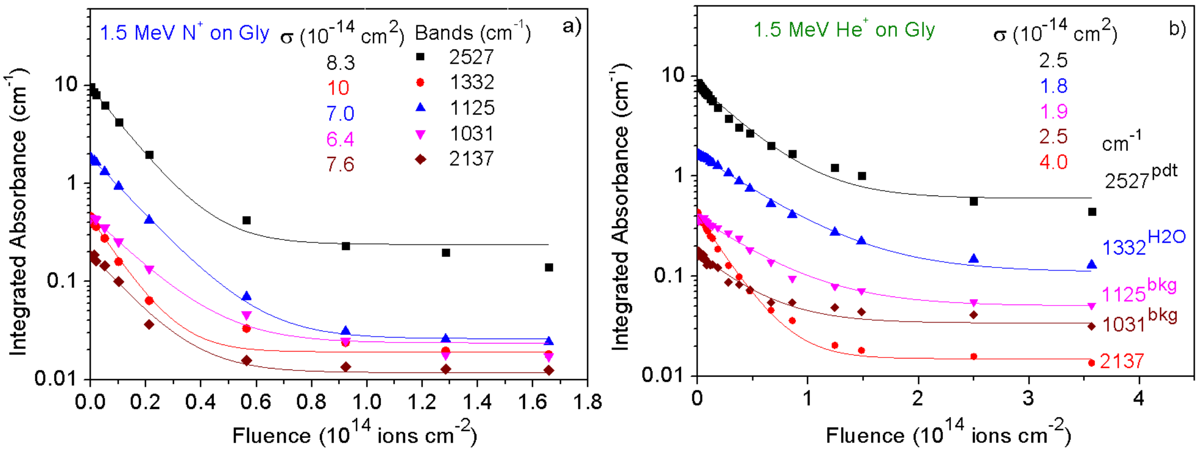

Figure 4.12: Integrated absorbance evolutions of five selected glycine bands in function of 1.5 MeV a) N^+ and b) He^+ beam fluences. Lines are fittings with equation $S = S_0 \exp(-\sigma F) + S_\infty$. Errors are ~ 5 % for low fluence measurements and > 50% for high ones.

Figure 4.13 presents the results of proton data analysis. Again, the general behavior of the bands is similar to the one seen for the other beams, although these results do not show the band levelling off as the previous ones. This is explained by the fact that this sample was not completely destroyed by irradiation, though this was the longest experiment (~26 hours). Nevertheless, the exhibited data are enough to extract important information such as the destruction cross section. Table 4.3 summarizes the apparent destruction cross sections for the beams 1.5 MeV N^+, He^+ and H^+.

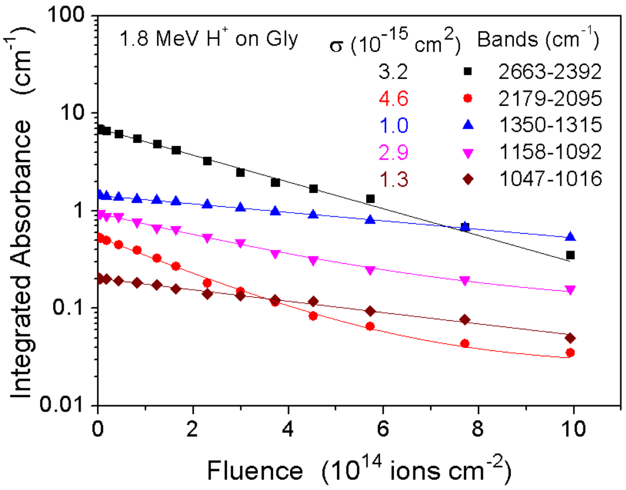

Figure 4.13: Integrated absorbance evolutions of five selected glycine bands in function of 1.5 MeV H^+ beam fluences.

Table 4.3: Apparent destruction cross sections for five glycine bands and their respective average for 1.5 MeV N^+, He^+ and H^+ ion beams.

Band	**σ_d^{ap} (10^{-16} cm^2)**		
(cm^{-1})	**1.5 MeV N^+**	**1.5 MeV He^+**	**1.5 MeV H^+**
2663-2392	830	250	32
2179-2095	1000	180	46
1350-1315	700	190	10
1158-1092	640	250	29
1047-1016	760	400	13
Average σ_d^{ap}	786 ± 214	254 ± 146	26 ± 20

4.2.2
Valine
4.2.2.1
Dependence on ion beam and its energy

D-valine samples, prepared by drop casting onto ZnSe substrates (see section 3.2.2), were bombarded at room temperature by 1.5 MeV H^+, He^+, and N^+ in the Van de Graaff laboratory at PUC-Rio, and by 230 MeV S^{15+} at GANIL facilities, Caen – France [57]. Using infrared spectroscopy, the evolutions with fluence of the 3300-2400, 1335-1304 (peak at 1329), 1279-1261 (1271), 957-937 (948), and 726-705 (716) cm^{-1} IR regions were followed. Figures 4.14 (a) and (b) display three and four spectra of valine, from top to bottom, corresponding to zero, intermediates and maximum fluences of the 1.5 MeV proton and of the 230 MeV sulfur beams, respectively.

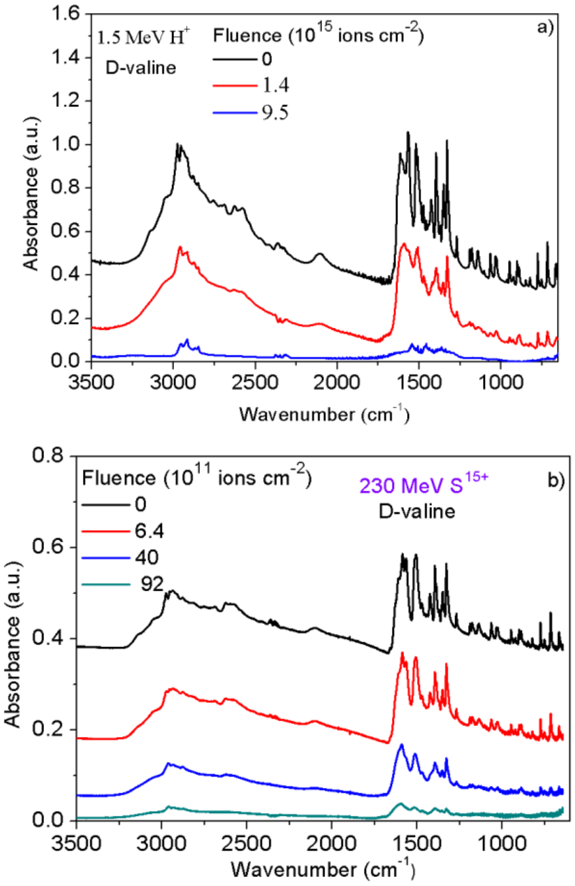

Figure 4.14: D-Valine IR spectra of samples bombarded with a) 1.5 MeV H^+ and b) 230 MeV S^{15+} ion beams.

In more detail, for the 1.5 MeV H^+ beam, Figures 4.15 (a) – (e) show particular characteristics of the analyzed bands, such as the appearance of daughter species and the broadening of some bands as the fluence increases.

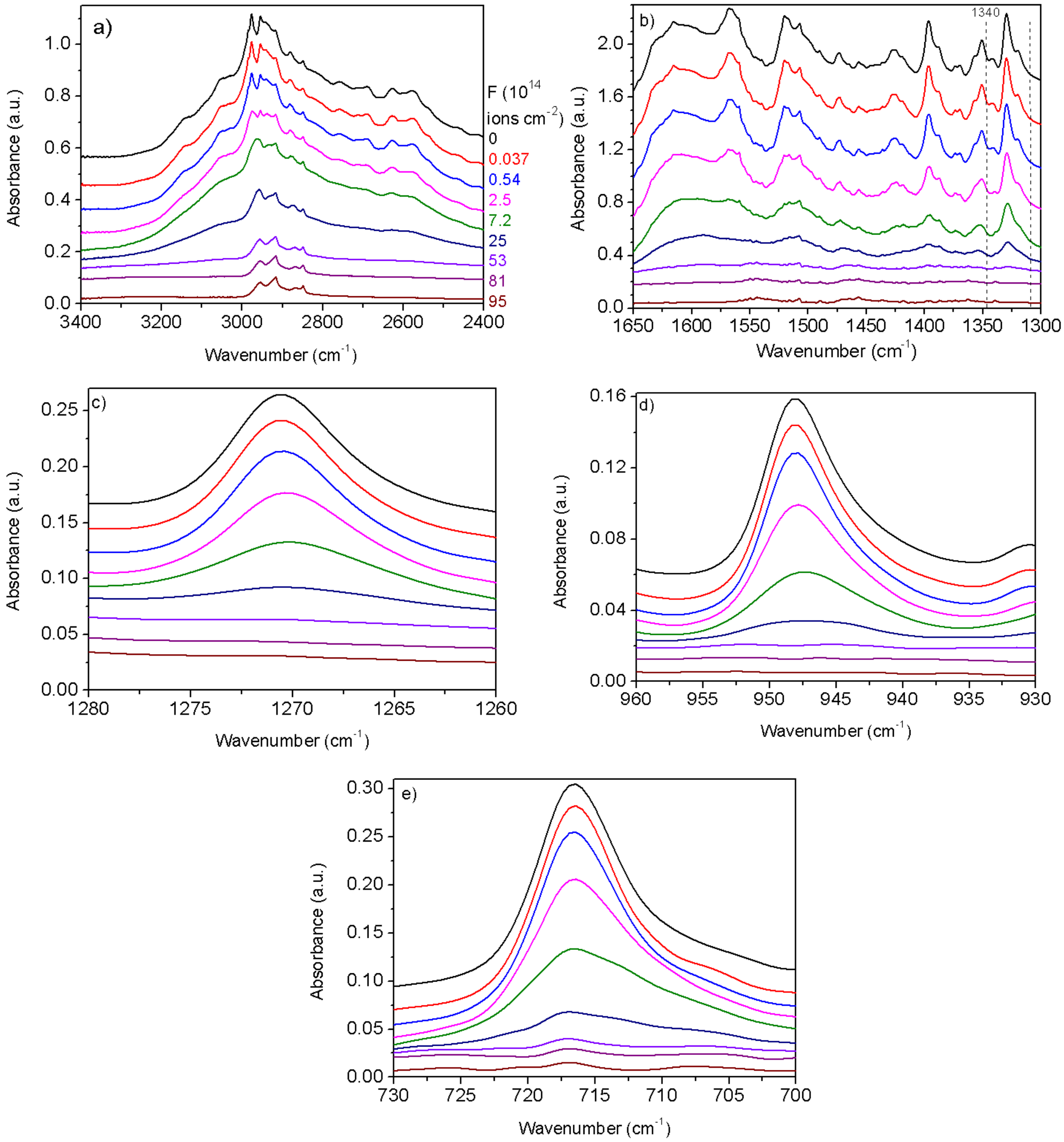

Figure 4.15: Valine absorbance evolutions with 1.5 MeV H^+ beam fluence for the bands a) 3400-2400, b) 1650-1300, c) 1280-1260, d) 960-930 and e) 730-700 cm^{-1}.

Figures 4.16 (a) – (d) represent the evolutions of the five selected bands in function of 1.5 MeV H^+, He^+, N^+, and 230 MeV S^{15+} beam fluences, respectively; Table 4.4 displays their apparent destruction cross sections.

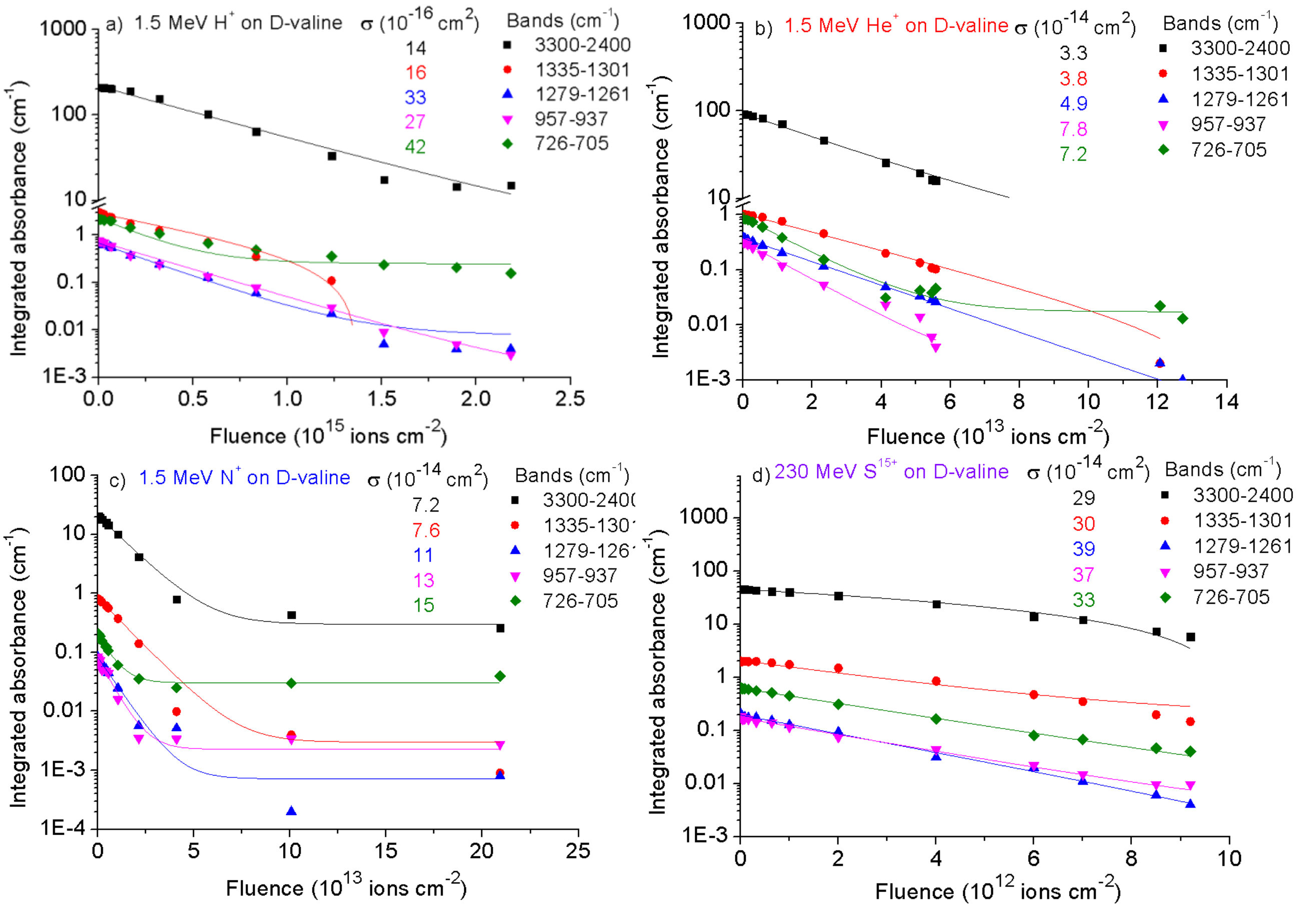

Figure 4.16: D-valine integrated absorbance of five selected bands in function of 1.5 MeV a) H^+, b) He^+, and c) N^+ and d) 230 MeV S^{15+} beam fluence.

Table 4.4: Apparent destruction cross sections for five valine bands and their respective average for four MeV ion beams.

Band (cm^{-1})	**σ_d^{ap} (10^{-16} cm^2)**			
	1.5 MeV H^+	**1.5 MeV He^+**	**1.5 MeV N^+**	**230 MeV S^{15+}**
3300-2400	14	330	720	2900
1335-1304	16	380	760	3000
1279-1261	33	490	1100	3900
957-937	27	780	1300	3700
726-705	42	720	1500	3300
Average σ_d^{ap}	26 ± 16	540 ± 210	1100 ± 400	3370 ± 400

4.2.2.2

Nitrogen beam data

This section presents various data from the irradiation of valine by nitrogen beams in distinct conditions, such as molecular beam (N_2^+), and beams with different charge states (N^{q+}, q = 1, 2 and 3) and energies (0.75, 1.5 and 6.0 MeV).

- Beam charge state (N^{q+})

Five L-valine samples, ~25 nm thick, prepared by vacuum deposition on ZnSe (see section 3.2.1), were bombarded by 1.5 MeV N^+, N^+, N^{2+}, N^{3+} and 6.0 MeV N^{2+} at 300 K and $p \approx 10^{-6}$ mbar. Different charge states were obtained by a selector magnet, as described in section 3.4. For each beam the evolutions of the IR bands 3190-2430, 1602-1579 (1507), and 1337-1320 (1330) cm^{-1} were followed and their respective normalized integrated absorbance is displayed on Figures 4.17 (a) – (c) and 4.18; lines are fittings and the obtained destruction cross sections are presented in the same color code.

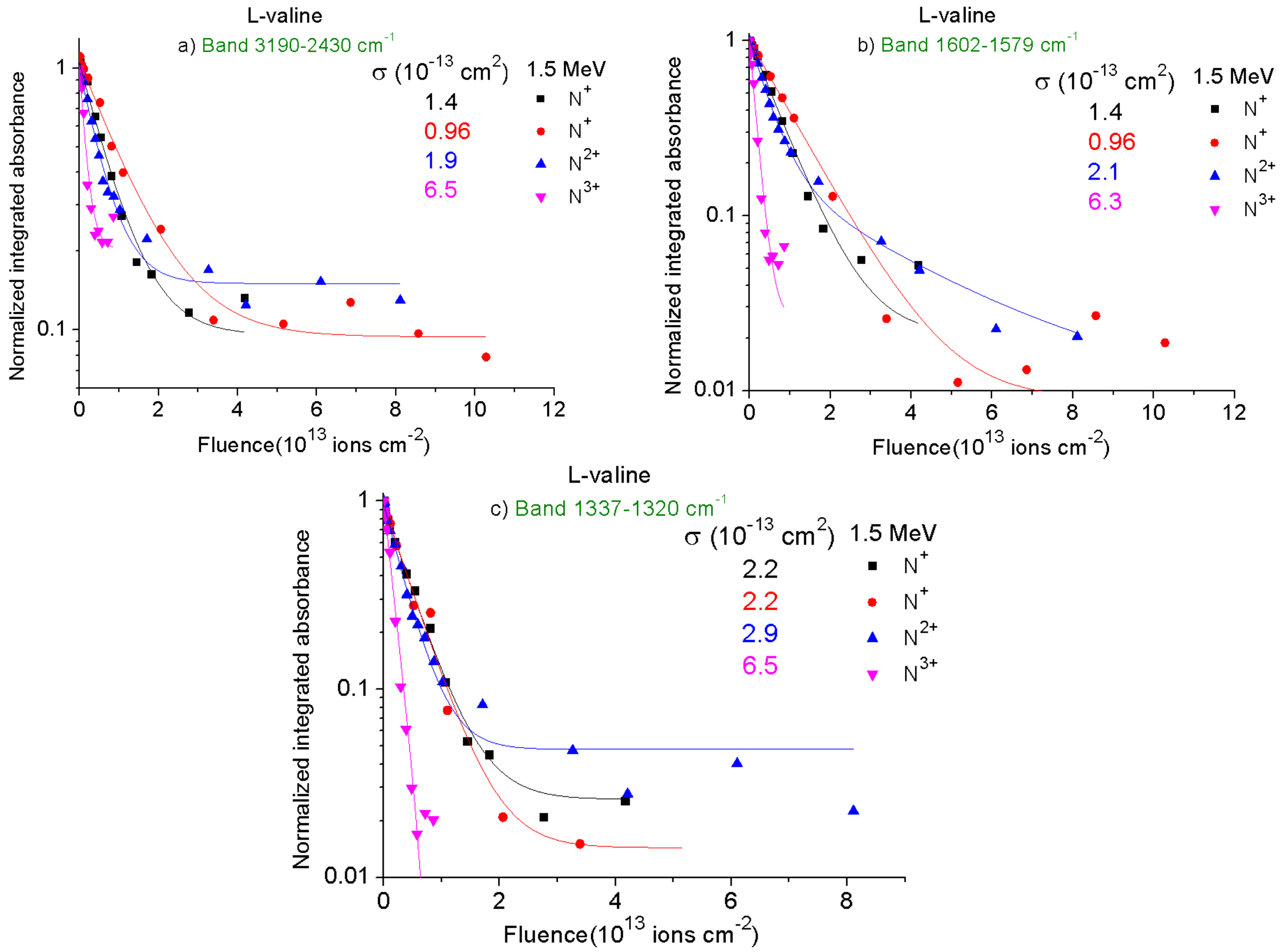

Figure 4.17: Evolution of the normalized integrated absorbances of valine with fluence of the beams 1.5 MeV N^+, N^+, N^{2+} and N^{3+} for the bands a) 3190-2430, b) 1602-1579, and c) 1337-1320 cm^{-1}.

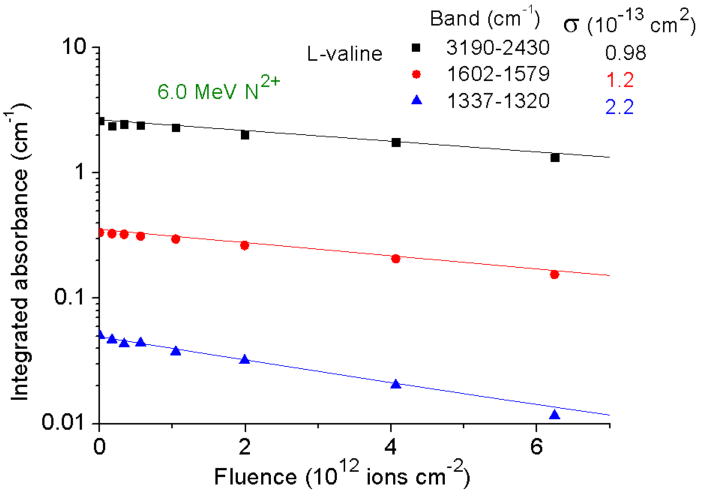

Figure 4.18: Evolution of the normalized integrated absorbances of valine with fluence of the beam 6.0 MeV N^{2+} for the bands 3190-2430, 1602-1579, and 1337-1320 cm^{-1}.

Next, four D-valine samples (~600 nm thick) prepared by vacuum deposition on KBr (see section 3.2.1), were respectively irradiated by 1.5 MeV N^+ and N^{2+}, and by 0.75 MeV N_2^+ at 300 K and $p \approx 10^{-6}$ mbar. Again, the evolutions of the same IR bands mentioned above were followed and they are presented on Figures 4.19 and 4.20. Tables 4.5 and 4.6 summarize the fitting parameters. The strong decrease of the integrated absorbance of the 1337-1320 band may be attributed to sputtering.

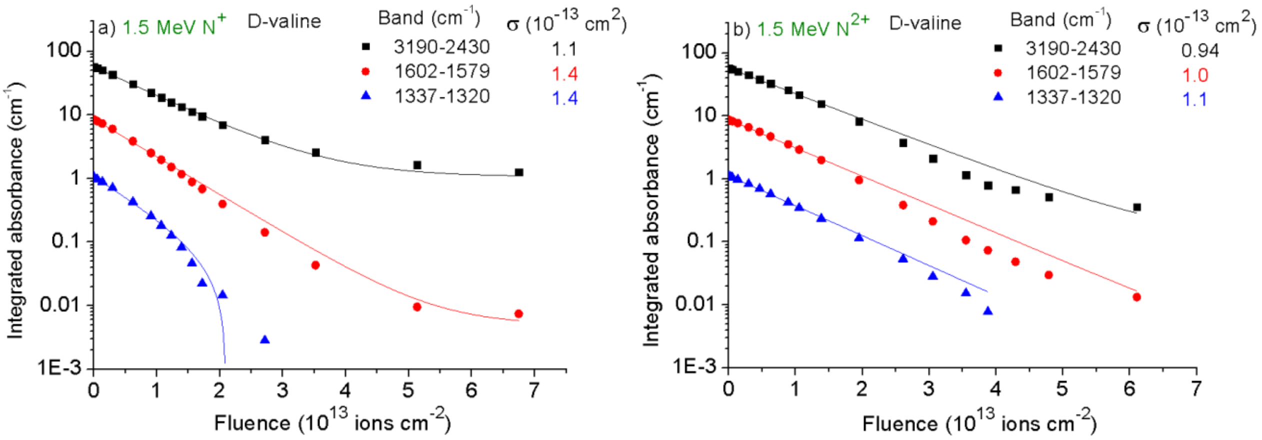

Figure 4.19: Evolution of the integrated absorbances of valine with fluence of the 1.5 MeV beams a) N^+ and b) N^{2+} for the bands 3190-2430, 1602-1579, and 1337-1320 cm^{-1}.

Table 4.5: Parameters obtained from the fitting of the integrated absorbances decay with the function $S(F) = S_0 \exp(-\sigma F) + S_\infty$. Data from valine irradiated by 1.5 and 6.0 MeV multi-charged nitrogen beams.

Sample	**Beam**	**Band (cm^{-1})**	**S_0 (cm^{-1})**	**σ (10^{-16} cm^2)**	**S_∞ (cm^{-1})**
L-Val	1.5 MeV N^+	3190-2430	0.95	1400	0.096
		1602-1579	0.99	1400	0.01
		1337-1320	0.91	2200	0.026
	1.5 MeV N^+	3190-2430	0.97	960	0.094
		1602-1579	0.99	960	0.01
		1337-1320	0.94	2200	0.014
	1.5 MeV N^{2+}	3190-2430	0.85	1900	0.15
		1602-1579	0.83	2100	0.17
		1337-1320	0.92	2900	0.048
	1.5 MeV N^{3+}	3190-2430	0.82	6500	0.20
		1602-1579	0.96	6300	0.03
		1337-1320	0.99	6500	-
	6.0 MeV N^{2+}	3190-2430	2.65	980	-
		1602-1579	0.35	1200	-
		1337-1320	0.048	2200	-
D-Val	1.5 MeV N^+	3190-2430	56.8	1100	1.07
		1602-1579	8.51	1400	0.005
		1337-1320	1.07	1400	-
	1.5 MeV N^{2+}	3190-2430	56.6	940	0.1
		1602-1579	8.66	1000	0.001
		1337-1320	1.11	1100	0

- Molecular beam

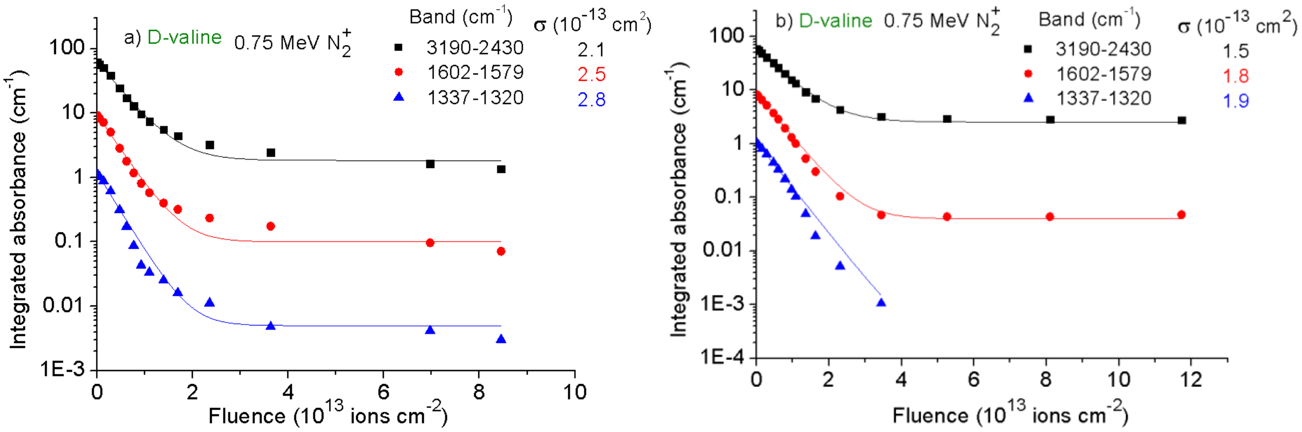

Figure 4.20: Evolution of the integrated absorbances of valine with fluence of the beam 0.75 MeV N_2^+ for the bands 3190-2430, 1602-1579, and 1337-1320 cm^{-1} for two distinct samples a) and b).

Table 4.6: Parameters obtained from the fitting of the integrated absorbances decay with the function $S(F) = S_0 \exp(-\sigma F) + S_\infty$. Data from valine with distinct thicknesses irradiated by 0.75 MeV N_2^+.

Band (cm^{-1})	**S_0 (cm^{-1})**	**σ (10^{-16} cm^2)**	**S_∞ (cm^{-1})**
3190-2430	61.3	2100	1.84
1602-1579	9.33	2500	0.1
1337-1320	1.17	2800	0.005
3190-2430	56.8	1500	2.53
1602-1579	8.40	1800	0.04
1337-1320	1.05	1900	0.0002

- Dependence on Sample thickness

Three L-valine samples, prepared by vacuum deposition on ZnSe (see section 3.2.1), with thicknesses 27.5, 44.2 and 64.9 nm were irradiated by 1.5 MeV N^+, at 300 K and $p \approx 10^{-6}$ mbar. In figures 4.21 (a) – (c), the evolutions of these three samples in function of beam fluence is presented for the 3190-2430, 1602-1579 and 1337-1320 cm^{-1} bands. Table 4.7 summarizes the fitting parameters.

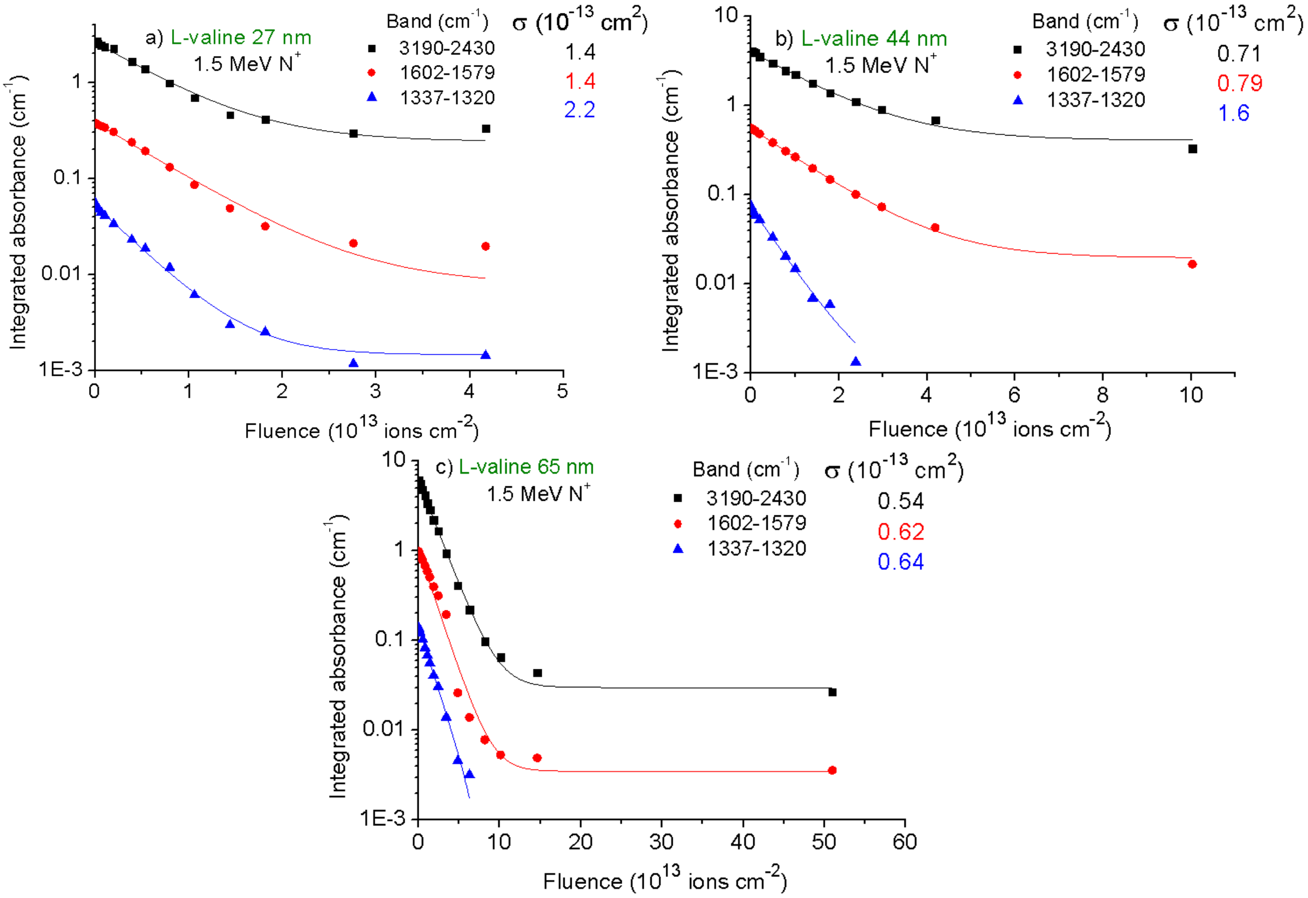

Figure 4.21: Evolution of valine integrated absorbances with fluence of the 1.5 MeV N$^+$ beam for the 3190-2430, 1602-1579, and 1337-1320 cm^{-1} bands. Sample thicknesses are: a) 27 nm, b) 44 nm and c) 65 nm.

Table 4.7: Parameters obtained from the fitting of the integrated absorbances decay with the function S(F) = $S_0 \exp(-\sigma F) + S_\infty$. Data from valine with distinct thicknesses irradiated by 1.5 MeV N$^+$.

Thickness (nm)	**Band (cm^{-1})**	**S_0 (cm^{-1})**	**σ (10^{-16} cm^2)**	**S_∞ (cm^{-1})**
27	3190-2430	2.40	1400	0.24
	1602-1579	0.37	1400	0.008
	1337-1320	0.051	2200	0.0014
44	3190-2430	3.66	710	0.41
	1602-1579	0.54	790	0.020
	1337-1320	0.071	1600	0.001
65	3190-2430	6.07	540	0.03
	1602-1579	1.02	620	0.0035
	1337-1320	0.14	640	-

4.2.3

Phenylalanine

DL-Phenylalanine samples, prepared by vacuum deposition over ZnSe substrates (see section 3.2.1), were irradiated by 0.5 and 2.0 MeV H^+, 2.0 MeV He^+, and 0.5 and 2.0 MeV N^+ beams. The radiolysis was followed by infrared spectroscopy via the analysis of the 2680-2400, 1650-1550, 1545-1465 (1500), 1430-1380 (1415), and 1360-1280 cm^{-1} bands. As an example, Figure 4.22 shows the Phe IR absorbance evolution as a function of the 2 MeV N^+ beam dose.

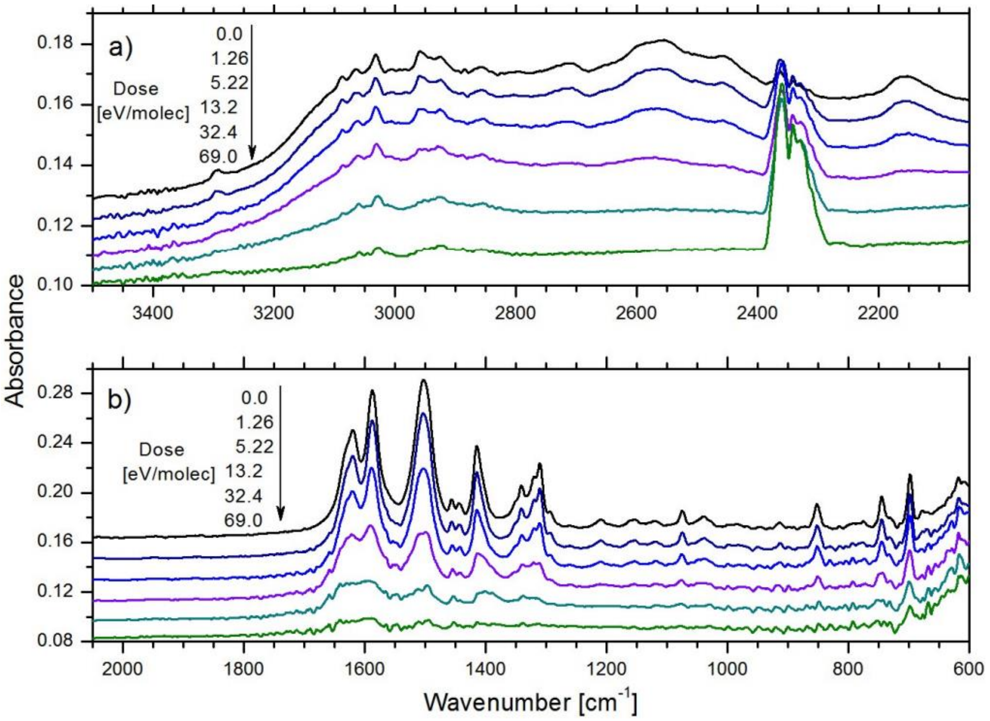

Figure 4.22: Phenylalanine spectra evolution of (a) 3500-2050 and (b) 2050-600 cm^{-1} IR regions, for increasing 2 MeV N^+ beam doses [51].

Figures 4.23 (a) – (f) present the normalized integrated absorbance evolutions of the 2680-2400 (peak 2500), 1650-1550 (1575), 1545-1465 (1500), 1430-1380 (1415), and 1360-1280 (1320) cm^{-1} bands for 2 MeV N^+, 0.5 MeV N^+, 2 MeV He^+, 0.5 MeV H^+, 2 MeV H^+, and 2 MeV H^+ beams, respectively. Blue solid lines are fittings, and data are presented in log-log scale to emphasize that band dispersions are small.

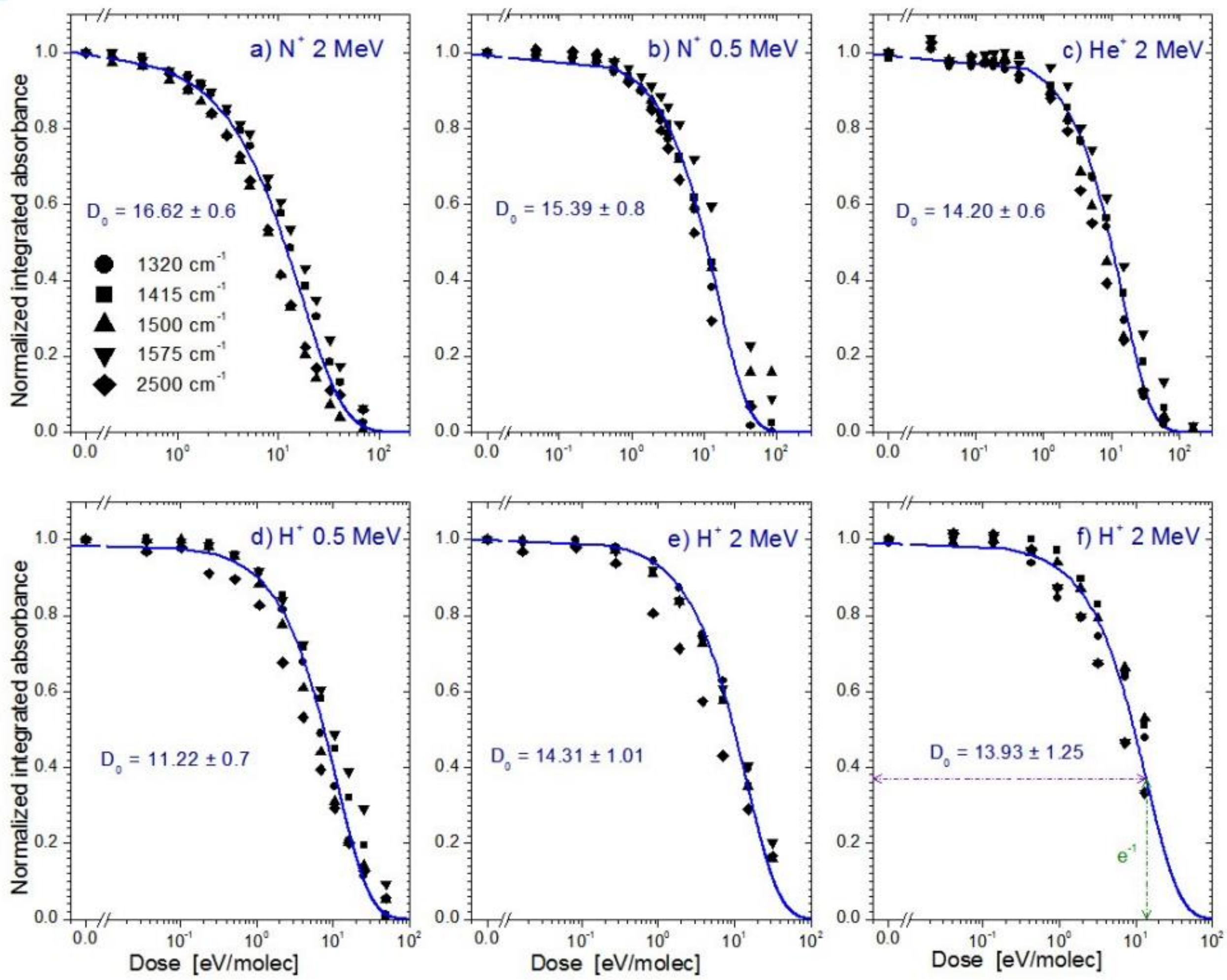

Figure 4.23: Normalized integrated absorbance for several Phe bands as a function of the dose of a) 2 MeV N^+, b) 0.5 MeV N^+, c) 2 MeV He^+, d) 0.5 MeV H^+, and e) and f) 2 MeV H^+ ion beams [51].

4.3
Electron beams

For this part, changing the ionizing source from MeV ions to keV electrons, amino acid L-valine data are presented in function of the beam current and energy, as well as of the sample thickness, temperature and crystallographic state. For the amino acid α-glycine, results of 1.0 keV electrons irradiation are also exhibited.

4.3.1
Beam current

Two L-valine samples, ~50 nm thick, prepared by vacuum deposition on ZnSe (see section 3.2.1), were bombarded by 1.0 keV electrons with 1.5 µA and 30.2 nA beam currents, at 300 K and $p \approx 10^{-6}$ mbar, in order to verify the existence of thermal effects during measurements (high current beams warm the sample and induce sublimation). Infrared absorbance regions 3190-2430 and 1650-1301 cm^{-1} were followed as the beam fluence increased; Figure 4.24 presents both data and the respective fittings.

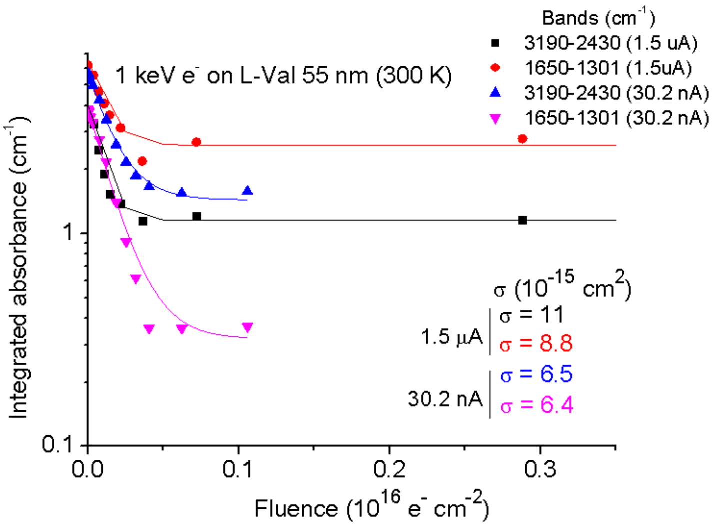

Figure 4.24: L-valine IR integrated absorbance evolutions with fluence of 1.0 keV electrons with 1.5 μA and 30.2 nA for the 3190-2430 and 1650-1301 cm^{-1} bands.

4.3.2

Sample thickness

L-valine samples, prepared by vacuum deposition, were irradiated by 100 and 1000 eV electrons. Four samples with distinct thicknesses for the former case, and seven samples for the latter were bombarded at room temperature and residual gas pressure ~10^{-7} mbar. Figures 4.25 (a) and (b) show the IR spectra of non-processed samples for both cases, respectively.

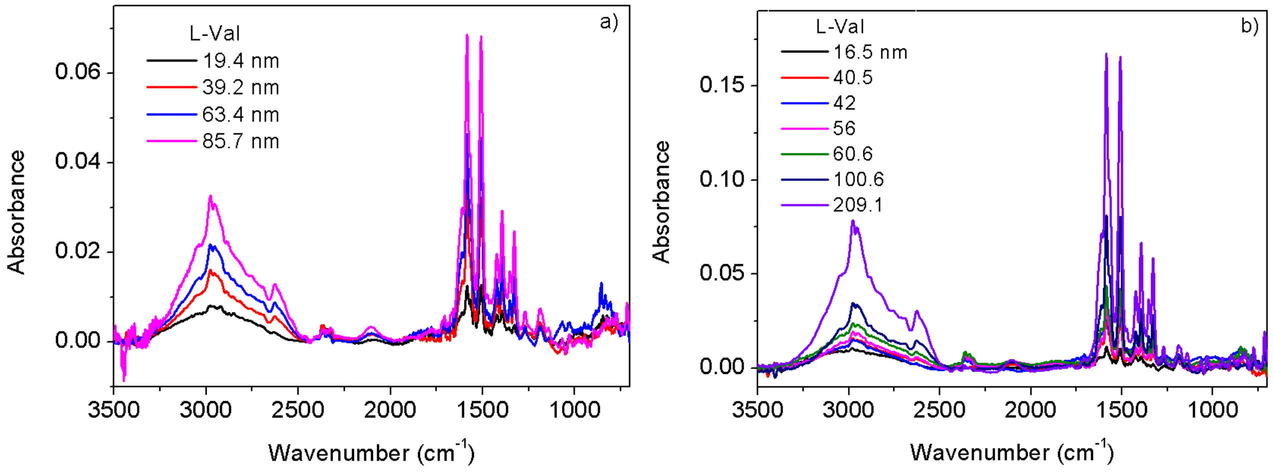

Figure 4.25: Infrared spectra of L-valine samples with (a) three and (b) seven distinct thicknesses to be bombarded with 100 and 1000 eV, respectively.

The 3190-2430 and 1602-1579 cm^{-1} bands were analyzed as a function of fluence. For the 1602-1579 cm^{-1} band, Figures 4.26 (a) – (d) show the evolution for thick and thin samples bombarded with 100 and 1000 eV.

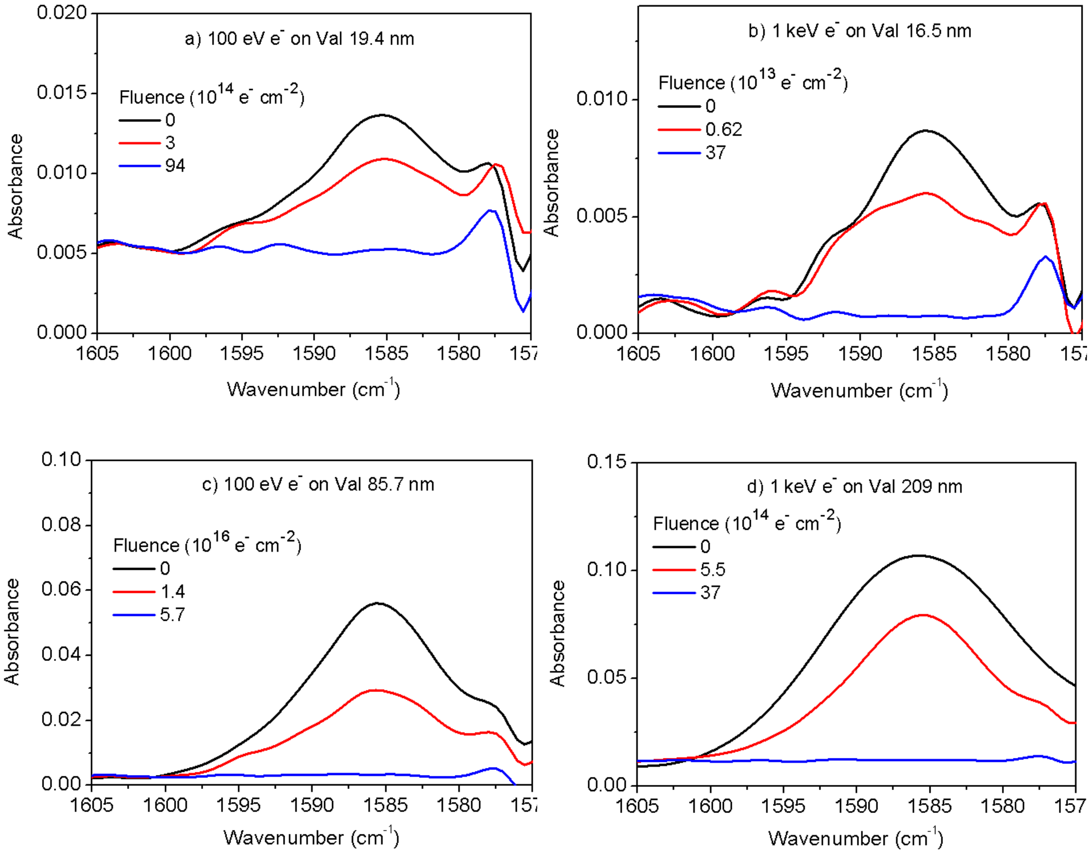

Figure 4.26: Thin (a)-(b) and thick (c)-(d) L-valine IR absorbance evolutions were both analyzed with fluence of 100 and 1000 eV e$^-$, respectively. Feature growing at ~1577 cm^{-1} is due to contaminant water.

For the analyzed 3190-2430 and 1602-1579 cm^{-1} bands, Figures 4.27 (a)-(b) and (c)-(d) present respectively the integrated absorbance evolutions for the various film thicknesses in function of 100 and 1000 eV electron beam fluences. Table 4.8 summarizes the fitting parameters.

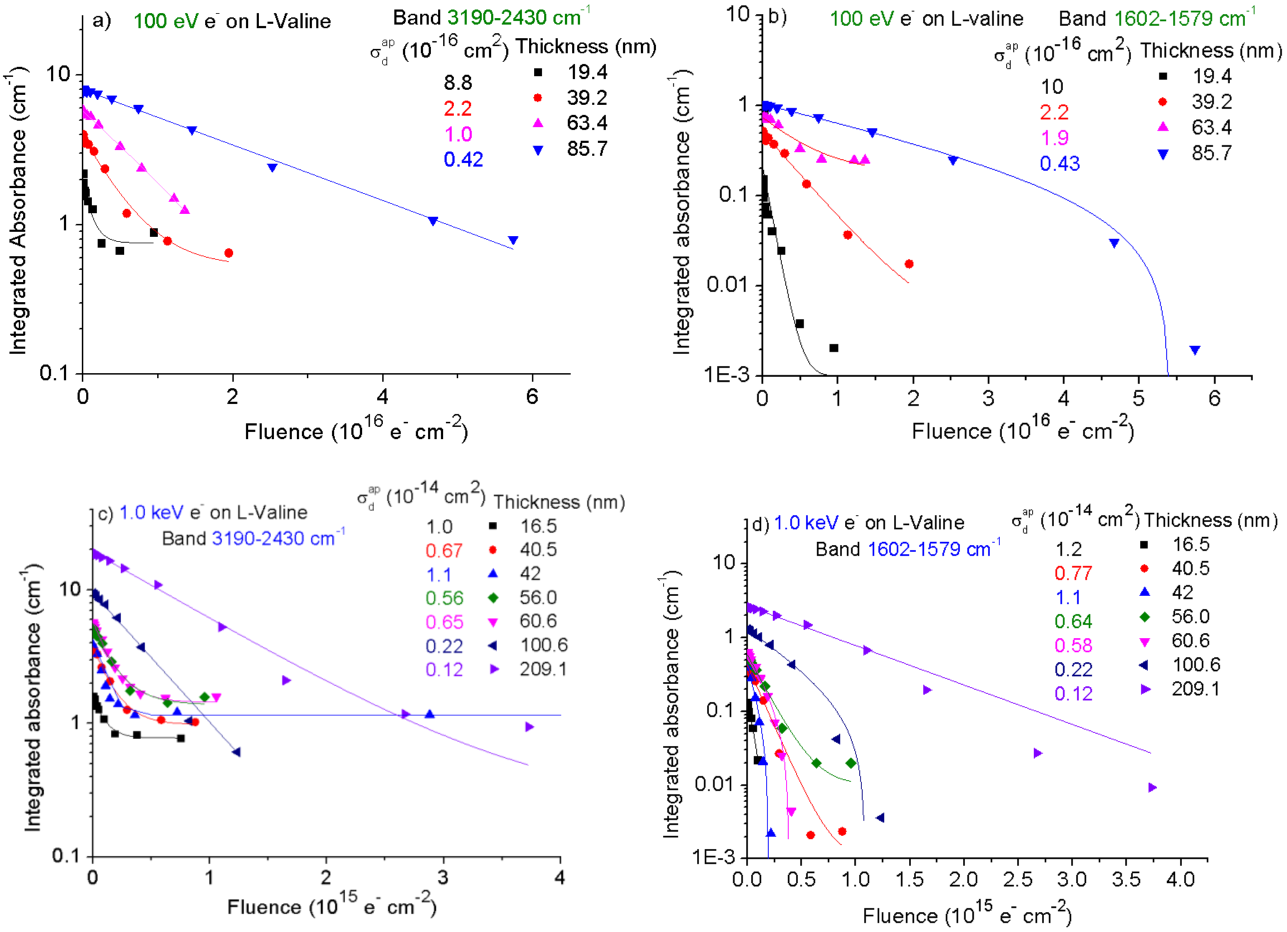

Figure 4.27: 3190-2430 and 1602-1579 cm^{-1} L-valine integrated absorbance evolutions in function of fluence of a) and b) 100, and c) and d) 1000 eV electron beams for samples with increasing thicknesses.

Table 4.8: Parameters obtained from the fitting of the integrated absorbances decay with the function $S(F) = S_0 \exp(-\sigma F) + S_\infty$. Data from valine at various thicknesses irradiated by electrons at two different energies.

Energy (eV)	**Thickness (nm)**	**Band (cm^{-1})**	**S_0 (cm^{-1})**	**σ (10^{-16} cm^2)**	**S_∞ (cm^{-1})**
100	19.4	3190-2430	1.78	8.8	0.75
		1602-1579	0.15	10	0. 001
	39.2	3190-2430	3.6	2.2	0.52
		1602-1579	0.52	2.2	0.003
	63.4	3190-2430	5.82	1.0	-
		1602-1579	0.71	1.9	0.18
	85.7	3190-2430	7.86	0.42	-
		1602-1579	1.03	0.43	-
1000	16.5	3190-2430	1.51	100	0.77
		1602-1579	0.13	120	-
	40.5	3190-2430	3.72	67	0.99
		1602-1579	0.42	77	0.001
	42	3190-2430	3.82	110	1.16
		1602-1579	0.40	110	-
	56	3190-2430	5.14	56	1.4
		1602-1579	0.58	64	0.01
	60.6	3190-2430	5.56	65	1.4
		1602-1579	0.64	58	-
	100.6	3190-2430	9.23	22	0
		1602-1579	1.3	22	-
	209.1	3190-2430	19.2	12	0.24
		1602-1579	2.7	12	0

4.3.3

Dependence on beam energy

Two data sets were acquired: i) five L-valine samples, ~55 nm, irradiated with 1000, 1000, 750, 500 and 100 eV electron beams, and ii) four thinner samples, ~18 nm, bombarded with 1000, 100, 60 and 60 eV e$^-$. Since: i) sample thickness plays an important role on the cross section determination (as seen in Section 4.3.2), and ii) low energy electrons have a shorter penetration depth in materials, thinner samples are required for a better understanding of the processing phenomenon, in the sense that analysis of the interactions is restricted to the collisions in the first monolayers. There is no clear feature on the spectra to reveal whether the sample was bombarded with 1 keV or 60 eV electrons, so there is no reason to repeat spectral evolution with fluence of some chosen beams; as an example, see figures 4.26 (a)-(d).

Evolutions of 3190-2430 and 1650-1301 cm^{-1} bands in function of the respective electron beam fluence were analyzed. Results are presented in Figure 4.28 for the thick sample and in Figure 4.29 for the thin one. Table 4.9 summarizes the fitting parameters.

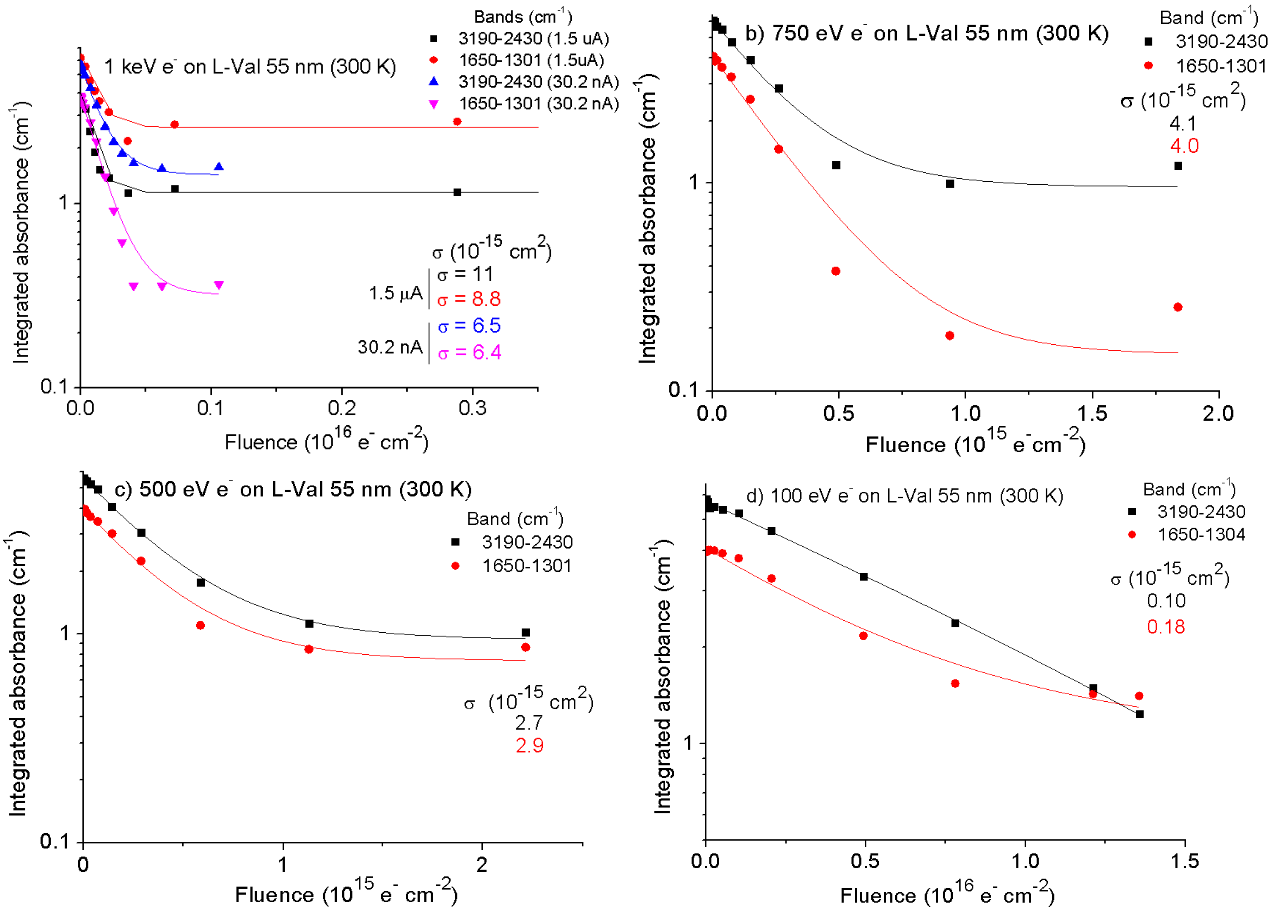

Figure 4.28: Integrated absorbances evolution of valine bands 3190-2430 and 1650-1301 cm^{-1} as function of electron beam fluences for the energies (a) 1000, (b) 750, (c) 500, and (d) 100 eV.

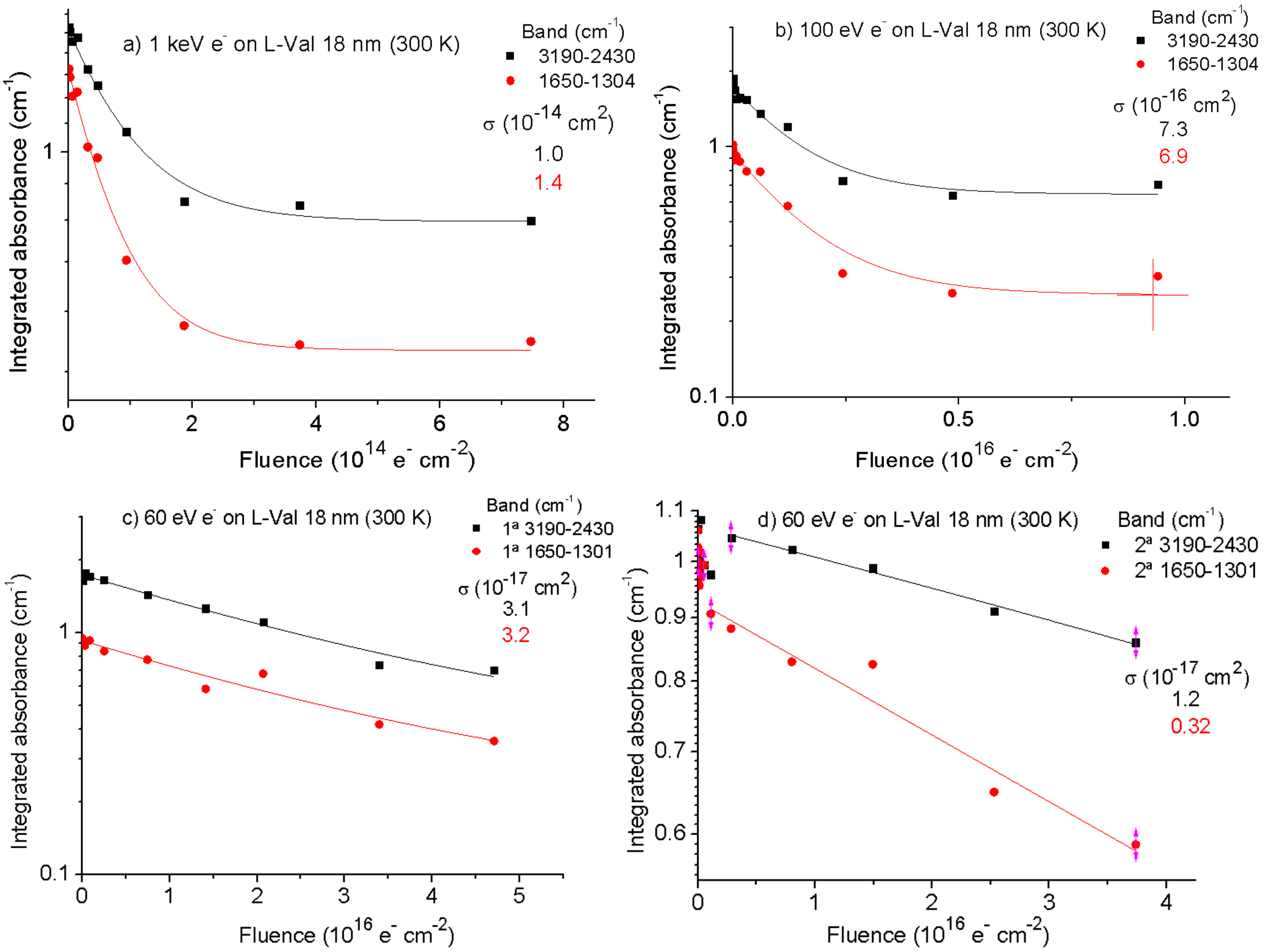

Figure 4.29: Integrated absorbances evolution of valine bands 3190-2430 and 1650-1301 cm^{-1} as function of electron beam fluences for the energies (a) 1000, (b) 1000, and (c) and (d) 60 eV.

Table 4.9: Parameters obtained from the fitting of the integrated absorbances decay with the function $S(F) = S_0 \exp(-\sigma F) + S_\infty$. Data from valine at two thicknesses irradiated by electrons at different energies.

Thickness (nm)	**Energy (eV)**	**Band (cm^{-1})**	**S_0 (cm^{-1})**	**σ (10^{-16} cm^2)**	**S_∞ (cm^{-1})**
55	1000[*]	3190-2430	3.85	11	1.16
		1650-1301	6.18	8.8	2.59
	1000	3190-2430	5.56	6.5	1.45
		1650-1301	3.83	6.4	0.32
	750	3190-2430	5.97	41	0.98
		1650-1301	3.97	40	0.15
	500	3190-2430	5.4	27	0.95
		1650-1301	3.87	29	0.75
	100	3190-2430	5.82	1.0	-
		1650-1301	4.02	1.8	1.04
18	1000	3190-2430	1.51	100	0.78
		1650-1301	1.33	140	0.48
	100	3190-2430	1.75	7.3	0.65
		1650-1301	0.97	6.9	0.25
	60	3190-2430	1.75	0.31	0.32
		1650-1301	0.95	0.32	0.19
	60	3190-2430	1.71	0.12	-
		1650-1301	0.81	0.032	-

[*] Beam current: 1.5 μA.

4.3.4
Dependence on sample temperature

Four L-valine samples ~ 60 nm thick, prepared by vacuum deposition and connected to a cold head at 300, 150, 80, and 10 K (see sections 3.2.1 and 3.4.1), were irradiated by 1.0 keV electrons and analyzed by infrared spectroscopy. Figure 4.30 shows the evolution of IR absorbance for three beam fluences on the sample at 10 K.

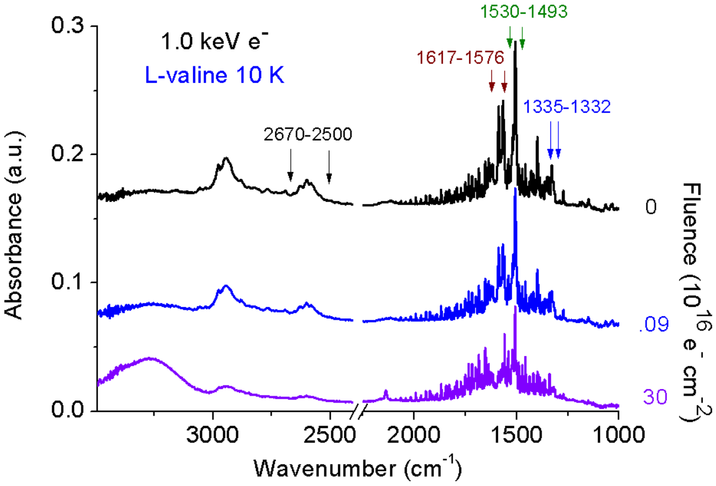

Figure 4.30: 10 K L-valine IR absorbance evolution as function of fluence of 1.0 keV electron beam.

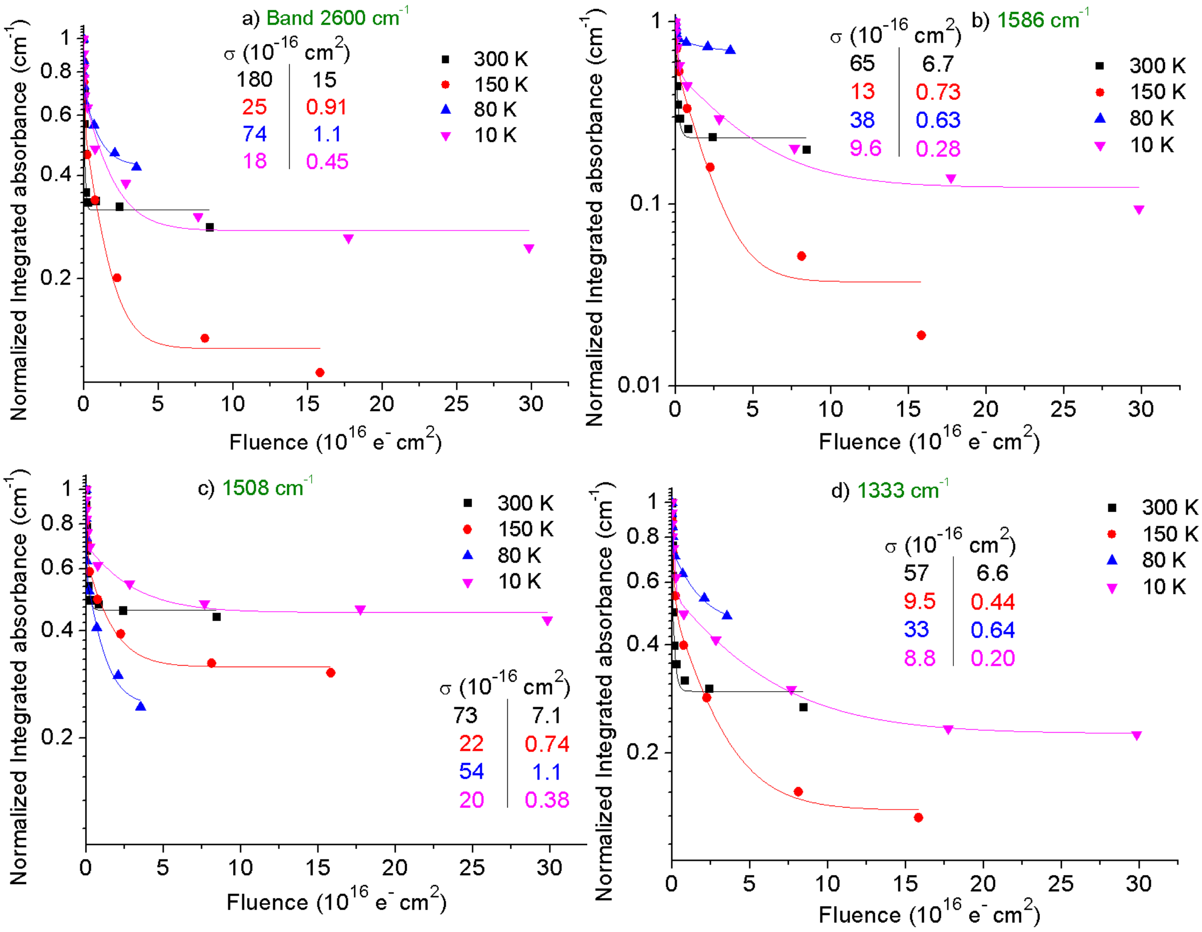

Figure 4.31: L-valine normalized integrated absorbance evolutions in function of 1.0 keV electron beam fluence for the bands: a) 2670-2500, b) 1617-1576, c) 1530-1493, and d) 1335-1332 cm^{-1} and sample temperature; 300 K (black squares), 150 K (red circles), 80 K (blue triangles) and 10 K (pink triangles).

Figures 4.31 (a)-(d) show the normalized integrated absorbance in function of 1.0 keV electron beam fluence for the 2670-2500, 1617-1576, 1530-1493 and 1335-1332 cm^{-1} bands, respectively. Analysis of the 3190-2430 cm^{-1} band was avoided because of the growing feature on the left side of the spectra due to water condensation. Table 4.10 summarizes the fitting parameters.

Table 4.10: Parameters obtained from the fitting of the integrated absorbances decay with the function $S(F) = S_1 \exp(-\sigma_1 F) + S_2 \exp(-\sigma_2 F) + S_\infty$. Data from valine at different temperatures irradiated by 1 keV electrons.

Temperature (K)	Band (cm^{-1})	S_1 (cm^{-1})	σ_1 (10^{-16} cm^2)	σ_2 (10^{-16} cm^2)	S_∞ (cm^{-1})
10	2600	0.85	18	0.45	0.28
	1586	0.92	9.6	0.28	0.12
	1508	1.5	20	0.38	0.45
	1333	0.16	8.8	0.20	0.23
80	2600	0.92	74	1.1	0.43
	1586	2.1	38	0.63	0.69
	1508	0.56	54	1.1	0.25
	1333	0.18	33	0.64	0.48
150	2600	0.71	25	0.91	0.13
	1586	1.1	13	0.73	0.038
	1508	1.6	22	0.74	0.31
	1333	0.18	9.5	0.44	0.14
300	2600	0.38	180	15	0.32
	1586	1.25	65	6.7	0.23
	1508	1.2	73	7.1	0.46
	1333	0.17	57	6.6	0.30

4.3.5

Sample crystalline state dependence

At the Van de Graaff laboratory (PUC-Rio), four L-valine samples, prepared by vacuum deposition onto ZnSe substrates, were irradiated with a 1.0 keV e^- beam at 300 K and residual gas pressure ≈ 10^{-6} mbar. Two sets of experiments were performed with two equal samples, in one of them the samples were bombarded without thermal processing, while in the second experiment the two samples were irradiated after being thermally processed in a lab oven (Nova Ética 400 – 1ND) by 90 °C (for one hour) and 100 °C (for 6 hours). Evolutions of the integrated IR absorbance in function of beam fluence are presented in Figs. 4.32 and 4.33, respectively. Table 4.11 summarizes the fitting parameters.

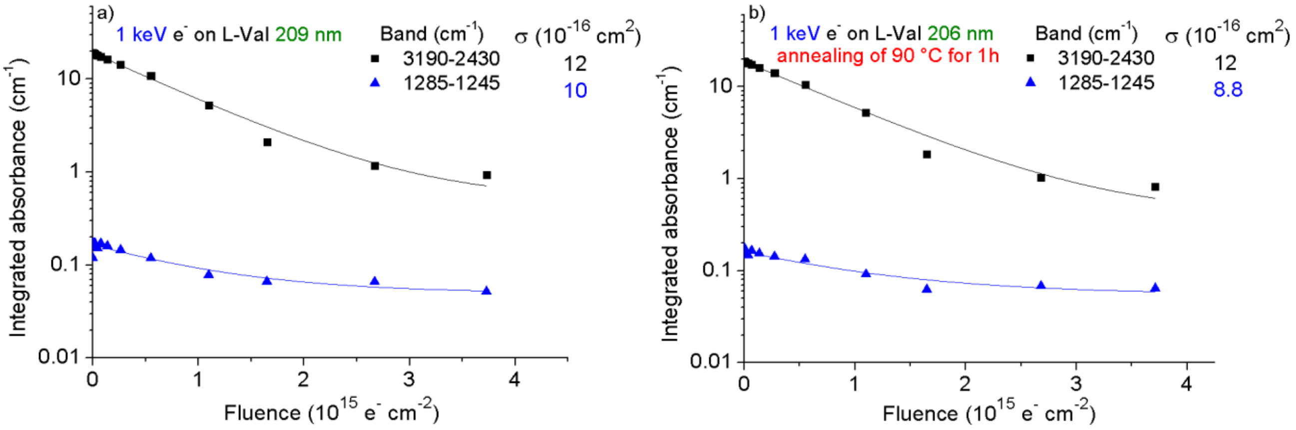

Figure 4.32: Evolutions of valine integrated absorbance with fluence of 1.0 keV e$^-$ for the 3190-2430 and 1285-1245 cm^{-1} bands: a) non-processed sample and b) sample annealed at 90 °C for 1 hour.

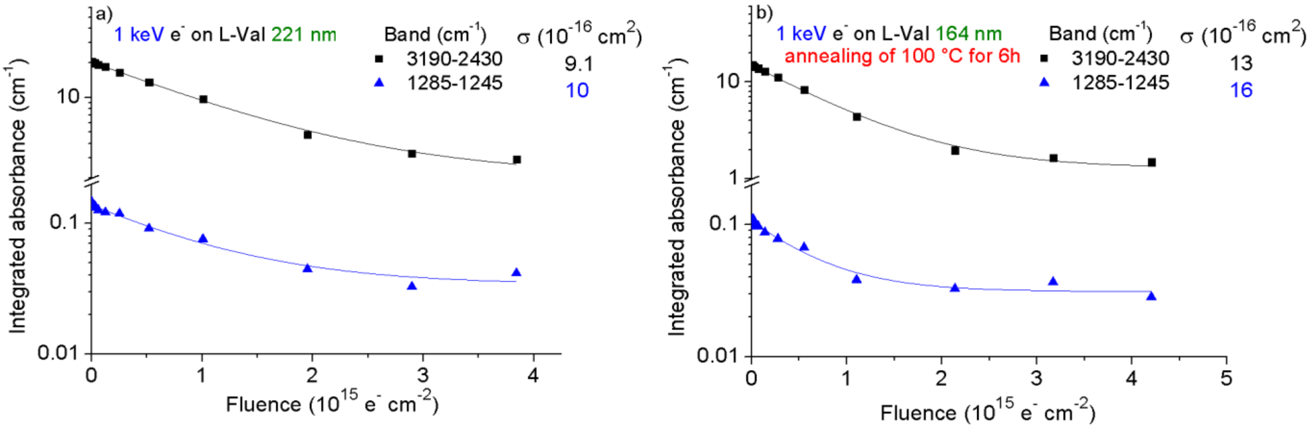

Figure 4.33: Evolutions of the integrated absorbance of valine with fluence of 1.0 keV e$^-$ for the bands 3190-2430 and 1285-1245 cm^{-1} of a) non-processed sample and b) sample annealed at 100 °C for 6 hours.

At UFBA (Universidade Federal da Bahia), two L-valine samples, prepared by drop casting deposition onto ZnSe substrates (see section 3.2.2), were bombarded by 2.0 keV electrons at 300 K and p ≈ 10^{-6} mbar. One of the samples was heated in a lab oven (JUNG, model 0912) at 100 °C for one hour; the results of the evolutions with fluence of non- and processed samples are shown in Figure

4.34. The thermal processing of one of the samples sublimated part of the material, which is the reason why absorbances at Fig. 4.34 (b) are lower. Table 4.12 summarizes the fitting parameters.

Table 4.11: Parameters obtained from the fitting of the integrated absorbances decay with the function S(F) = S_0 exp(-σF) + S_∞. Data from glycine irradiated by 1 keV electrons.

Thickness (nm)	**Band (cm^{-1})**	**S_0 (cm^{-1})**	**σ (10^{-16} cm^2)**	**S_∞ (cm^{-1})**
209	3190-2430	19.2	12	0.50
	1285-1245	0.12	10	0.050
206*	3190-2430	18.9	12	0.40
	1285-1245	0.18	8.8	0.055
221	3190-2430	20.3	9.1	2.1
	1285-1245	0.15	10	0.034
164*	3190-2430	15.0	13	1.3
	1285-1245	0.10	16	0.031

*Annealed sample.

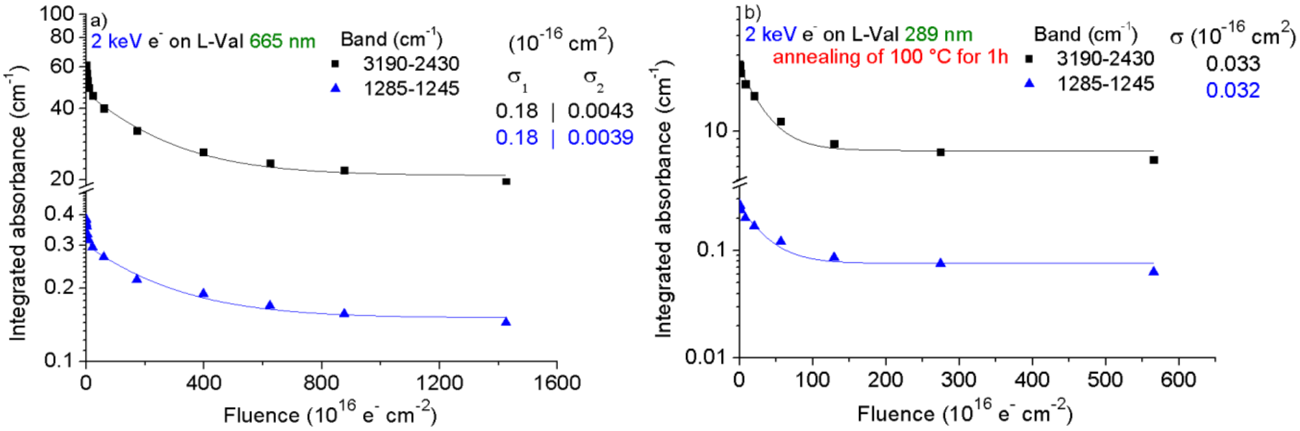

Figure 4.34: Evolutions of the integrated absorbance of valine with fluence of 2.0 keV e^- for the bands 3190-2430 and 1285-1245 cm^{-1} of a) non-processed sample and b) sample annealed at 100 °C for 1 hour.

Table 4.12: Parameters obtained from the fitting of the integrated absorbances decay with the function $S(F) = S_0 \exp(-\sigma F) + S_\infty$. Data from glycine irradiated by 2 keV electrons.

Thickness (nm)	Band (cm^{-1})	S_0 (cm^{-1})	σ (10^{-16} cm^2)		S_∞ (cm^{-1})
665	3190-2430	61.0	0.18	0.0043	20.8
	1285-1245	0.38	0.18	0.0039	0.15
289*	3190-2430	26.5	0.033		7.6
	1285-1245	0.27	0.032		0.076

*Annealed sample.

4.3.6
Glycine

An α-glycine sample, ~150 nm thick prepared by vacuum deposition on a KBr substrate (see section 3.2.1), was irradiated by 1.0 keV electrons at 300 K and residual gas pressures ≈ 5 x 10^{-7} mbar. Fig. 4.35 presents the integrated absorbance evolutions with fluence of the 2663-2392, 2179-2095, 1350-1315, 1158-1092 and 1047-1016 cm^{-1} bands. Table 4.13 summarizes the fitting parameters.

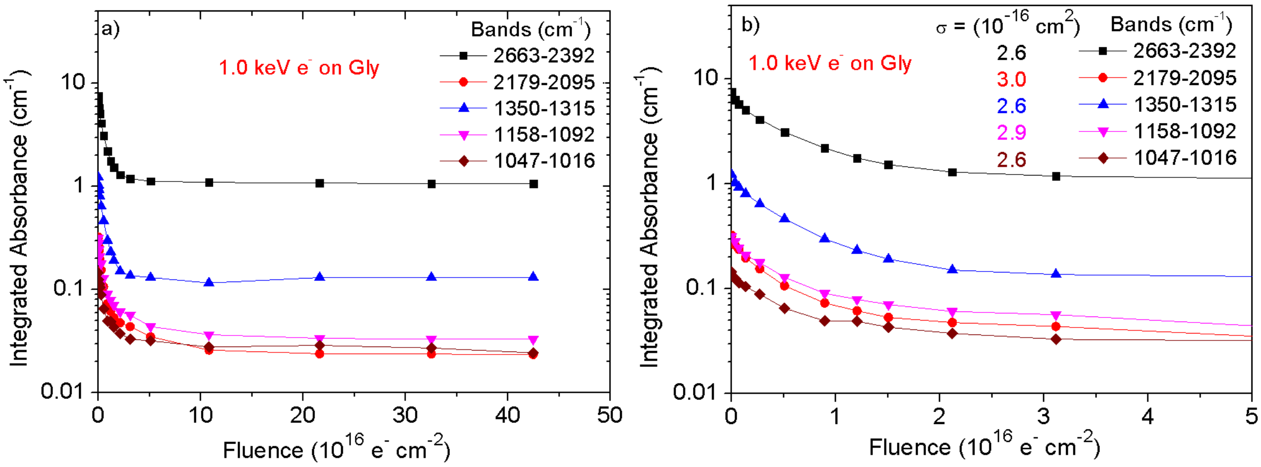

Figure 4.35: Evolutions of integrated absorbance with 1.0 keV e⁻ beam fluence of five selected glycine bands: a) high fluence spectra and b) zoom of region of low fluences [54].

Table 4.13: Parameters obtained from the fitting of the integrated absorbances decay with the function $S(F) = S_0 \exp(-\sigma F) + S_\infty$. Data from glycine irradiated by 1 keV electrons.

Band (cm^{-1})	**S_0 (cm^{-1})**	**σ (10^{-16} cm^2)**	**S_∞ (cm^{-1})**
2663-2392	7.54	2.6	1.36
2179-2095	0.325	3.0	0.039
1350-1315	1.23	2.6	0.17
1158-1092	0.318	2.9	0.067
1047-1016	0.145	2.6	0.039
Average σ_d^{ap}		2.7 ± 0.2	

5

Electron beam simulations

In order to investigate the interaction of keV electrons with atoms in a solid, the version 2.51 of the code CASINO (monte CArlo SImulation of electroN trajectory in sOlids) [58] was employed to predict the behavior of valine samples processed by keV electron beams. CASINO is commonly applied on scanning electron microscopy [59], although it can also be used in damage profile modelling (e.g., [21]).

Particularly for this work, CASINO is very useful. On the one hand, the code allows or outputs: i) the selection of energy, incidence angle, and diameter of the beam; ii) a quite wide sample specification, such as stoichiometry, density, mixed materials or multilayer structure; iii) a detailed description of the electron trajectories inside the solid; iv) the deposited beam energy as a function of depth; and v) the penetration distribution. On the other hand, the main limitation is that the code does not take into account processes that modify samples when bombarded by keV electrons: radiolysis, sputtering and molecular rearrangements. In other words, for CASINO, regardless of the beam fluence, the target is always considered virgin (unprocessed by irradiation).

In this chapter, simulations for the amino acid valine in its pure state and in analogue spatial conditions (illustrated for a mixture of icy water and CO_2 layers over a SiO_2 substrate) are presented. In order to bypass the problem of samples being modified by the impinging beam, we have developed a model based on CASINO, which is the reason why it is referred here as “CASINO-extended”. The algorithm represents an adiabatic process, which is equivalent of running CASINO multiple times but, after each cycle, the sample slightly changes according to the effects caused by the energy deposited in the previous cycle (see section 5.2).

In a first approach, only radiolysis is considered. Sputtering effects will be discussed in Chapter 6.

5.1
Simulations for valine

Degradation of valine samples by 0.25, 0.50, 1.0, 2.5, 5.0 and 10 keV electron beams were simulated by using the CASINO code; 5 x 10^6 projectiles have been employed in each run. Calculations were performed in analogue laboratorial conditions; the relevant settings are: ρ = 1.32 g cm^{-3} as the valine density, $C_5H_{11}NO_2$ the stoichiometry, 40° the beam incidence angle (with respect to the normal) and $E_{min} \equiv 50$ eV the selected minimum projectile energy necessary to cause any damage at the end of the collision cascade. Deposited energy distributions on depth are insensitive to the beam radius. As an example, Fig. 5.1 presents predictions corresponding to a 45 nm thick valine placed over a ZnSe substrate bombarded by 1.0 keV electrons; 5.1 (a) shows the electrons trajectories while 5.1 (b) presents the deposited energy gradient in the sample.

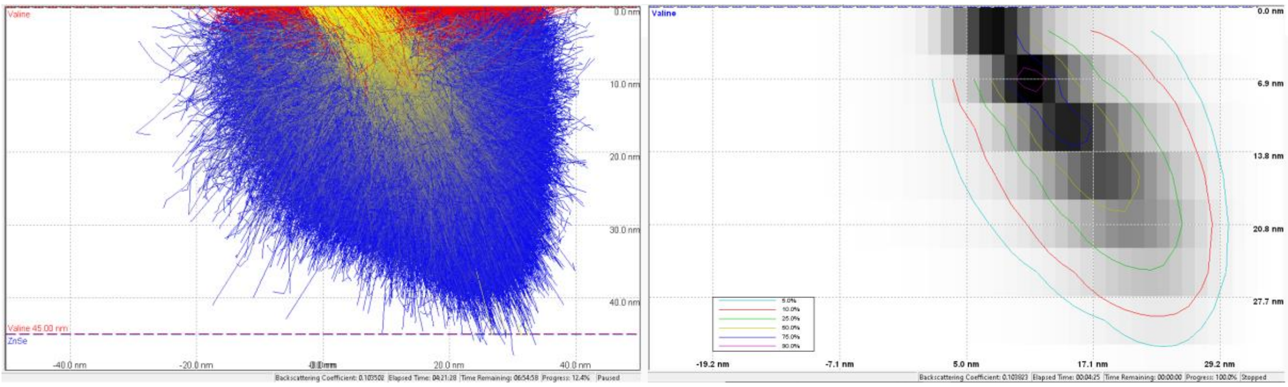

a) b)

Figure 5.1: CASINO simulation of a 45 nm thick valine over ZnSe substrate: (a) Electron trajectories projected in the XZ plane for E_0 = 1.0 keV and θ = 40°. The yellow (central) and blue (peripheral) regions correspond to high and low projectile electron energies, respectively. The red trajectories correspond to future backscattered electrons (~10%). (b) Bi-dimensional deposited energy distribution. The gray gradient indicates the fraction and where the projectile energy was transferred to the sample. Contour lines encompass the regions receiving 5, 10, 25, 50, 75 and 90% of the incident beam energy.

One of CASINO's outputs is the Cathodoluminescence intensity as a function of depth, CL(z), which we assume to be proportional to the deposited energy along the electron trajectories. Simulations were done with a beam radius of 10 mm to cover the entire sample, although in Fig. 5.1 (a) the used beam radius was 10 nm just to emphasize the balloon shape volume that narrow beams spread out inside the sample as they are decelerated. A quite realistic trajectory simulation inside a sample is shown in Fig. 5.2 (a), where the surface is traversed by a beam having a relatively large diameter. Compared to penetration Fig. 5.2 (b) makes clear that the beam radius does not play a vital role on the energy distribution per depth z because, in (these) Monte Carlo simulations, electron trajectories are independent of each other.

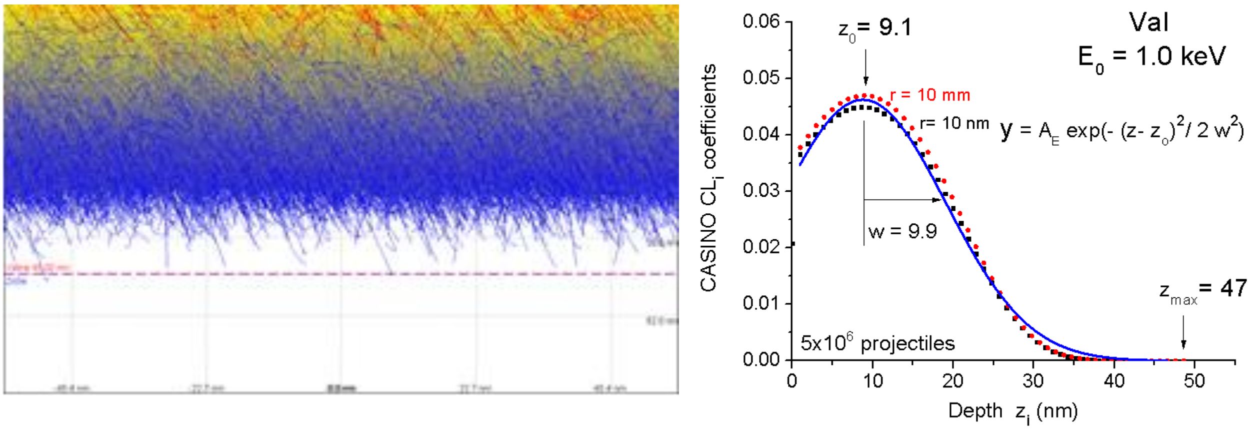

a) b)

Figure 5.2: (a) CASINO simulation of a 45 nm thick valine over ZnSe substrate: Electron trajectories projected in the XZ plane for E_0 = 1.0 keV,θ = 40° and r = 10 mm. (b) CL_i coefficients versus i, the sublayer index, transformed into z_i, the sublayer depth. Red circles and black squares are CASINO CL(z_i) distributions corresponding to beam radii of 10 mm and 10 nm, respectively. Blue line represents the deposited energy density distribution obtained by fitting $CL_i(z_i)$ data with a Gaussian function. w is the standard deviation and z_0 the depth of the maximum deposited energy density. The area under this function, for $0 \leq i \leq i_{max}$, is normalized to 1.

The region processed by the beam is divided into i_{max} sublayers, so that the depth of the i^{th} sublayer is given by $z_i = i\Delta z$, where Δz is the sublayer thickness and i an integer running from 1 to i_{max}. The $CL_i(z)$ energy fraction coefficients are defined as the ratio between E_i, the average energy deposited in the sublayer i, and the incident energy, E_0: $CL_i = E_i/E_0$. In other words, the term $E_0 CL_i$ represents the energy transferred per projectile to the sublayer i, independently of which amount of this energy goes into the precursor's dissociation.

The distribution $CL_i(z)$ is well fitted by a Gaussian function as seen in Fig. 5.2 (b); by construction, it is normalized to 100%, in the sense that the integrated area under the curve (from i = 1 to i_{max}) is unitary. Figures 5.3 (a) and (b) present these distributions for five incident energies in function of sample depth and of the sublayer index i = $z_i/\Delta z$, respectively; the former highlights the depth with the highest energy deposition (or damage), z_0, while the latter points out the universality of the CL_i coefficients if i_{max} is the same for different energies.

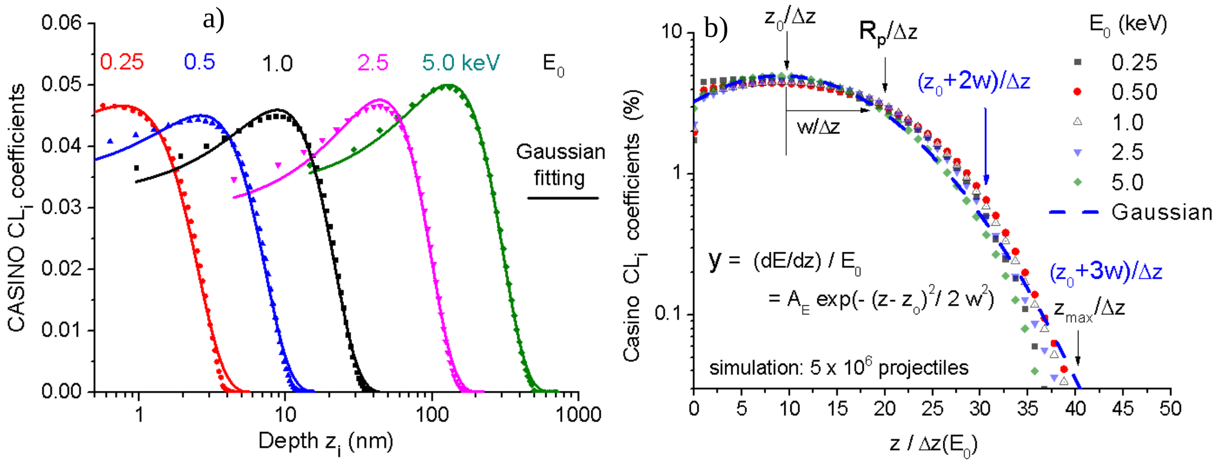

Figure 5.3: CASINO's CL_i distribution in function of (a) depth and (b) i = $z_i/\Delta z$ sublayers for valine 500 nm thick. The CASINO'S depth step Δz is obtained dividing z_{max} by the number of layers (50 in the example). Fitting parameters of these distributions are presented in Table 5.1.

Figure 5.4 presents the dependence on the initial projectile energy of the obtained Gaussian parameters: i) maximum penetration z_{max}, ii) Full Width at Half Maximum (FWHM), iii) projected range R_p, iv) standard deviation w, and v) the Gaussian center, z_0, corresponding to the depth receiving the highest energy deposition (data from Fig. 5.3). Note that $R_p \sim z_0 + w$, and z_{max} is the deepest length reached by electrons. The power law $z_k = a_k E_0^{nk}$ describes this dependence, where the a_k's are constants, k holds for z_{max}, FWHM, R_p, w and z_0, respectively, and n_k is $1.58 \leq n \leq 1.75$, or, on average, n ~ 1.6. The fitting parameters are presented in Table 5.1.

$$z_k = a_k E_0^n \qquad (5.1)$$

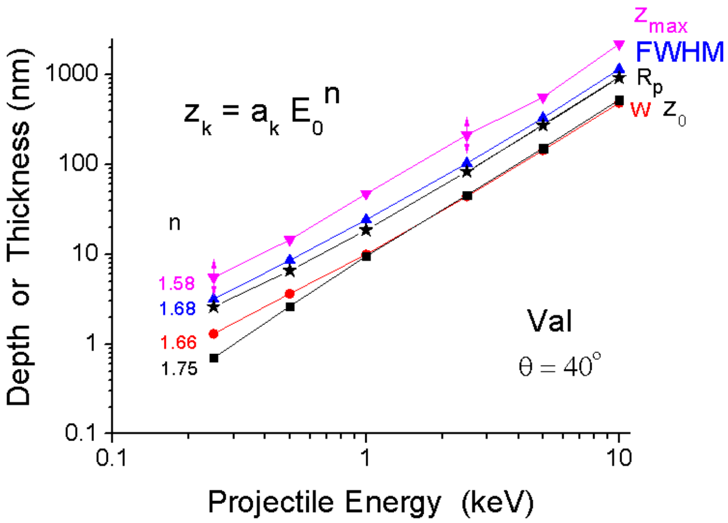

Figure 5.4: Dependence of the Gaussian parameters on the incident electron energies. All of them follow a power function law, with the exponent n ~ 1.6.

In Fig 5.4, $R_p \approx 2z_0$, which on average means that: i) most of the projectiles stop in a sublayer twice deeper as the highest damaged sublayer; and ii) $w \sim z_0 \sim z_{max}/4$, which shows that, although unlikely, the precursor molecules located four times deeper than z_0 may still be destroyed. The interface region is then limited by $R_p \sim z_0 + w$, and by $z_{max} \sim 2R_p \sim z_0 + 3w$. In the present work, the thickness $z_{int} = z_0 + 3w$ represents ≈ 99.5 % of $\sum_i CL_i$, which is used to define N_{max}. This definition is better than $z_{int} = z_{max}$ in the sense that z_{max} is the deepest precursor dissociation, a value not well defined because, in general, it increases when the number of projectiles in the simulation increases and is defined by a small number of events. $N_{max} = (N_A\rho/M)\, z_{max}(E_0)$, where $z_{max}(E_0) = z_{max}(\text{for } E_0 = 1 \text{ keV})\, E_0^{1.5}$.

Table 5.1. Parameters of the Gaussian functions obtained from fitting CASINO CL distribution outputs (Fig. 5.3) for valine film, 500 nm thick. Normalization: $\boldsymbol{\int_0^1 A_E\ exp\left(-\frac{(z-z_0)^2}{2\,w^2}\right) d\left(\frac{z}{z_{max}}\right) = 1}$; less than 10% error is expected on z_{int} calculations.

Projectile Energy (keV)	**A_E (0.01 z_{max} /Δz)**	**z_0 (nm)**	**w (nm)**	**z_{int} (nm)**	**FWHM (nm)**	**z_{max} (nm)**	**Δz (nm)**	**N_{max} (10^{16}Molec cm^{-1})**
0.25	0.02391	0.7	1.3	5.0	3.16	5.5	0.113	0.21
0.50	0.02283	2.6	3.6	14	8.58	15	0.315	0.64
1.0	0.02314	9.1	9.9	40	24.2	47	0.950	2.0
2.5	0.02381	45	44	180	103	213	4.435	8.9
5.0	0.02593	143	140	580	330	560	14.57	28

5.2
CASINO-extended model

Destruction cross section data of amino acids bombarded by keV electrons are very disperse in literature; e.g., see Pilling et al. (2014) [24] and Maté et al. (2015) [25]. Both groups analyzed glycine degradation by 2 keV electrons, at room temperature, and found destruction cross sections that differ up to a factor ~50. It should be paid attention that the sample thickness is very different in their experiments: 3.5 µm for Pilling et al. (2014) [24] and 90 nm for Maté et al. (2015) [25]; in addition, as can be inferred by Fig. 5.3, the maximum penetration for a 2 keV electron beam is about z = 100 nm.

This section is divided in two subsections: i) an introduction on the meaning of cross sections for thin and thick targets; and ii) the fundaments of the proposed CASINO-extended model, in an attempt to describe the radiolysis and sputtering of thick targets, especially those where electrons cannot traverse. In practice, the goal is to build a model to compare the column density evolutions with beam fluence, N(F), for experimental and theoretical data. By doing this, a better understanding of the interaction of keV electrons with atoms in a solid is achieved.

5.2.1
Average cross sections for thick targets

For the current discussion, thin samples are those traversed by a beam with low kinetic energy loss; that is, the beam exits the sample with a velocity slightly (~ 2%) lower than the incident one. Thick targets are the ones for which the projectiles transfer all or substantial fraction of their kinetic energy to the sample. In particular, sample degradation stops when the collision energy becomes lower than E_{min} (typically around 50 eV) when molecular dissociation or ionization are unlikely. For thin targets, the destruction cross section σ is written as:

$$\sigma(E_0) = \frac{1}{N(F)}\frac{dN}{dF} \tag{5.2}$$

in words, the cross section is the relative column density rate with fluence: dN is the number of dissociated molecules by sample unit area, dF the number of projectiles, N the number of dissociable molecules by sample unit area. The term 1/N(F) takes away the dependence of σ on sample thickness, which is equivalent of saying that it is the same cross section for binary collisions.

For thick targets, the situation is quite different. Not only the projectile's energy changes after each collision, but also its direction. As a consequence, the projectile flux varies with depth; in particular, the flux usually is enhanced at the first sublayers due to backscattered projectiles (~ 10% higher for keV electrons). For each i sublayer, an average cross section σ_i needs to be considered and a thick target average, σ_{av}, is calculated for the ensemble of sublayers. This reasoning guides the model's algorithm: the thick target is divided into i_{max} thin sublayers, each one having the thickness $\Delta z = z_{max}/i_{max}$. The thick target average cross section is then defined:

$$\sigma_{av}(E_0, \mathrm{F}) = \left(\frac{1}{i_{max}}\right) \Sigma_1^{imax} \sigma_i = \left(\frac{1}{i_{max}}\right) \Sigma_i \frac{1}{N_i(F)}\frac{dN_i}{dF} \tag{5.3}$$

with N_i being the column density of the i sublayer and F is the fluence of the incident beam in the first sublayer. It is crucial to note that σ_i contains information of all trajectories that transfer energy to this layer, that is, collision energies, projectile local directions and fluxes. N_i depends on depth z for non-homogeneous samples; moreover, even for homogeneous samples, N_i becomes z-dependent because – in general – degradation is not uniform when fluence increases. The important consequence is that, contrarily to thin films, σ_{av} is fluence dependent: it is not unique for a given E_0.

Calling N_{max} the maximum number of molecules that can be processed, for homogeneous samples at the beginning of irradiation, $N_i \sim N_{max}/i_{max}$. Eq. (5.3) then becomes very similar to Eq. (5.2):

$$\sigma_{av}(E_0) = \left(\frac{1}{N_{max}}\right)\frac{(\Sigma_i dN_i)}{dF} \tag{5.4}$$

Experimentally, we measure $\Sigma_i dN_i$ and not each individual N_i, which makes clear the difficulty of measuring σ_{av} accurately. If the target is thick, it is necessary to know which N_i's are contributing to $\Sigma_i dN_i$, otherwise σ_{av} becomes target- thickness dependent. In fact, it is not an easy task to precisely determine either N_∞ or N_{max}, fixing the interface between the beam processed region and the non-irradiated one (the interface spreads out over a depth interval, due to an exponential-like decay behavior of the projectile's deposited energy). Fig. 5.3 (b) illustrates the effect of the interface inaccuracy on σ_{av} systematic errors: the processed column density, defined as $N_{proc}(F) = \Sigma_i N_i(F)$, can be easily increased by a factor 2, while $\Sigma_i dN_i$ only increases a few percent.

The cross section σ_{av} is usually measured by FTIR via the absorbance evolution with fluence of the bands, S(F), which can be rewritten, according to Beer-Lambert's Law, $N(F) = \ln(10)\frac{S(F)}{A_v}$, in terms of the column density of the whole sample, $N_{sp}(F)$:

$$N_{sp}(F) = N_{max}e^{-\sigma_d^{eff}F} + N_\infty \tag{5.5}$$

Regardless of the microscopic considerations on the destruction cross section calculation, this expression shows that an effective cross section, σ_d^{eff}, can be extracted from fitting experimental data. In particular, the determination of σ_d^{eff} depends on the correct determination of N_∞. At high fluences, $N_{sp}(F)$ levels off at N_∞ because the region beyond N_∞ is not processed by the beam. Two problems appear: i) often, experiments are relatively short (they are stopped before the N(F) levells off), and ii) even for long measurements (at least for electrons on thick targets), the levelling off happens too slowly. Both issues cause mistakes on σ_d^{eff}. Aiming the understanding of the N(F) evolution, the presently proposed model is a microscopic algorithm based on CASINO.

5.2.2

CASINO-extended model for beam-modifying molecular thick targets

Based on Eq. (5.4) and considering only radiolysis, the proposed CASINO-extended model predicts the maximum value of the averaged destruction cross section for virgin samples to be σ_0:

$$\sigma(E_0, \theta) \equiv \sigma_0 = \frac{1}{N_{max}(E_0, \theta)} \frac{E_0}{D_0} \tag{5.6}$$

where D_0 is the energy necessary to dissociate in average one precursor molecule of the target, and E_0 is the projectile initial energy. N_{max}, the maximum column density of processable molecules, depends on the beam range, which in turn depends on the incident energy and angle. σ_0 is the maximum possible destruction cross section because the introduction of other processes (sputtering, crystalline modifications, heating, electronic excitations without molecular dissociation, etc.) decreases the energy available for dissociation. $E_0 - E_{min}$ is the available energy for molecular dissociation once this process stops for energies lower than E_{min}. Rewriting Eq. (5.5) with $N_\infty = N_0 - N_{max}$ and adding up the contribution of each sublayer i one obtains:

$$N_{sp}(F) = N_0 - N_{max} + \sum_{i=1}^{i_{max}} N_i\,(F) = N_0 - N_{max}\left[1 - \sum_{i=1}^{i_{max}} \frac{\Delta z_i}{z_{max}} e^{-\sigma_i F}\right] \tag{5.7}$$

with Δz_i and σ_i being the thickness and the destruction cross section of sublayer i, respectively; $\sigma_i = \sigma_0 i_{max} CL_i$, so σ_i is calculated from the net cross section, σ_0, multiplied by the total number of sublayers (region where the beam loses all its energy), i_{max}, and the fraction of energy deposited on that particular layer, represented by CL_i. CASINO's CLi outputs are normalized to 100% ($\sum_{i=1}^{i_{max}} CL_i =$ 100%). A schematic drawing of the column densities of Eq. (5.7) is displayed in Fig. 5.5:

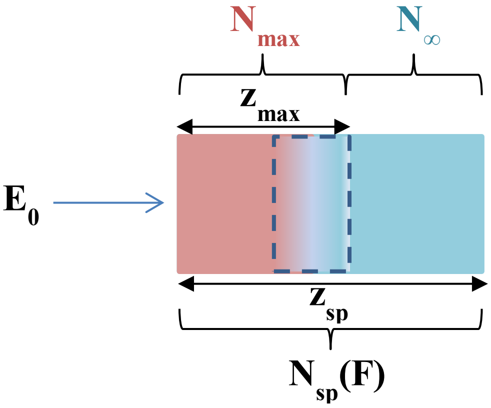

Figure 5.5: Representation of the column densities during the processing of a sample. N_{max} being the maximum number of molecules per cm^2 that can be processed (according to beam range), $N_{sp}(F)$ the column density of the entire sample at fluence F, N_0 the column density at F = 0, $N_\infty = N_0 - N_{max}$ (or the column density of the molecules that will never be dissociated). The dashed rectangle depicts the interface region between processable and rear region.

Equation (5.7) is the skeleton of the model. The next step is to predict σ_i which has to be related with the energy delivered to the ith sublayer. CASINO is invoked to perform this task, providing the CL_i and z_{max} outputs. Based on the code's results, $N_{sp}(F)$ is calculated for selected valine thicknesses and for several energies. Results are compared to the experimental data for electron beams presented in the previous chapter (Section 4.3).

Simplifications considered in the model:

i) Large radius beams (10 mm) were set in the simulations, so the target XY plane is homogeneously processed; consequently, only the depth Z dependences are analyzed.

ii) N_{max} depends on the maximum depth, z_{max}, according to the beam energy; therefore, the model considers the column density for the $z > z_{max}$ region as corresponding to a virgin material. This is relevant because the IR beam traverses the entire sample and is absorbed by the processed and virgin parts; the comparison with real data requires that the non-processed part needs to be included for thick targets.

iii) Sample stoichiometry does not change with fluence. Since, at this stage, the model does not take sputtering or the production of volatile daughter species into account, the number of atoms of each atomic species in the sample remains the same. It must be reminded that

CASINO simulates the interaction between electron-atom and not electron-molecule; thus, even if the sample structural configuration changes, for the code, the sample is always virgin.

iv) The calculation is performed sublayer by sublayer. If sputtering is considered, the first sample sublayer is ejected and the new distribution CL_i should be exactly the same as before if the origin of z is redefined on the new surface.

v) The deposited energy on the layer defined between z_i and $z_i + \Delta z$ is $E_i = E_0 CL_i$. The deposited energy not used to dissociate precursor molecules must go to other phenomena: dissociation of products, chemical reactions, increase of temperature etc. Equations treating these cases may be further included in the model.

vi) To describe the dependence on E_0, CL_i is parameterized by a Gaussian function $CL_i(z) = A_E \exp[-(z-z_0)^2/2w^2]$ with z_0 and $(z-z_0)$ varying according to $z_k = a_k E^{nk}$, as shown in Fig. 5.4 and Eq. (5.1) for valine and $\theta = 40°$. A_E values are presented in Table 5.1 for some energies. Because the CL_i coefficients are normalized to 1 for all incident energies, the A_E values present low sensitivity to E_0 if i_{max} is always the same.

Defining z_{sp} as the actual sample thickness, the column density is given by

$$N_{sp} = \frac{z_{sp}}{V_{molec}} = \frac{N_A \rho}{M} z_{sp} \tag{5.8}$$

with V_{molec} being the volume of the precursor molecule, ρ the density, N_A the Avogadro's number and M the molecular weight. The projectiles penetrate until z_{max}, which increases with E_0 and decreases with θ.

The model describes the radiolysis effect in each sublayer. The number of precursors per unit area on the layer between z and z + dz, at fluence F, is $\frac{\partial N(z,F)}{\partial z} dz$ and, as new projectiles arrive, $\frac{\partial^2 N(z,F)}{\partial z \partial F}$ molecules per layer and projectile are destroyed. Considering the total energy deposited in the layer at depth z due to all collisions, the local destruction cross section, $\sigma_{av}(z)$, is defined by the relationship

$$\frac{\partial^2 N(z,F)}{\partial z \partial F} = -\sigma_{av}(z)\frac{\partial N(z,F)}{\partial z} \tag{5.9}$$

Assuming that the projectile trajectories in the solid are independent, this equation can be solved for F for that layer:

$$\frac{dN(z,F)}{dz} = \frac{dN(z,0)}{dz}e^{-\sigma^{av}(z)F} \tag{5.10}$$

This result establishes that the precursor concentration, dN/dz, in each layer evolves exponentially with its own $\sigma_{av}(z)$. Integrating over all sublayers, from z = 0 up to the processable depth z_{max}, the evolution of N is obtained:

$$N_{sp}(F) = \int_0^{z_{max}} \frac{dN(z,0)}{dz}e^{-\sigma^{av}(z)F}\,dz + N_\infty \tag{5.11}$$

Particular cases

i) Self-supported thin samples (without substrate)

Since the beam traverses the sample, Eq. (5.11) becomes

$$N_{sp}(F) = \int_0^{z_{sp}} \frac{dN(z,0)}{dz}e^{-\sigma(z)F}\,dz \tag{5.12a}$$

$$\sigma(z) = \frac{1}{D_0}\left(\frac{dE}{ds}\right) = S_e(z)\frac{M}{N_A \rho D_0 cos\theta} \tag{5.12b}$$

where the length s is measured along the projectile trajectory.

For very thin samples, just a single layer Δz exists:

$$N_{sp}(F) = N_0 e^{-\sigma_1 F} \tag{5.13}$$

In this case, $N_0 = N_{max}$ and the dependence of σ_1 on the initial energy E_0 is the same as that of the electronic stopping power $S_e(E_0)$, as seen in Fig. 5.6 for valine:

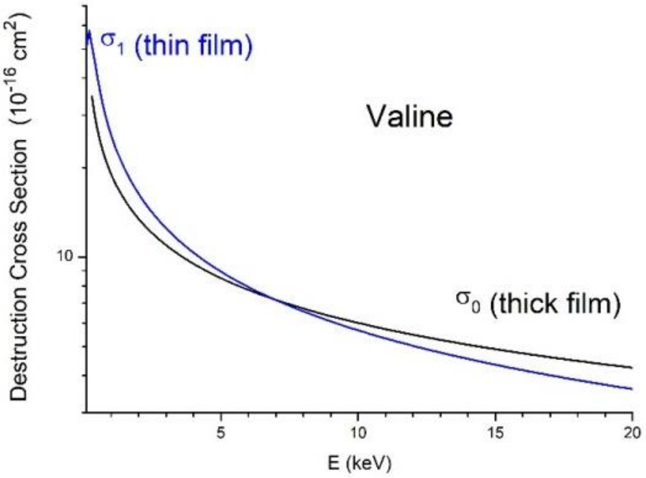

Figure 5.6: Comparison between the destruction cross section of virgin thin films, σ_1, and the average destruction cross section of virgin thick samples, σ_0; where maximum means that all the projectile energy goes to the degradation of precursors.

ii) Initially uniform thick sample

$$N_{sp}(F) = \frac{N_{max}}{z_{max}} \int_0^{z_{max}} e^{-\sigma^{av}(z)F} dz + N_\infty$$

$$N_{sp}(F) = \sum_{i=1}^{i_{max}} N_i(F) + N_\infty = N_0 - N_{max}\left[1 - \frac{\Delta z}{z_{max}} \sum_{i=1}^{i_{max}} e^{-\sigma_i F}\right] \qquad (5.14)$$

with $\frac{\Delta z}{z_{max}} = i_{max}$ being the normalization factor, and $\sigma_i = \sigma_0 i_{max} CL_i$ as proposed in the model. Results of partial normalization of $N_i(F)$ to 10 sublayers are shown in Fig. 5.7.

At low fluences, the sublayers i = 3, 2, 4 and 5 hold for the intense variations of $N_{sp}(F)$, since they have the largest CL_i values. For high fluences, the processed region close to the surface is practically depleted of precursors. Only the sublayers far from the surface, having low CL_i coefficients, are able to contribute to the $N_{sp}(F)$ variations and, progressively, impose lower dissociation rates. The fact that dN_i/dF goes into a maximum for i = 3 (in this case) has a practical consequence: a few sublayers around i = 3 dominate the processing at the beginning of the irradiation; the average of their σ_i is approximately constant during this fluence interval, so that dN/dF is also approximately constant: N(F) decreases with an apparently fixed cross section. Once the fast precursor dissociation is achieved for front sublayers, only the slow processing of the rear (interface) sublayers is observed: the N(F) “elbow” indicates this transition (Fig. 5.7).

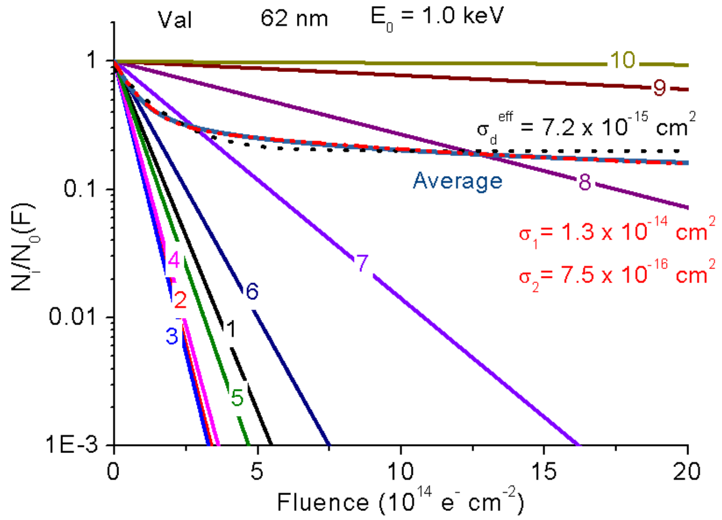

Figure 5.7: Evolution with fluence of the normalized column density of each i layer, $N_i(F)/N_i(F=0)$. Simulation for 62 nm Val film irradiated by 1 keV electrons. The blue curve is the average contribution of 10 layers, and it is fitted by the functions exp ($-\sigma_d^{eff}$ F) + N_∞/N_{max} (blackdotted curve), fixing $N_\infty = N_{max}/5$, and exp ($-\sigma_1$ F) +exp ($-\sigma_2$ F) + N_∞/N_{max} (red dashed curve), fixing $N_\infty = N_{max}/10$.

$N_{proc}(F)$ is the sum of all $N_i(F)$ during irradiation; it starts at N_{max} and tends to zero when F ⟶ ∞. In Fig. 5.7, $N_{proc}(F)$ is represented by the dashed curve as the average of all N_i’s. In this limited range of fluences, $N_{proc}(F)$ seems to level off, which is well fitted by Eq. (5.5) with F = 2 x 10^{15} e^- cm^{-2}. Imposing $N_{max}/N_\infty = 1$, σ_{av} = 7.2 x $10^{-15}$$cm^2$ is obtained. Considering statistical fluctuations, experimental $N_{sp}(F)$ should also be fitted by Eq. (5.5), leading to the conclusion that the destruction cross section is constant; as a reference, the σ_i’s of the first 4 layers of Fig 5.7 are σ_3 = 2.1, σ_2 = 2.0, σ_4 = 1.9 and σ_5 =1.5 x 10^{-16} cm², respectively.

Although CL_i values depend on the beam incidence angle θ, this does not affect the algorithm because CASINO takes into account this dependence, as well as that of the backscattered electrons. For thin samples, the substrate and the transmitted electrons are also considered. Eq. (5.9) can also be generalized to describe the irradiation products; in this case, a series of growing exponentials appears as a solution [60]. By construction, daughter species are formed and destroyed more frequently in the depths corresponding to high CL_i values.

Figure 5.6 shows how σ_0 evolves with the increase of the initial projectile energy, E_0. From Eqs. (5.6) and (5.8): $N_{max}(E_0, \theta) = (N_A\rho/M)\, z_{int}(1\ \text{keV})\, E_0^{1.64}$, where $z_{int}(1\ \text{keV})$ is the processable region thickness for $E_0 = 1$ keV.

$N_{sp}(F)$ was calculated for valine bombarded by 1 keV electrons using Eq. (5.7). The sample was divided into 10 slices of thickness $\Delta z = 4.8$ nm. Figure 5.7 presents $N_{sp}(F)$ for each of those 10 sublayers and their average. A clear conclusion from Eq. (5.7) is that $N_{sp}(F)$ does not have a single defined destruction cross section because this quantity varies with depth within the sample, $\sigma(z)$. However, the overall behavior is similar to the decay $N_{sp}(F) = N_{max} \exp(-\sigma_d^{eff}F) + N_\infty$, Eq. (5.5).

Figure 5.8 displays the same data as Fig. 5.7, but instead of fluence, the abscissa is depth - to highlight the inhomogeneity of the damage caused by the beam. In Fig. 5.8 (a), $N_i(F)/N_i(0)$ is presented as a function of sample depth for fluences varying with 10^{14} e^- cm^{-2} steps. The points to be noted are: i) $N_i(F)/N_i(0) = 1$ initially and decreases exponentially with fluence; ii) $N_i(F)/N_i(0)$ decreasing rate depends on the sublayer i, so the degradation is not homogeneous with depth; iii) the degradation profile is Gaussian-like, the highest rate occurring near 10 nm deep; iv) once the region close to the surface is depleted of precursors, degradation proceeds slowly in the interface region; and v) beyond z_{max}, there is no degradation at all.

Figure 5.8 (b) presents the same features, but viewed from E_i, the projectile energy transferred to sublayer i precursor molecules. E_i is proportional to $dN_i(F)/dF = - \sigma_i N_i(F) = - \sigma_i N_i(0) \exp(-\sigma_i F)$, where $\sigma_i = \sigma_0\, i_{max}\, CL_i$. This expression shows that, at $F_{hom} = 1/\sigma_i$, $\sigma_i \exp(-\sigma_i F)$ goes into a maximum, around which the energy absorbed by precursors is the same for a large number of sublayers. Figure 5.8 (b) displays $\sigma_i \exp(-\sigma_i F)$ as a function of depth for several fluences; at $z = z_0$ and $F = F_{hom}$, the 1st and 2nd derivatives of $\sigma_i \exp(-\sigma_i F)$ are zero. The points to be noted are: i) initially, this function is proportional to CLi and decreases exponentially with rates which are also proportional to CL_i; ii) the sub layers receiving more energy are those that lose precursors faster; iii) the previous observation indicates a kind of auto-regulation process for precursors: the more energy received by a sublayer, the less precursor molecules exist in it to absorb this energy; iv) although inhomogeneously processed, at $F \sim F_{hom}$ (= 1.42×10^{14} e^-

cm^{-2}) the most active sublayers contribute with the same $dN_i(F)/dF$ to the precursor column density variation; and v) for $F >> F_{hom}$, the precursor concentrations in the superficial and central regions of the sample have decreased substantially and processing keeps going slowly at the interface region.

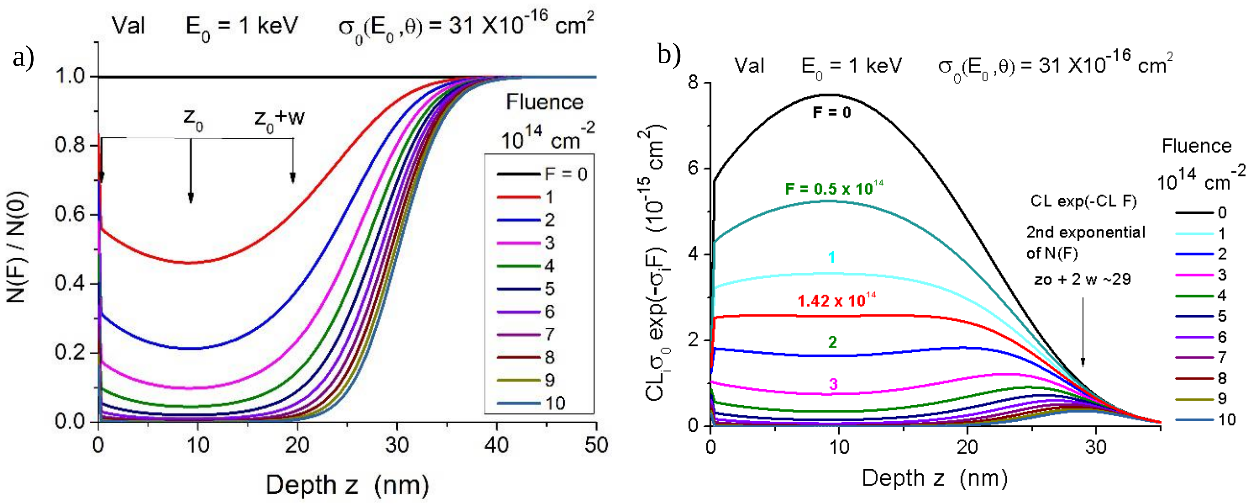

Figure 5.8: (a) Dependence of valine column density on depth, for several fluences; normalization: N(F=0) = 1. (b) Dependence of the degradation factor $CL_i\,\sigma_0 \exp(-\sigma_i F)$ with sample depth. The precursor is first depleted around 10 nm, where CL(z) is maximum. Degradation stops at $z_{max} \approx 47$ nm.

The model can be used then to analyze how $N_{sp}(F)$ evolves with the beam energy and with the target thickness, Figs. 5.9 and 5.10, respectively. It is worthwhile mentioning that this model does not have free parameters beyond the default options given by the CASINO code. The parameter D_0, not used in the code, was measured from the valine radiolysis by MeV ions [61], and it is taken as being the same for degradation by electron beams.

For five incident energies, Fig. 5.9 (a) shows the normalized $N_{proc}(F)$ calculated by the decomposition of the samples' processable region using Eq. (5.7). At low fluences, the degradation rate is intense for two reasons: i) the precursor molecule concentration is high in depths where the beam flux is also high, and ii) the average ionization cross section has its maximum value around 100 eV [62, 63]. Irradiations with E_0 close to 100 eV have the highest σ_d^{eff} values, while projectiles with higher E_0 penetrate deeply in the target and keep the processing over a larger region. When F → ∞, only the interface region is under processing; dN/dF is relatively low because the flux and the energy deposited in this region are also reduced.

Figure 5.9 (b) presents $N_{sp}(F)$, obtained by introducing $N_{max} = N(0)$ in the $N(F)/N(0)$ prediction displayed in Fig. 5.9 (a), of a 2 µm valine sample (N_{max} = 13.55 x 10^{17}molec cm^{-2}). Notice that in Fig. 5.9 (b): i) $N_{sp}(F)$ is the quantity that is experimentally measured; ii) dN_{sp}/dF increases with the projectile incident energy, E_0; iii) by construction, σ_0 decreases with E_0, therefore dN_{sp}/dF increases because N_{max} increases with E_0; and iv) in the inset, 10 keV data are well fitted by Eq. (5.5), which gives the false impression that one single exponential σ_d exists, and that it grows with the initial projectile energy.

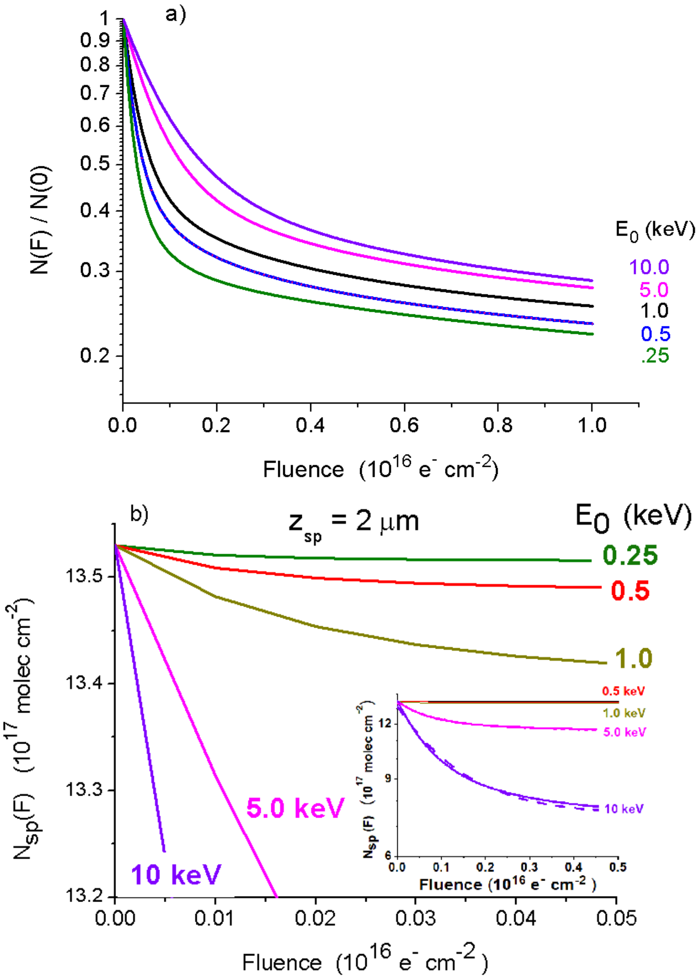

Figure 5.9: (a) Dependence of normalized valine column density on fluence for 0.25 to 10 keV beam energies; θ = 40°. Only the processed regions are considered. The "elbow" near F = 0.1 x 10^{16} corresponds to the region $z_0 \pm$ w depleted of precursors (see Fig. 5.8). (b) Same calculation as (a), but for $N_{sp}(F)$.In the inset, scales have been changed to show the 10 keV data levelling off; in

dash, the prediction for this energy is very well fitted by Eq. (5.5). Note that the sequence of slopes has been inverted.

Figure 5.10 shows the $N_{sp}(F)$ behavior of three sample thickness ranges when they are bombarded by E_0 = 1 keV electrons: i) very thin samples (z_{sp} = 5 nm), when the beam traverses the sample; ii) thin or mild thick samples (z_{sp}= 10 – 30 nm); and iii) thick samples (z_{sp}> 50 nm), when the projectiles do not reach the substrate. In the first case, the $N_{sp}(F)$ behavior is determined by one exponential, which should barely depend on the sample thickness. While, for the second, as the sample thickness increases, $N_{sp}(F)$ initially decreases faster, but then reverses this behavior, once the CL_i distribution has a maximum at z_{sp} ~ 15 nm. For thick targets, the projectile flux is very low at the deepest sublayers ($z > z_0 + w$, interface lower limit), which leads to a low molecular dissociation rate ($N_{sp}(F)$ levels off at higher fluences). This tendency qualitatively replicates the one shown in Fig. 4.27 for 1.0 keV measurement.

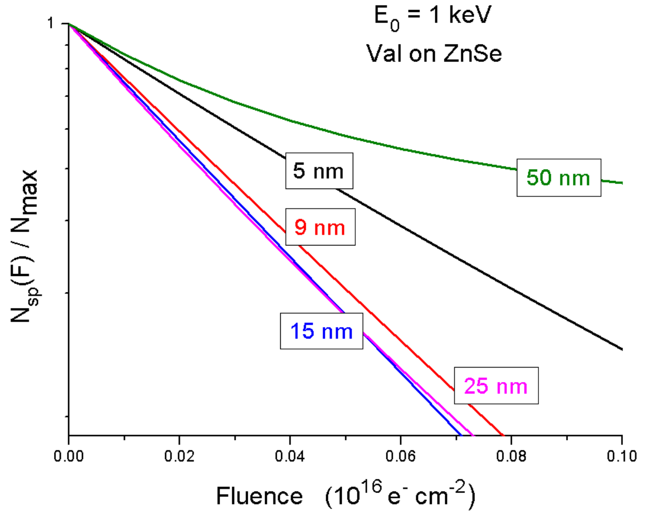

Figure 5.10: Dependence of valine column density on fluence for 5 – 50 nm sample thicknesses. Substrate is 200 nm ZnSe. Increasing the thickness, the average cross section increases, goes into a maximum near 15 nm and then decreases due to the very small $N_{sp}(F)$ decrease rates in deep layers. Excepted for the 50 nm thickness, N_{max} is the same.

5.3

CASINO-extended model applications

5.3.1

Comparison between theoretical predictions and experimental results

The column density evolutions of experimental results are compared to the CASINO-extended model predictions in Figs. 5.11 and 5.12 at the same conditions (beam incidence angle and energy, and sample density and thickness). Figures 5.11 (a) and (b) present the results of 62 nm thick valine samples bombarded by keV electron beams with E_0 = 0.1, 0.50, 0.75 and 1.0 keV. It is noticeable that samples are degraded faster as the energy of the incident beam increases.

One can also observe that, with the exception of 100 eV data, degradations of experimental results are higher than the ones predicted by the model. This finding is supported by the data shown in Fig. 5.12, where E_0 was fixed at 1.0 keV and the samples' thickness was varied. Although CASINO predicts that a 1.0 keV electron beam reaches $z_{max} \approx 47$ nm, the 17, 62 and 210 nm valine samples were completely destroyed at the end of irradiation; evidence that other processes are competing with radiolysis – sputtering, in particular. Roughly estimating, a sputtering yield of ~ 100 molecules ejected per projectile is obtained from data presented in Fig. 5.12.

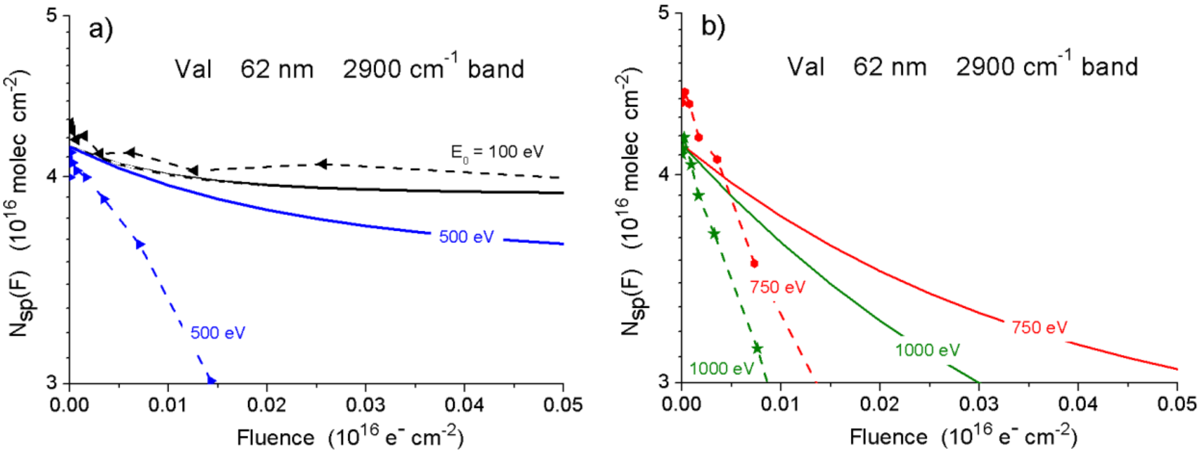

Figure 5.11: Comparison between experimental $N_{sp}(F)$ (points connected by dashed lines) with CASINO-extended model predictions (solid lines) of 62 nm thick valine samples. Data of the 2900 cm^{-1} band for (a) 0.1 and 0.50, and (b) 0.75 and 1.0 keV electron beams.

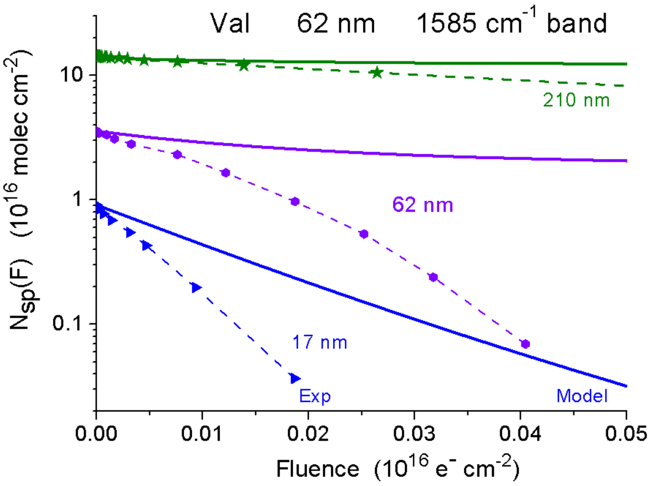

Figure 5.12: Comparison between experimental $N_{sp}(F)$ (points connected by dashed lines) with CASINO-extended model predictions (solid lines) of 1.0 keV electron beams and 1585 cm^{-1} band data for valine samples of 17, 62 and 210 nm.

5.3.2

Astrophysical samples

It is unlikely to find pure prebiotic materials in the surface of astrophysical bodies. Instead, one expects that they are protected by tholins and ices (i.e. H_2O, CO_2 and CO) and mixed with silicates, carbonates and other cosmic materials. CASINO enables multi-material simulations of pure distinct layers and heterogeneous mixtures, as for instance the irradiation of an icy water and valine mix, 100:1, by 2.0 keV electrons, placed between a CO_2 layer and a SiO_2 substrate.

It is possible to generalize Eq. (5.6) and write Eq. (5.14) for heterogeneous samples. For instance, for any prebiotic material (PM) Eq. (5.6) becomes:

$$\sigma_0^{PM} = \frac{E_0^{PM}}{D_0\ N_{max}^{PM}} \tag{5.15}$$

where $E_0^{PM} = E_0\left(\frac{\sum_{i_a}^{i_b} f_i CL_i}{\sum_1^{i_{max}} CL_i}\right)$, the fraction f_i CL_i corresponds to the energy effectively transferred to the PM in the sublayer i; $f_i = S^{PM}/S^{Total}$, where S^{PM} and S^{Total} are the PM and mixture stopping powers, respectively. N_{max}^{PM} is the PM column density.

$$N_{sp}^{PM} = N_{sp}^{PM}(0) - N_{max}^{PM}\left[1 - \left(\frac{1}{i_b - i_a}\right)\sum_{i=i_a}^{i_b} e^{-\sigma_0^{PM}(i_b - i_a)CL_iF}\right] \tag{5.16}$$

i_a and i_b indexes limit the region where the PM begins and ends. Another method to obtain f_i is to run CASINO for the same mixture, but segmenting the PM. For instance, Fig. 5.13 presents the CL_i coefficients of three samples composed by two layers of distinct materials over a SiO_2 substrate perpendicularly bombarded by 2.0 keV electron beam.

The first layer is constituted by 15 nm of CO_2 (ρ = 1.63 g cm^{-3}), the second by 30 nm of pure icy water (0.917 g cm^{-3}) and pure valine (1.32 g cm^{-3}) or by a mix of those substances in the proportion 100:1 (0.92 g cm^{-3}). The simulation reveals that $f_i \approx f = \sum CL_i^{PM} / \sum_1^{i_{max}} CL_i =$ 0.0192 under the i_{max} interval to be applied in Eq. (5.16). In this example, for valine being the PM one obtains: N_{max}^{Val} = 0.88 x 10^{15} molec cm^{-2}, N_{max}^{H2O} = 100 N_{max}^{Val}, Δz^{Val} = 1.3 nm, and Δz^{H2O} = 28.7 nm. Only E_0^{PM} = 46 eV from the 2.0 keV projectile initial energy is drifted to PM, and once it takes 16 eV per molecule to dissociate valine (D_0), on average each projectile degrades ~3 valine molecules.

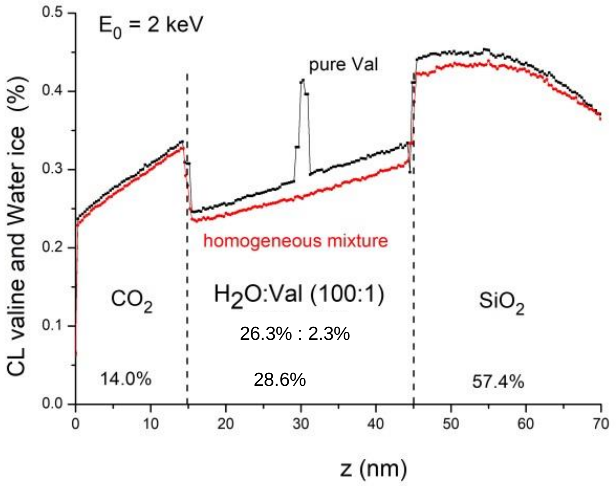

Figure 5.13: CL_i coefficients as a function of depth for 2 keV electron beam for three distinct samples formed by: i) 15 nm CO_2 ice layer; ii) 30 nm H_2O: Val (100:1), either pure H_2O ice + pure valine layers or homogeneously mixed; and iii) SiO2 substrate. The energy delivered to pure valine is 2.3% of E_0. The $CL_i(CO_2)$ and $CL_i(SiO_2)$ change slightly because of the CL_i normalization: the energy transmitted to SiO_2 depends on the Val distribution.

Besides processing Val, the electron beam simultaneously degrades the CO_2 and H_2O compounds, as well as the products that outcome from chemical reactions between Val and H_2O. These processes can be described by equations similar to Eq. (5.16). The shielded Val column density is represented by Fig. 5.14. Partial normalized contributions to de column density are shown; the dotted red line represents their average contribution. Notice that, in contrast to the degradation of thick targets (Figs 5.7 and 5.8a), the degradation of thin samples is uniform and the rear sublayers may be processed faster than the front ones. σ_0 decreases if the CO_2 layer increases: if Δz_{CO2} = 15 nm, $\sigma_0 = 27 \times 10^{-16}$ cm², but if $\Delta z_{CO2} >$ 140 nm the Val degradation ceases.

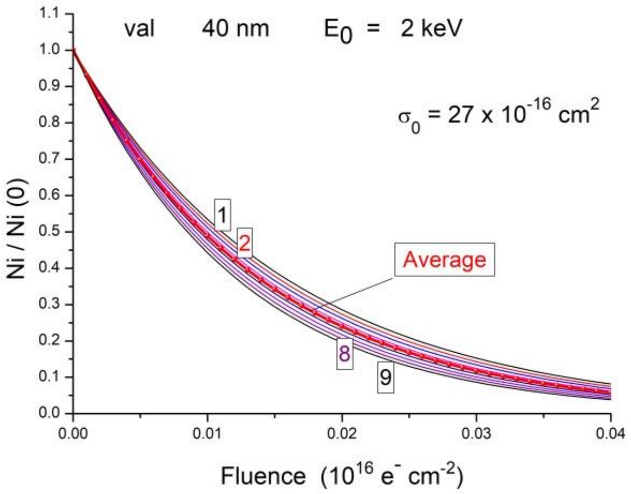

Figure 5.14: Prediction for valine radiolysis by 2 keV electrons. Red curve represents the average degradation of 9 sublayers. This illustrates the material formed by 40 nm H2O:Val (100:1) mixture valine covered by 15 nm CO_2.

In summary, the CL_i coefficients establish that the deposited energy goes with 14.0% in the CO_2 layer, 28.2% in the water-valine mixture and 57.4% in the substrate; furthermore, only 2.3% of the deposited energy goes to the valine degradation, while 26.3% goes to the water molecules, as seen in Fig. 5.13. While the predicted net cross section, σ_0, can be used to estimate half-lives under realistic spatial circumstances, the goal of the present chapter was to demonstrate the CASINO-extended model potentiality and its applications in astrophysical conditions.

6
Discussion

Data presented in chapters 4 and 5 are now discussed.

Regarding sample characteristics, degradation measurements of amino acids as a function of both sample temperature and thickness were performed. This allowed, besides sublimation rate measurements, to determine the dependence of destruction cross section on sample temperature, as well as verifying whether sample thickness effects modify this cross section.

With respect to ion beam data, an extensive work to determine the dependence of amino acid's apparent destruction cross section, σ_d^{ap}, on electronic stopping power, S_e, was carried out. Experiments with multi-charged and molecular beams were also executed; degradation was analyzed for different sample thicknesses, aiming the extraction of sputtering yields.

Concerning degradation by keV electron beams, measurements varying the beam current and energy, as well as the target crystalline structure, temperature and thickness were performed. The lack of a theoretical tool to analyze thick targets degradation by electron projectiles was the motivation to develop the CASINO-extended model.

6.1
Sample characterization

i) Amino acids A-values

In section 4.1.1, experimental results of unprocessed valine and phenylalanine samples were presented and analyzed, permitting the determination of A-values of various bands for non-processed samples. No information was obtained on band strength changes for irradiated samples, that is, $A_v(F)$ is in principle unknown for any fluence different from zero.

In IR spectroscopy, specific cares should be taken for correct results. First, samples cannot be too thick, otherwise IR absorbances saturate and the Beer-Lambert Law, Eq. (4.1), is no longer valid. This does not happen for the present results: saturation occurs at absorbances close or above 5, when peaks start to present flat behaviors at their tops - Figure 6.1 is an example. Second, background and range limits might introduce errors in the analysis of the chosen bands: analysis for all samples should be coherent, keeping the same band limits and background, which may vary with fluence, as shown in Figure 6.2. Although the employed substrates, ZnSe, are practically transparent at the analyzed mid-infrared region, it is important to be careful about its background shape. Furthermore, oil contaminations may exist internally in the chamber windows; externally, in gas phase, CO_2 bands always appear around 2390-2273 cm^{-1} region as a double peak.

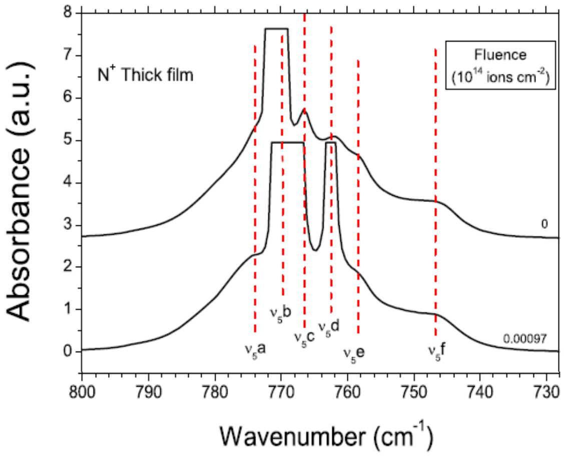

Figure 6.1: Zoom illustrating the saturated 765 cm^{-1} infrared band of an acetylene ice thick film (4 µm), adapted from Pereira et al. (2020) [64].

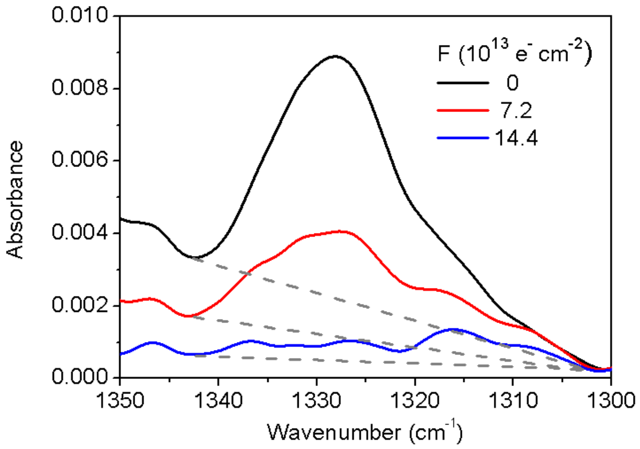

Figure 6.2: Evolution of the 1329 cm^{-1} valine IR band with fluence of 1 keV electrons. Gray dashed lines exhibit how baselines may fluctuate during measurements.

Concerning data from profilometry, the main error source is the lack of a well-defined mask between sample and substrate, which is crucial to determine the correct thickness of the amino acid film. Possible non-uniform deposition may occur, but that does not seem to be the case, since measurements do not present an increasing feature as the probe tip goes towards the center of the sample; this is illustrated in Fig. 6.3, where the green region is flat instead of uphill tilted.

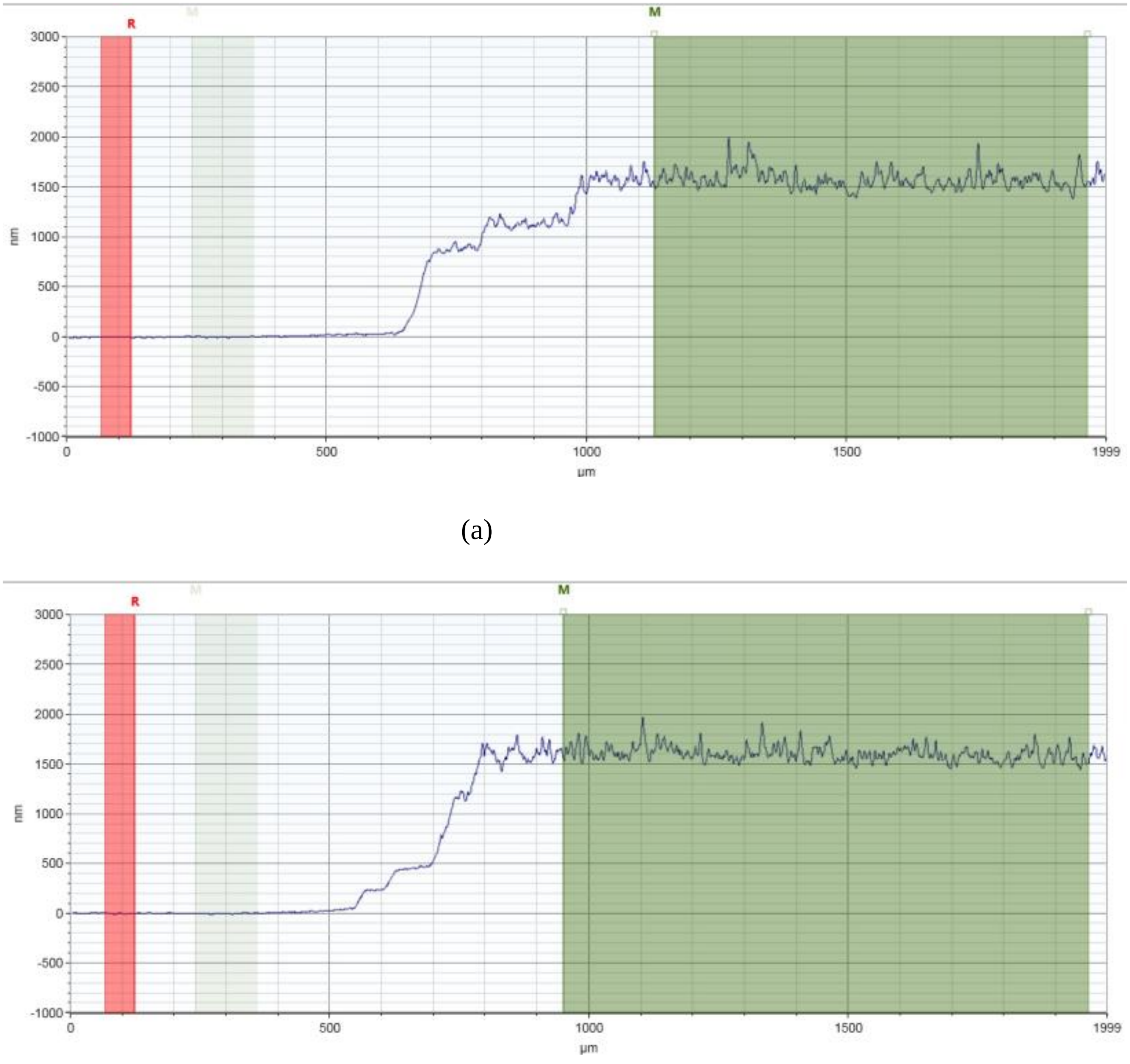

(a)

(b)

Figure 6.3: Thickness profiles of a given valine sample measured at two distinct edges. For both, the average thickness of the deposited material was determined at the green region: (a) 1571 nm, and (b) 1604 nm.

The determination of the A_{vj} for the desired j band is performed by introducing the infrared spectroscopy and profilometry results in Eq. (4.3). The obtained values are presented in tables 4.1 and 4.2 to valine and phenylalanine, respectively. Here, the main problem is that information of samples density is required in Eq. (4.3). For Val and Phe, we adopted the densities 1.32 and 1.29 g/cm³, respectively. It is not excluded the possibility that the deposition method may produce samples with distinct porosities or more compact than the ones referenced, yielding differences in the absolute A_v values; for instance, Gly densities vary up to 50% [65, 66].

ii) *Absorbance dependence on sample temperature*

Temperature affects absorbance on two ways: either sublimation reduces systematically the sample column density and/or A-value changes reversibly with temperature. IR absorption depends on electronic density distribution, which is sensitive to distances between neighboring molecules. Sublimation effects are studied by warming up the sample; reversible absorbance effects are studied by cooling down the sample to cryogenic temperatures and warming it up afterwards.

a) Warming up (sublimation)

For the results shown in section 4.1.2, several samples were prepared simultaneously by vacuum deposition; sample holders, with three substrate disks each, are placed parallel to the sublimation boat and equidistantly placed around it. Sample thicknesses are expected to be equal, but, as seen in section 3.2, the boat may not spread the amino acid vapor in a perfectly isotropic way, and systematic variations in column density occur.

Regarding sublimation data, Fig. 4.8, each sample was kept at a fixed high temperature and IR spectra were acquired after designated time intervals. Figure 6.4 displays the normalized column density, N(t)/N(0), as a function of time, t, that the material spent in the laboratory oven for three samples at T = 90, 100 and 110 °C, respectively. Figures 6.4 (a) and (b) show the results obtained analyzing the 1651-1470 cm^{-1} and 3190-2430 cm^{-1} bands, respectively. The sublimation rate $N_0\beta_T$ for each temperature is extracted by fitting data with the function $\frac{N}{N_0} = 1 - \beta_T t$.

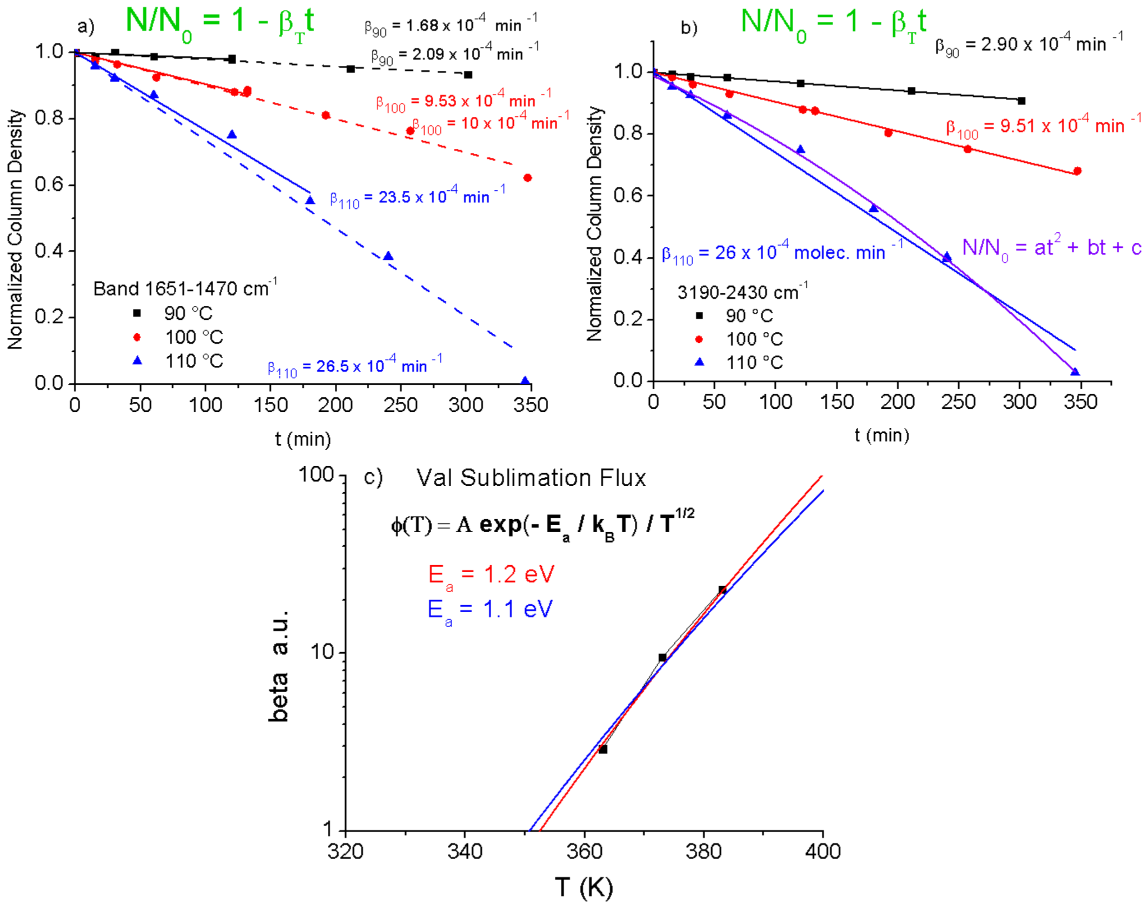

Figure 6.4: L-Val normalized column density as a function of heating time, observed via: (a) the 1641-1470 cm^{-1} band; (b) via the 3190-2430 cm^{-1} band. Solid and dash lines are fittings with the function $\frac{N}{N_0} = 1 - \beta_T t$ in order to determine the sublimation rate $N_0\beta_T$ for each temperature T. c) Sublimation flux of valine; activation energy $E_a = 1.2 \pm 0.1$ eV.

Two kinds of fittings are used: one (solid line) uses data obtained during the first half time of heating; another includes all experimental points. It is noticeable that the slopes increase slightly as the samples get thinner and a better fitting is obtained by a second order function in temperature. Since sublimation rate increases with temperature but decreases with local gas pressure (“pressure cooker effect” [67]), a likely explanation for the observed behavior is: i) for grains in the sample surface at atmospheric pressure, the sublimation rate is relatively high; ii) for grains in the bulk, the sublimated valine molecules diffuses slowly, the local gas pressure raises and the sublimation rate decreases. The thinnest sample heated at 110 °C is the best case for observing this characteristic; actually, it is the only one completely sublimated during the experiment time. Results presented in Fig. 6.4 (b) repeat and confirm the sublimation behavior but measuring the 3190-2430 cm^{-1} band absorbance. On the sample heated at 110 °C, a parabola fitting was also performed (purple curve at Fig. 6.4 (b)), confirming that the sublimation rate increases as the sample gets thinner. Table 6.1 summarizes the results and presents an average value for the sublimation rate β for each temperature.

Table 6.1: Heating temperatures; sublimation constant β_T for two selected bands and their respective average. For 1641-1470 cm^{-1} band, two time intervals have been considered. Column density of samples before thermal processing, N_0. Sublimation rate $N_0\beta_T$.

T (°C)	**β_T** (10^{-4} min^{-1})				**N_0** (10^{17} molec cm^{-2})	**$N_0\beta_T$** (10^{13} molec min^{-1} cm^{-2})
	Band 1651-1470 cm^{-1}		**Band 3190-2430 cm^{-1}**	**Average**		
90	1.7	2.1	2.9	2.2 ± 0.7	1.60	3.52 ± 1.1
100	9.5	10	9.5	9.7 ± 0.5	1.65	16 ± 0.8
110	23	26	26	25 ± 2	1.26	3.15 ± 2.5

As seen in Fig. 6.4 and Table 6.1, samples: i) sublimate faster as the heating temperature increases and ii) become thinner with time. When T increases, the kinetic energy RT increases and gets closer, or even overcomes, the activation energy E_a, increasing the chemical sublimation rate $\Phi(T) = A \exp(-E_a/RT)/T^{1/2}$ [41]. Error sources are the determination of the integrated absorbances (peak areas) and the average temperature of the sample when it was placed in the oven. In fact, after introducing the samples in the oven, ~3 min are necessary for them to reach the equilibrium temperature.

Due to the long measurements in high vacuum at room temperature, a relevant question is whether valine sublimates under these conditions. Previous works report that at low pressure valine does not sublimate (or has a negligible sublimation rate) [42, 56].

b) Cooling down (IR spectral changes)

As shown in section 4.1.3, IR absorption data from L-Val present a characteristic behavior as the sample temperature changes; peaks become more resolved as the temperature decreases. Figure 6.5 shows the evolution of valine’s

IR spectra when the temperature changes, back and forth over two cycles, from room temperature (RT) to 40 K. It is observed that, at low temperatures: i) spectra become more resolved (broad peaks turn into narrower ones) and ii) some bands shift to higher wavenumbers (blue shift, see Figs. 4.10 (d) and (e)). After warming up back to 300 K, spectrum shapes are restored, which means that no irreversible physical phase transition has occurred. For the 2nd cycle, the sample was thermally processed (annealed at 120 °C for 1 hour) and cooled down to 40 K again. Because of circumstantial reasons, this new cycle lasted longer, which is the reason why a broad water absorbance feature appears at 40 K in the spectrum of the annealed sample (wavenumbers > 3000 cm^{-1}).

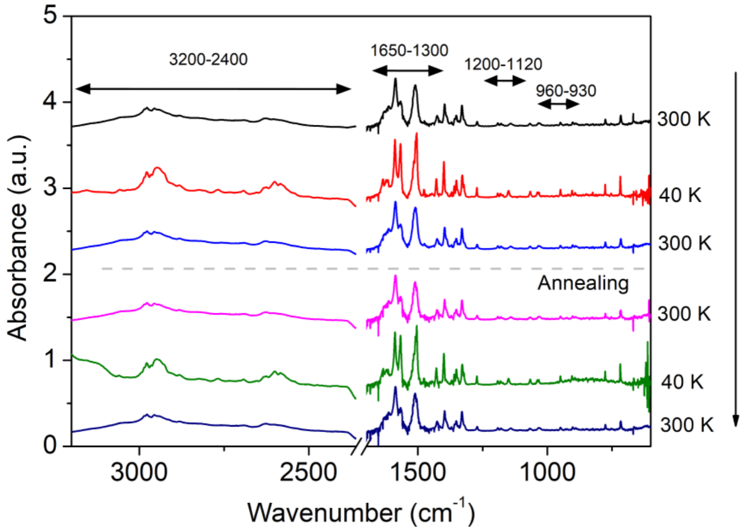

Figure 6.5: Infrared spectra in function of valine temperature before and after annealing processing.

Figures 6.6 (a) – (d) display how the integrated absorbance of the 3000-2400, 1280-1260, 1165-1120, and 960-930 cm^{-1} bands evolve in function of temperature. Solid and dashed lines represent non- and annealed samples, respectively. Arrows indicate the time flow (temperature beginning and ending at 300 K). These are non-irradiated samples.

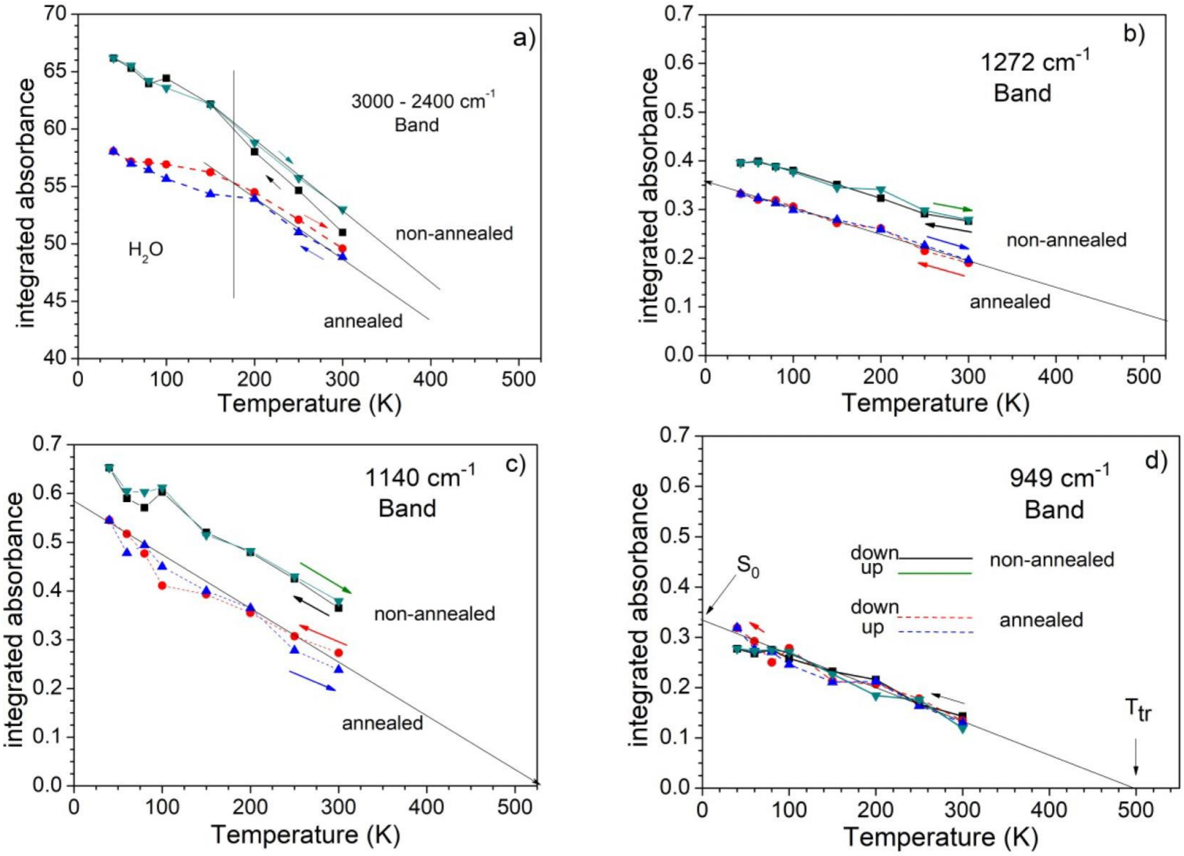

Figure 6.6: Integrated absorbance dependence on sample temperature for bands: (a) 3000-2400, (b) 1272, (c) 1140, and (d) 949 cm^{-1}; solid lines represent the first excursion (temperatures decreasing from 300 K to 40 K and then going back to 300 K). After annealing the sample, the same procedure was repeated (dash lines) [56].

The integrated absorbances clearly increase with the decrease of sample temperature (Fig. 6.6); since the number of molecules in the sample does not increase, the A-values of the distinct bands must increase with temperature. The Beer-Lambert Law can be written in function of sample temperature as N(T) = ln(10) S(T)/A_v(T). Since N(300 K) = N(T), because without sublimation temperature variation does not alter the number of molecules in the sample, the relationship S(300 K)/S(T) = A_v(300 K)/A_v(T) holds. From A-value results on section 4.1.1.1 and low temperature data on section 4.3.4, the A-value dependence on temperature of the 1408-1380 cm^{-1} band, above 150 K, is:

$$A_v(T) = 1.10 \times 10^{-17}\ S(300\ K)/S(T)\ \text{cm molecule}^{-1} \quad \text{(see Fig. 6.7).}$$

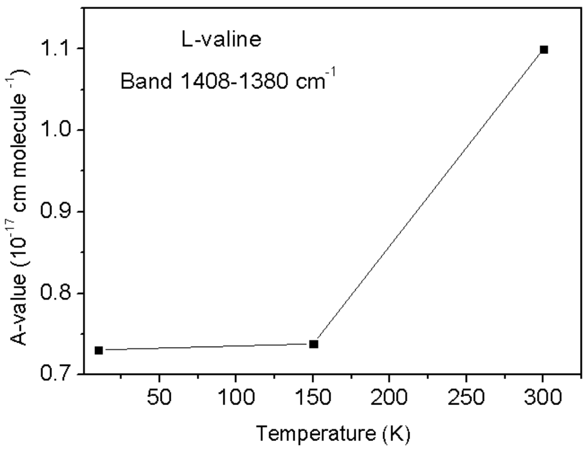

Figure 6.7: A-value of the 1408-1380 cm^{-1} band as a function of valine temperature.

The linear function $S = S_0\,(1 - T/T_{tr}) \equiv S_0 - \alpha\,\Delta\nu\,T$ was employed in the fitting of data presented in Figure 6.6. In this relationship, S is the integrated absorbance, S_0 the integrated absorbance at zero Kelvin, T the absolute temperature, T_{tr} the "transparency" temperature when a given band absorbance voids, α the absorbance rate coefficient ($\alpha = S_0/(\Delta\nu T_{tr})$), and Δν the band interval ($\Delta\nu = \nu 1 - \nu 2$). T_{tr} is just a fitting parameter: the sample should be in gas phase at these temperatures. Fitting parameters are shown in table 6.2. One notices that the parallelism seen in figure 6.6 is evidenced by the *same* absorbance rate coefficient ($\alpha \approx 0.25$) not only between themselves (non- and annealed samples), but also between the three single bands analyzed.

Table 6.2: Fitting parameters of absorbance evolution with temperature, Fig. 6.6, with equation $S = S_0\,(1 - T/T_{tr}) = S_0 - \alpha\,\Delta\nu\,T$ [56].

Band (cm^{-1})		3000 – 2400		1272		1140		949	
$\Delta\nu = \nu_1 - \nu_2$		3000 – 2400		1280 – 1260		1165 – 1120		960 – 935	
Annealing:		non-ann.	ann.	non-ann.	ann.	non-ann.	ann.	non-ann.	ann.
S_0	cooling	73	63	0.43	0.36	0.68	0.56	0.31	0.33
	warming	71	65	0.42	0.36	0.69	0.58	0.32	0.33
T_{tr} (K)	cooling	1000	1200	833	667	667	555	588	500
	warming	1100	1200	909	714	714	526	500	500
α (10^{-4} cm^{-1} K^{-1})	cooling	1.2	0.87	0.25	0.27	0.22	0.22	0.21	0.26
	warming	1.1	0.90	0.24	0.26	0.22	0.24	0.25	0.26

Figures 6.8 (a) – (c) show the behavior of the full width at half maximum (FWHM) of the 1280-1260, 1165-1120, and 960-930 cm^{-1} single bands, as the sample temperature changes. Here again, solid and dashed lines represent non- and annealed samples, respectively. FWHM decreases as the temperature decreases up to level off into a minimum width, which depends on crystallographic properties of the sample and, mainly, on fundamental quantum mechanics constrains. Indeed, even for a pure monocrystal at zero Kelvin, Band Theory predicts that band broadness is ruled by the height and width of potential barriers, which, in turn, depend on interatomic or intermolecular distances [68].

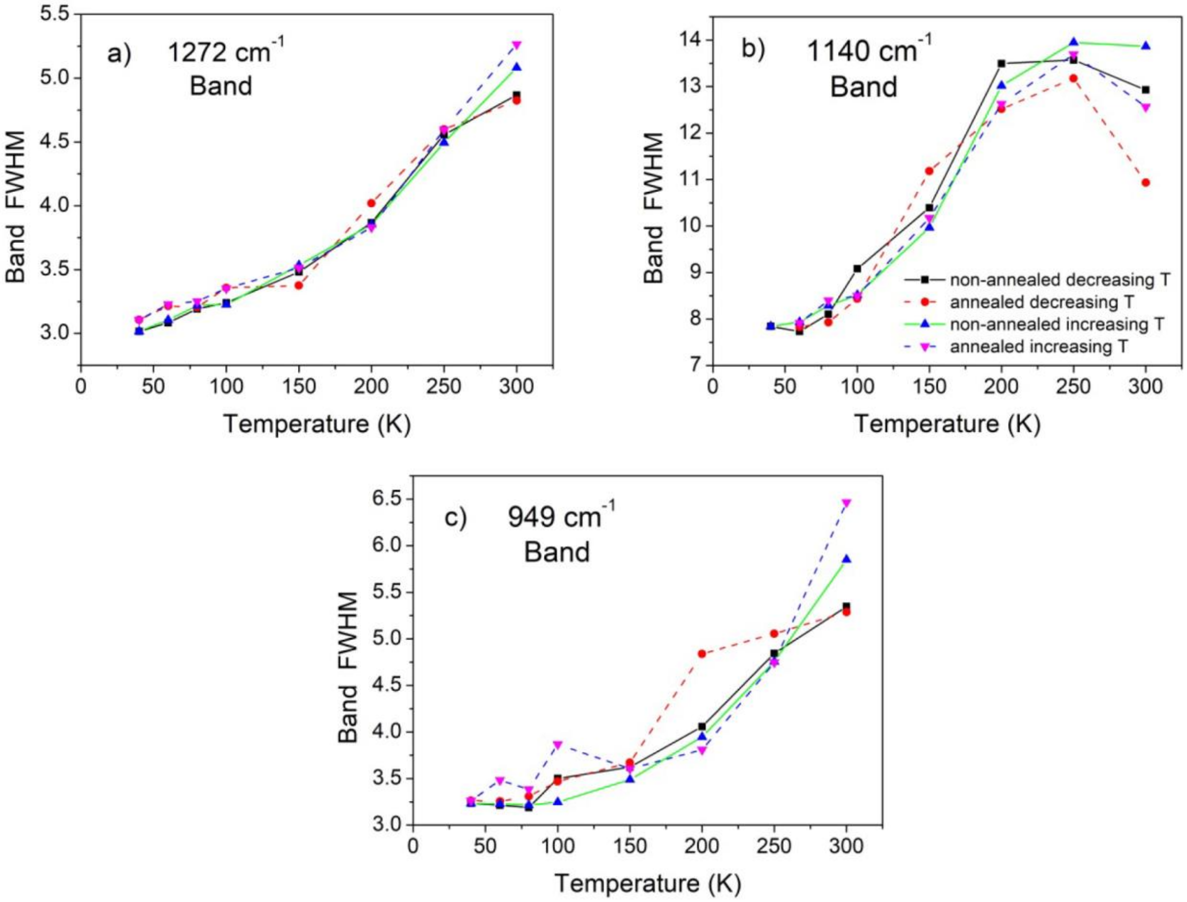

Figure 6.8: Full width at half maximum dependence on sample temperature for the single bands: (a) 1272, (b) 1140 and (c) 949 cm^{-1}; solid and dash lines represent the excursions before and after sample annealing, respectively.

Concerning the current analysis, questions to be answered are: when the sample temperature decreases, why bands become narrower? Why infrared absorbances increase? And why some bands shift?

When temperature is lowered, two thermal effects occur: i) molecular velocities decrease and ii) mean molecular and atomic distances are reduced. In detail:

i) Concerning the first question: the MID-infrared region corresponds to photons of 60 – 500 meV (since $E = h\nu = k\hbar c$; with k being the wavenumber). Average bandwidths are ~ 30 cm^{-1} or ~ 4 meV. If the sample temperature varies from 40 to 300 K, the average molecular kinetic energy, kT, varies from 3.4 to 26 meV. The fact that bandwidths and thermal energies have similar values gives a hint that thermal energies should be responsible for a significant fraction of the observed bandwidths. Indeed, photon absorption by a molecule is a resonant process (similar to the Mössbauer effect for atomic nuclei) and the energy match depends on the molecule’s velocities; in turn, the molecular velocity distribution varies with temperature. The consequence is that energy match is less strict for absorption at high temperatures (Doppler effect).

ii) Band absorbances increase at lower temperatures because molecular polarizability is higher. Infrared absorbance depends on dipolar moment, which in turn depends on sample temperature. Temperature decrease reduces intermolecular distances, and increases polarizability. In particular, apolar molecules free to rotate have negligible time-average polarizability; their polarizability at low temperature samples increases due to constraints on molecular rotation. In adition, bandwidth is related to molecular relaxation: the lower is the damping, the thinner is the bandwidth. Moreover, the damping depends on the vibrational energy flow from the molecule towards the solid.

Band shifts may be consequence of conformer transitions and have been reported for glycine and alanine, at different temperatures. Conformers are characterized by the different stable or metastable configurations that a molecule may present. Gomez-Zavaglia and Fausto (2003) [69] studied the deprotonation phenomenon of the glycine carboxylate group (that is, the protonation of the amino group). They proposed that, during the deposition (or condensation), the glycine kinetic energy in gas phase would be employed to transform, irreversibly, neutral molecules into zwitterion isomers. In this process, sample temperature increases and the extra energy converts the deposited molecules into zwitterions. Rodríguez-Lazcano et al. (2012) [70] performed similar experiments with alanine, and basically reached the same conclusions. Alanine molecules: i) in the gas phase are neutral but, forming a solid at room temperature, are zwitterionic; ii) when deposited at 25 K, the solid is constituted by a mix of neutral and zwitterionic forms, the neutral isomers becoming zwitterions as the sample is heated.

In the interpretation of amino acids spectra, composed by lines due to distinct conformers, UV irradiation and annealing are procedures that may be used to change the molecular conformational ratios. Wong et al. (2015) [71] analyzed, experimental- and theoretically, several isolated β-alanine in a parahydrogen matrix; they have confirmed that conformer transitions occurred when the material was exposed to UV radiation. Assuming that valine behaves as alanine and glycine, the sample produced by deposition at 300 K and which data are shown in Figs. 6.5 – 6.8 should be constituted exclusively by zwitterionic molecules.

Tamuliene et al. (2018) [72] have studied gaseous valine fragmentation by low energy electrons (0 – 150 eV) and by DFT calculations; they determined the total energies for four valine conformers, neutral or ionized. Temperature variation (from 40 to 400 K) did not modify the valine isomeric structure, confirming that no permanent phase transitions occur during the thermal treatment. The observed band shifts (Figs. 4.10 (d) and (e)) are therefore attributed to conformer transitions induced by temperature changes.

6.2
Ion beams

The present section aims to discuss the results presented in section 4.2 relative to the valine, phenylalanine and glycine degradation by MeV ion beams.

Valine is the most probed amino acid in the current work, and because of this it will be used to illustrate the discussion of the analytical method. Fig. 6.9 (a) shows three selected spectral regions of a valine sample bombarded by a 230 MeV S^{+15} beam at a given fluence; Fig. 6.9 (b) presents the fluence evolution of their integrated absorbance. At high fluences, they decrease exponentially and absorbances are proportional among themselves. Such behavior is not seen at low fluences, when restructuring phenomena such as compaction might have a powerful effect on massive regions; this is indeed the case for spectral regions II and III (Beer-Lambert Law: higher the absorbance, higher the number of molecules). On the other hand, at the beginning of irradiation, region I behaves differently from regions II and III. Actually, there is no evidence of compaction in region I. Absorbances with similar trend in distinct spectral regions mean that any chosen region should give the same evolution behavior, as long as one is coherent with the band wavenumber limits and with the background line. In other words, information - such as the destruction cross section - can be extracted from any fraction of the absorption band, although one should be careful when analyzing regions with daughter species and/or contaminations, as well as distinct compaction regions.

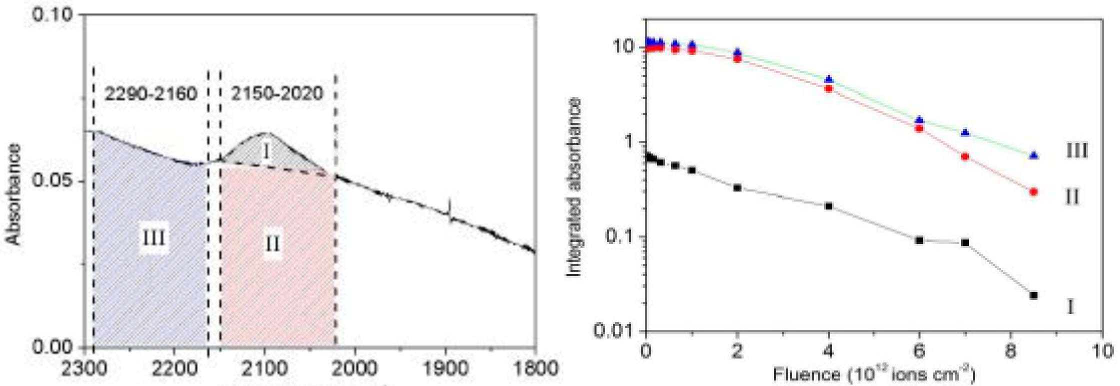

(a) (b)

Figure 6.9: (a) Zoom of valine infrared spectrum at the region 2300-1800 cm^{-1}, acquired at an arbitrary fluence. Regions I and II correspond to the 2109 cm^{-1} band and to its background, respectively; region III corresponds to the background line of the 2290-2160 cm^{-1} wavenumber interval. (b) The integrated absorbance (in cm^{-1}) evolution with fluence of the 230 MeV S^{+15} beam for these three regions [61].

Note that, at high fluences, some bands disappear while others do not. In Fig. 6.10, the absorbance relative to region 1340-1310 cm^{-1} vanishes, evidence that the sample was completely destroyed, but the one relative to region 3200-2400 cm^{-1} does not: some irradiation residual material (daughter species or products) vibrates in the frequencies very close to those of the precursor molecules. Due to their band widths larger than the precursor-product frequency variations, a spectrometer with higher resolution is not a solution. So, in order to compare cross sections obtained from both regions, one should subtract the contribution of the daughter species from the measured band absorbance. It turns out that distinct bands generate cross section values close to each other, but systematically different: an average is then carried out. A detailed discussion follows.

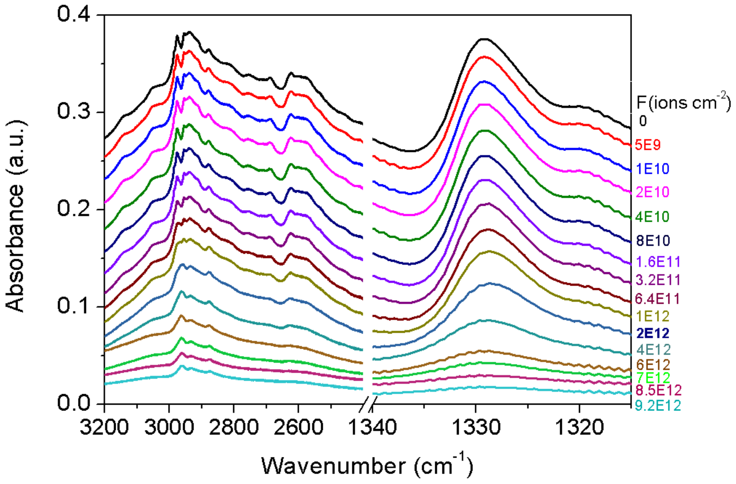

Figure 6.10: 3200-2400 and 1340-1315 cm^{-1} spectral evolution of a valine sample bombarded by a 230 MeV S^{+15} beam; beam fluence increases from top to bottom.

Data are usually fitted with Eq. (6.1). S(F) and S_0 are the integrated absorbances at fluences F and zero, respectively. σ_d^{ap} is the apparent destruction cross section (which includes radiolysis and sputtering effects), and S_∞ the integrated absorbance of saturation (or base line). S_∞ is band dependent, and it may indicate the presence of: i) daughter species vibrating at frequencies close to precursor ones or ii) external contaminants such as gaseous/adsorbed water or CO_2; if none of these two possibilities is the case, the band vanishes completely, that is, $S_\infty = 0$. Figure 6.11 displays the absorbance evolution for three valine bands to exemplify the S_∞ possibilities. Since Fig. 6.11 is presented in semi-log scale, the last experimental points of the vanishing band do not appear in the graph.

$$S(F) = S_0 e^{-\sigma_d^{ap} F} + S_\infty \tag{6.1}$$

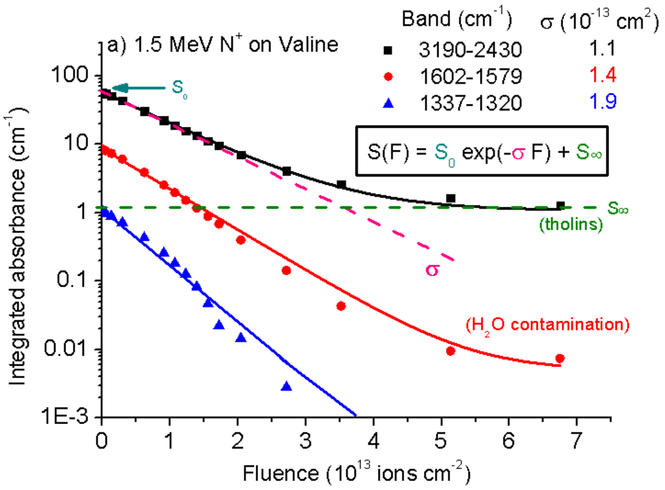

Figure 6.11: Dependence on fluence of three valine band integrated absorbances. Sample was irradiated by a 1.5 MeV N^+ beam. Solid lines are fittings with Eq. (6.1); S_∞ = 1.1, 0.005 and 0 cm^{-1} for the bands with tholins, water contamination and with pure precursors, respectively.

Analyses are usually performed for several bands, because distinct peaks decay at slightly different rates, as illustrated by the three band evolutions presented in Fig. 6.11. This happens not only for spectral regions with growing daughter species absorbances, but also for single bands (the ones produced only by precursors, for which absorbances void at high fluences). The consequence of having distinct evolutions is an evidence that the A-values are fluence dependent, justifying the notation $A_v(F)$. Table 6.3 confirms that the A-value ratios $A_{v,j}(F)/A_{v,\,948}(F)$ are not constant compared to data at zero fluence or at a reference fluence value, F_{ref}. Here, $A_{v,j}(F)$ is the A-value of the j band at fluence F and $A_{v,\,948}(F)$ is the A-value of the reference band 948 cm^{-1} at the same fluence; each beam has a different F_{ref}, see the fourth line of the table. Since, at any fluence, the column density of a given sample is unique and well defined, the integrated absorbances of the j and reference bands must be related by the Beer-Lambert Law: $S_j(F)/S_{948}(F) = A_{v,j}(F)/A_{v,\,948}(F)$.

Table 6.3: Relative A-values of five bands for virgin (F = 0) and processed (F_{ref}) valine samples. Band 948 cm^{-1} is taken as reference for $A_{v\text{-ref}}$. The reference fluence F_{ref} is different for each beam or sample.

	Ion beam	**$A_v/A_{v\text{-ref}}$**			
		H^+ 1.5 MeV	**He^+ 1.5 MeV**	**N^+ 1.5 MeV**	**S^{15+} 230 MeV**
	Sample thickness	**2.4 µm**	**0.96 µm**	**0.23 µm**	**0.58 µm**
Band (cm^{-1}) (interval)	**F_{ref} (ions cm^{-2})**	**5.8 x 10^{14}**	**1.1 x 10^{13}**	**4.4 x 10^{12}**	**3.2 x 10^{11}**
2900 (3300-2400)	0	273	282	235	246
	F_{ref}	768	602	270	303
1329 (1335-1301)	0	3.94	3.07	9.51	10.8
	F_{ref}	5.23	6.34	10.5	13.8
1271 (1279-1261)	0	0.876	1.16	0.981	0.984
	F_{ref}	0.955	1.70	0.997	1.22
948 (957-937)	reference	1	1	1	1
	reference	1	1	1	1
716 (726-705)	0	2.80	2.70	2.35	3.39
	F_{ref}	5.05	3.31	2.54	3.85

Stopping power dependence

Figure 6.12 (a) shows, for the band 948 cm^{-1}, how the normalized integrated absorbance evolves with fluence for four ion beams. They all decay exponentially, and it is clear that the higher the stopping power, S_e, the faster is the sample destruction (i.e., N(F) decay is steeper). Taking away the electronic stopping power and the specific mass (density) dependences, Fig. 6.12 (b) displays the same results as a function of the absorbed dose instead of the beam fluence. The definition $D \equiv S_e F/\rho$ is used, where D is the beam dose (eV g^{-1}), F the fluence (projectiles cm^{-2}), ρ the valine density (g cm^{-3}) and S_e the electronic stopping power (keV $\mu m^{-1} = 10^7$ eV cm^{-1}). Strictly speaking, radiation dose is the absorbed ionizing energy per mass unit, expressed in Gy ≡ 1 J kg^{-1} = 6.242 x 10^{15} eV g^{-1}, a unit used for macroscopic energies and masses. Here, the concept of "molecular dose" D is more convenient, which is the energy absorbed per molecule mass, m_{molec}, so that E/m_{molec} can also be expressed in eV/molec. Conversion is made by taking m_{molec} (g) = M/N_A= M/6.022 x 10^{23}, where M is the molar mass in g mol^{-1}; that is:

$$1 \text{ Gy} = 1 \text{ J/kg} = 6.242\text{x}10^{18} \text{ eV}/[10^3 \text{ N}_A/\text{M}] = (1.037\text{x}10^{-8} \text{ M}) \text{ eV molec}^{-1}.$$

Of course, the above considerations are valid for a given homogenous material or, in this context, for a non-irradiated amino acid. Once irradiation starts, the amino acid degrades and its concentration decreases. If the beam current is constant, the deposited energy rate in the sample is also constant, but the energy rate transferred to precursors decreases. Whenever the fluence attains the value $F_0 \equiv 1/\ \sigma_d^{ap}$, the precursor normalized column density, $N(F)/N_0 = \exp(-\sigma_d^{ap} F)$ becomes $N(F_0)/N_0 = \exp(-1) \cong 0.368$; that is, 63.2% of the original material has been destroyed or ejected. The "apparent" deposited dose up to this point to the material is defined as $D_0^{ap} = S_e F_0/\rho = S_e/(\rho\ \sigma_d^{ap})$, quantity that can be extracted directly from fittings of the integrated absorbance analysis. D_0 is the dose effectively deposited in the bulk and consumed only for radiolysis; since $\sigma_d^{ap} > \sigma_d$, $D_0^{ap} < D_0$, interpreted as the same projectile energy transferred to a higher precursor mass correspondent to dissociated and ejected molecules.

Figures 6.13 (a) and (b) present the normalized integrated absorbance evolution with dose for glycine and phenylalanine, respectively.

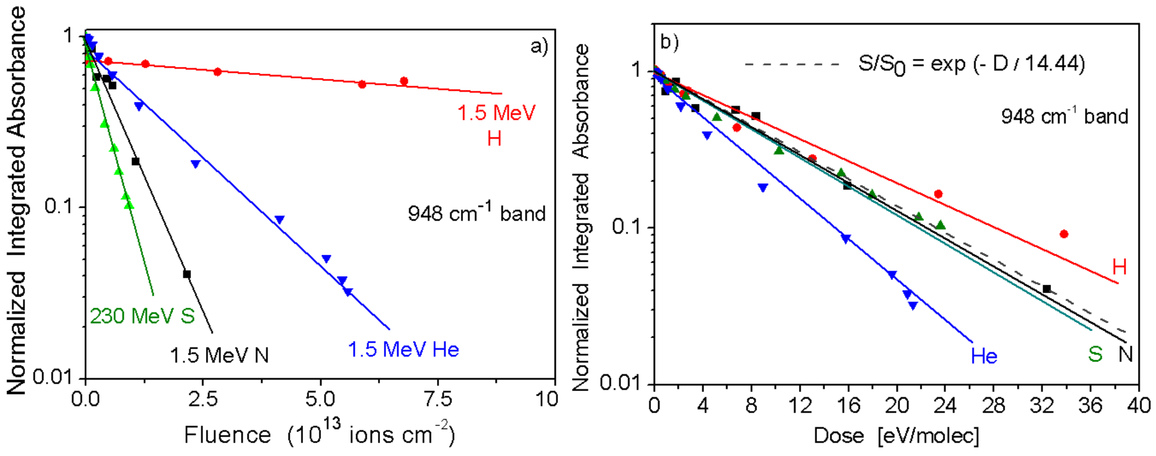

Figure 6.12: S(F)/S(0) for valine irradiated with four different beams, as a function of their respective (a) fluence and (b) dose. Conversion: 1 eV molec^{-1} = 96.5 M^{-1} MGy, where M is the molar mass (in g/mol).

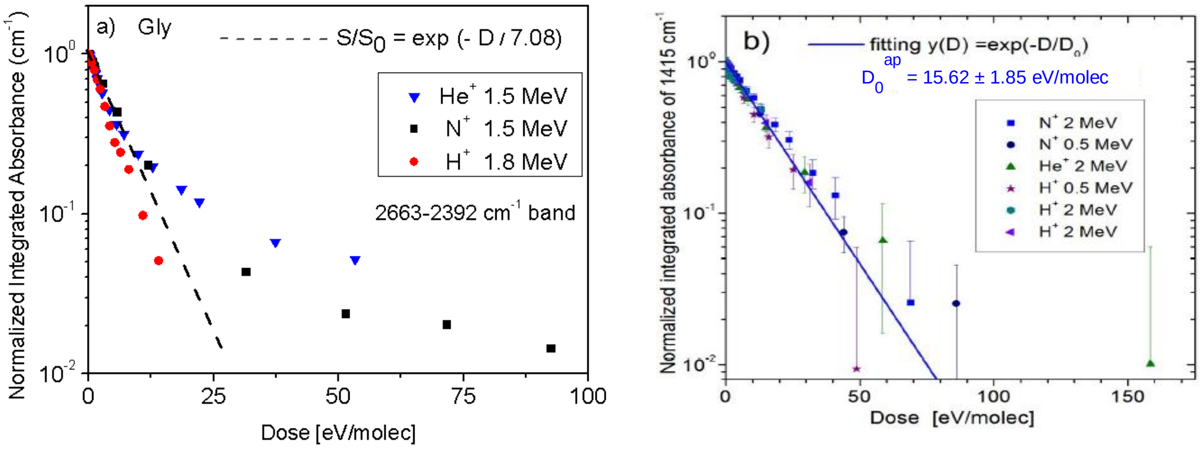

Figure 6.13: S(D)/S(0) as a function of dose for a) glycine and b) phenylalanine.

When data are exhibited as in Figs. 6.12 (b), 6.13 (a) and (b), the span in the precursor's absorbance decay corresponding to irradiation by distinct ion beams is reduced and data fluctuate around an average exponential–decay. It is then possible to estimate the critical "macroscopic" dose $D_0^{ap} = S_e/(\rho\ \sigma_d^{ap})$ in gray or in keV g^{-1}, or the critical "microscopic" dose, if expressed in eV molecule^{-1} unit.

Table 6.4 presents the electronic and nuclear stopping powers (S_e and S_n, respectively) of the ion beams specified in section 4.2. Since $S_n << S_e$ in the energy range of interest, data in Figs. 6.14 (a) – (c) are useful to extract the average apparent destruction cross section dependence, σ_d^{ap}, with S_e, for the amino acids glycine, valine and phenylalanine, respectively.

Table 6.4: Electronic (S_e) and nuclear (S_n) stopping powers of selected ion beams on the amino acids glycine, valine and phenylalanine (SRIM [73]).

Amino acid	**Ion Beam**	**Energy (MeV)**	**S_e (keV μm^{-1})**	**S_n (keV μm^{-1})**
Glycine	H^+	1.8	27	0.018
	He^+	1.5	287	0.29
	N^+	1.5	1070	8.85
Valine	H^+	1.5	26.7	0.019
	He^+	1.5	252	0.26
	N^+	1.5	998	7.84
	S^{15+}	230	1690	1.03
Phenylalanine	H^+	2.0	20.4	0.013
	H^+	0.5	50.4	0.044
	He^+	2.0	204	0.18
	N^+	0.5	544	1.69
	N^+	2.0	1082	5.69

Figs. 6.14 (a) – (c) display the observed dependence of the apparent destruction cross section on the electronic stopping power for glycine, valine and phenylalanine, respectively. Free fittings with $\sigma_d^{ap} = a\, S_e^n$ yields n = 0.91 ± 0.03, 0.97 ± 0.11, and 0.94 ± 0.02 for Gly, Val and Phe, respectively. For data presented in Fig. 6.14, we have adopted n = 1.0 ± 10%. The linear dependence $\sigma_d^{ap} = a\, S_e$ is reasonable, or at least acceptable, for the three analyzed amino acids.

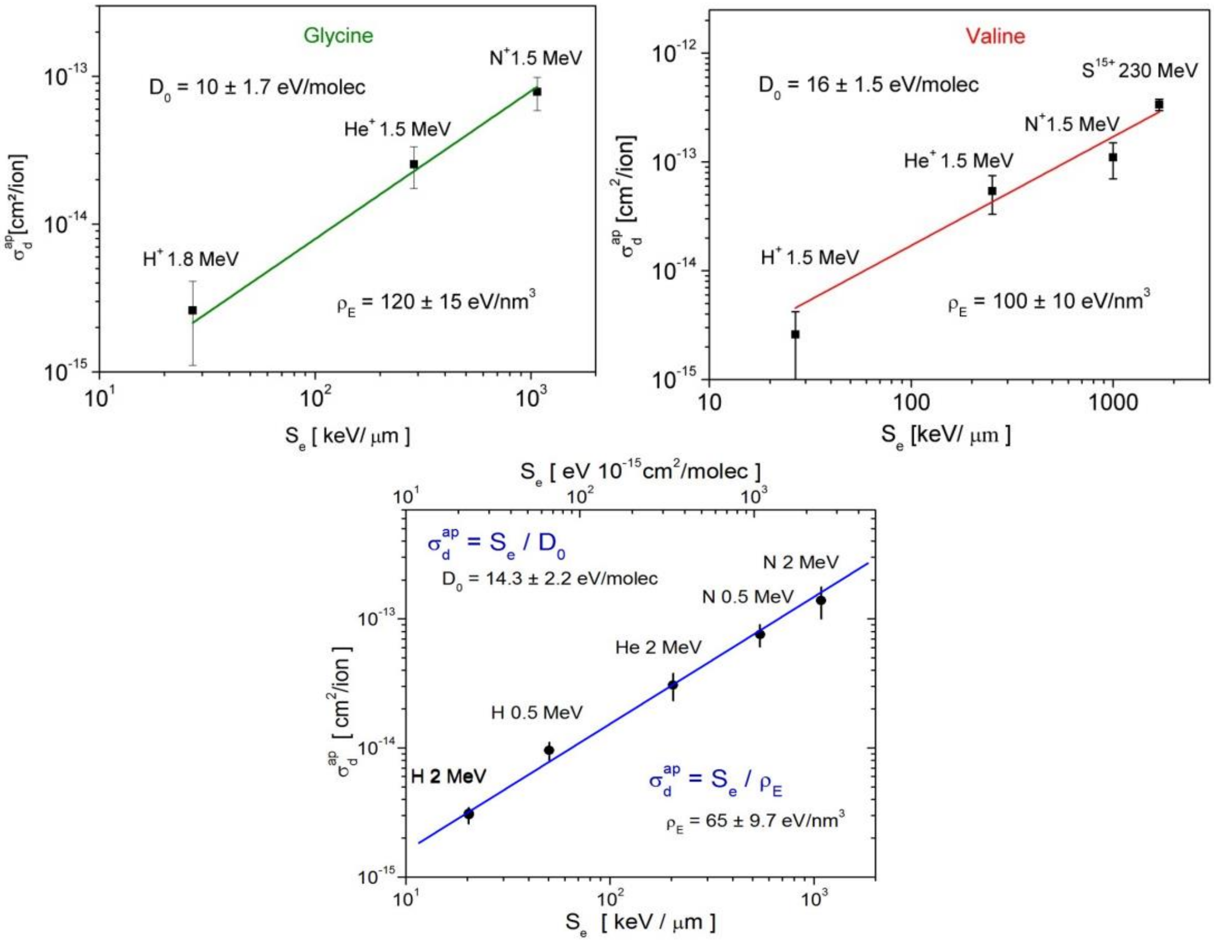

Figure 6.14: Apparent destruction cross section dependence on electronic stopping power for (a) glycine, (b) valine and (c) phenylalanine. The straight line represents a power law $y = a\, x^n$, where n =1. For each amino acid, the respective ρ_E and D_0 values are extracted directly from the linear fittings with equation $\sigma_d^{ap} = S_e/\rho_E$.

$$\sigma_d^{ap} = a\, S_e \qquad \text{or} \qquad S_e = \frac{1}{a}\sigma_d^{ap} = \rho_E\, \sigma_d^{ap} \tag{6.2}$$

The parameter *a* is distinct for each amino acid and has unit of volume per energy; its inverse can be interpreted as the average deposited energy density necessary to dissociate/eject precursor molecules: 1/*a* ≡ ρ_E which, in turn, is proportional to the chemical G-value for dissociation of molecules. The molecular volume being $V_m = (M / N_A)/\rho$, the average energy to dissociate e^{-1} of the molecular population is $\rho_E V_m = \rho_E M/(\rho N_A)$, which should be recognized as the critical dose D_0^{ap}; Table 6.5 gives the related quantities for the examined amino acids.

Table 6.5: Analyzed amino acids and their respective molecular weight (M), density (ρ), molecular volume (V_m), and minimal doses (D_0^{ap} in eV molec^{-1} and in MGy) and deposited energy density (ρ_E) for dissociation.

Amino acid	**M*** **(g mol^{-1})**	**ρ^*** **(g cm^{-3})**	**V_m** **(nm^3)**	**D_0^{ap}** **(eV molec^{-1})**	**D_0^{ap}** **(MGy)**	**ρ_E** **(eV nm^{-3})**
Glycine[a]	75.06	1.61	0.078	10 ± 4.5	13 ± 5.8	120
Valine[b]	117.14	1.32	0.16	16 ± 2.0	13 ± 1.6	100
Phenylalanine[c]	165.18	1.29	0.21	14.3 ± 2.2	8.3 ± 1.3	65

[a]da Costa et al. (2021) [63]; [b]da Costa et al. (2020) [61]; [c]Mejía et al. (2021) [51]; [*]Chusuei & Goodman (2003) [74].

Results on Table 6.5 show that $\rho_{E,Phe} < \rho_{E,Val} < \rho_{E,Gly}$, which indicates that, among these three amino acids, glycine is the most resistant material when exposed to ionizing radiation. One may interpret such finding by pointing out that phenylalanine and valine are more fragile than glycine because they are larger molecules, and thereby with larger destruction cross sections. However, it is important to take into account other factors, in particular the molecular stability; the irradiation of large molecules such as Polycyclic Aromatic Hydrocarbons, PAHs, by MeV H^+ and He^+ beams presents relatively low destruction rates [6]. The argument that a molecule with many identical functional groups (e.g., multiple aromatic rings) keeps absorbing radiation in a given vibrational band, even when a similar functional group is broken, is not convincing: the same argument could be invoked for identical functional groups existing in different molecules in the sample and this goes against Beer-Lambert Law.

It is noticeable that the order of magnitude of doses D_0 found is about 10 MGy, much higher than lethal or radiotherapy doses (10 – 100 Gy). This difference is attributed to the fact that ∼10 Gy irradiation destroys intermolecular bonds and very small fractions of DNA material, which is enough to stop or disturb its biological functions; in contrast, the D_0 determined by the current method corresponds to the energy necessary to destroy ~ 63% of precursor molecules.

Multi-charged beams

Sputtering and radiolysis are sensitive to projectile charge; yields of both processes are expected to be proportional to $S_e^n \sim (q^2)^n$. For icy samples, n = 2 have been reported for sputtering (e.g. Seperuelo-Duarte et al. (2010) [75]) and n = 1 to 1.5 for radiolysis. As mentioned in Chapter 4, experiments with multi-charged beams were planned to verify the sensitivity of amino acid's damage to the projectile charge. The project involves experimental challenges such as production, selection, transport and monitoring of multi-charged beams. Results must be regard as preliminary, providing discussion for technical improvements.

1.5 MeV N^+ ions were produced by the Van de Graaff accelerator and selected by the 90° analyzing magnet. The residual gas inside the 4.9 m long canalization between this magnet and the switching one was raised to around 10^{-4} mbar for enhancing ion beam charge exchange. At 1.5 MeV energy, projectiles have v = 4.5 x 10^3 km/s, and the equilibrium charge state distribution is N^{3+} (48%), N^{2+} (27%), N^{4+} (19%), N^{1+} (4%) and N^{5+} (2%) [76]. The average equilibrium charge state is, therefore, $q_{eq} = 2.9$; CasP (Convolution approximation for swift Particles) prediction is 2.1 [77].

After, crossing a 10^{-6} mbar residual gas, the N^+, N^{2+} and N^{3+} charge state beams were selected by an adequate magnetic field at the switching magnet and transported via a ∼5 m canalization up to the UHV section (at <10^{-7} mbar), see Fig. 3.7. Fluence was calculated assuming that no charge exchange has occurred between the switching magnet and the Faraday cup inside the FTIR chamber.

Valine samples, ~ 25 nm thick, were irradiated by 1.5 MeV N^{q+} with charge states q = 1, 2 and 3. Samples must be thin enough, not only to be traversed by the beam, but also for allowing it (ideally) to exit without reaching the equilibrium charge. On the other hand, 15-20 nm is typically the thinnest initial thickness range compatible to the infrared spectrometer sensibility, considering that the decrease of absorbances with beam fluence should be strong enough for permitting the σ_d^{ap} measurement.

For each experiment, the average σ_d^{ap} was calculated from three bands analyzed in Fig. 4.17 – see Table 6.6. Clearly, the higher the projectile charge, the greater the apparent destruction cross section measured.

Table 6.6: Apparent destruction cross sections of 1.5 MeV N^{q+} on valine samples.

Charge state	**σ_d^{ap} (10^{-13} cm^2)**			
	Analyzed band (cm^{-1})			**Average**
	3190-2430	**1602-1579**	**1337-1320**	
1+	1.4	1.4	2.2	1.7 ± 0.5
1+	0.96	0.96	2.2	1.4 ± 0.8
2+	1.9	2.1	2.9	2.3 ± 0.6
3+	6.5	6.3	6.5	6.4 ± 0.1

Under the perspective of a radiolysis analysis, Figure 6.15 (a) shows the average σ_d^{ap} dependence on q^2. Then, as $\sigma^{3+}/\sigma^{+} = 4.1$ and $\sigma^{2+} / \sigma^{+} = 1.5$, the average beam charge state ratios inside the samples are ~ 2.0 and 1.2 (instead of 3 and 2) for N^{3+}/N^{+} and N^{2+}/N^{+}, respectively. By combining Eq. (6.2) with Joy-Luo-Bethe-Bloch's formula [78, 62], the average cross section for a projectile with charge z and velocity v can be estimated as

$$\sigma_d^{ap}(q,v) = a\, S_e(q,v) = a\, S_e^{e-}(v)\, q^2 = \sigma_d^{ap}(e^-,v)\, q^2, \qquad (6.2a)$$

where $S_e^{e-}(v)$ and $\sigma_d^{ap}(e^-,v)$ are the stopping power and the destruction cross section for electron projectiles with the same velocity v, respectively. For a dominant radiolysis damage, a proportionality is expected in a graph $\sigma_d^{ap}(q,v)$ versus q^2, in which $\sigma_d^{ap}(e^-,v)$ is the angular coefficient, if no charge exchange occurs inside the sample. 1.5 MeV N ions and 59 eV electrons have the same velocity: $v = 4.5 \times 10^3$ km/s. For valine, $a = 1.0 \times 10^{-20}$ cm^3 keV^{-1}; 59 eV electrons have $S_e^{e-} \sim 8$ eV Å^{-1} = 8×10^5 keV cm^{-1}; the Joy-Luo formula with k = 0.6 provides $\sigma_d^{ap}(e^-,v) = 0.8 \times 10^{-14}$ cm^2. This result is to be compared with the angular coefficient of experimental data (dotted line in Fig. 6.15a), which is roughly 6×10^{-14} cm^2 (per square charge state). CasP results, imposing no charge exchange inside the sample, agree with the cross section ~ 1×10^{-14} cm^2 for q = 1; on the other hand, it predicts an angular coefficient of 0.4×10^{-14} cm^2, twice lower than Joy-Luo result, but much lower than the experimental value. A discussion on equilibrium charge state follows.

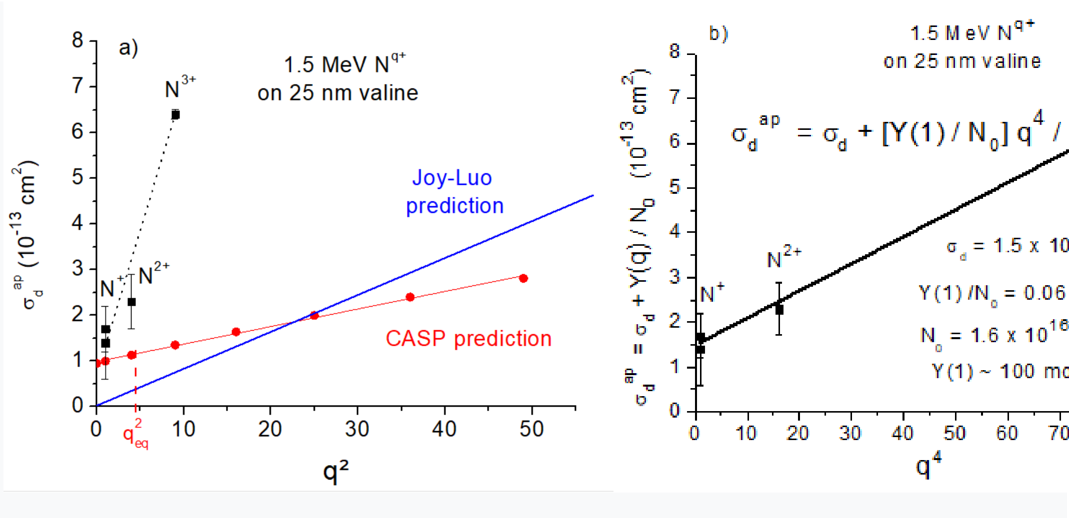

Figure 6.15: σ_d^{ap} dependence on initial beam charge state; 1.5 MeV N^{q+} beam impinging on valine 25 nm thick: q = 1, 1, 2 and 3. a) Linear fitting of data (dotted line) has a slope = 6 x 10^{-14} cm^2 per square charge state. The Bethe-Bloch's function prediction is valid if no charge exchange occurs. When a neutral 1.5 MeV N projectile enters in a solid target, it looses one or more electrons; therefore, in average, collisions in the bulk occur with $q \neq 0$ and σ_d^{ap} cannot be zero. In contrast, CasP predicts this stopping power (and σ_d^{ap}) correctly [77]. b) Assuming only sputtering ($\sigma_d^{ap} \sim q^4$).

Inside a solid, a projectile with initial charge state q captures and loses electrons until its charge state reaches an average equilibrium value, q_{eq} [79–81]. Equation (6.3) is the expression for this equilibrium charge according to Bohr's adiabatic criterion, where the projectile electrons with orbital velocities smaller than the projectile translation velocity are removed during the collision cascade with target atoms [82]; Z_p being the projectile atomic number, v its velocity and v_B the Bohr's velocity.

$$q_{eq} = Z_p \left[1 - exp\left(\frac{-125\ v}{137\ v_B Z_p^{2/3}} \right) \right] \tag{6.3}$$

Figure 6.16 presents the predicted equilibrium charge, acording to Eq. (6.3), in function of nitrogen projectile velocities. A nitrogen projectile with 1.5 MeV of kinetic energy has the velocity v = 0.45 cm ns^{-1} and a predicted equilibrium charge of q_{eq} ~ 2.8. Other q_{eq} expressions from more refined models, as those of Montenegro et al. (1982) [83], Heckman et al. (1963) [84] and Grande and Schiwietz (1998) [77] give similar results within 10% error [80]; for simplicity, Eq. (6.3) is the approach taken.

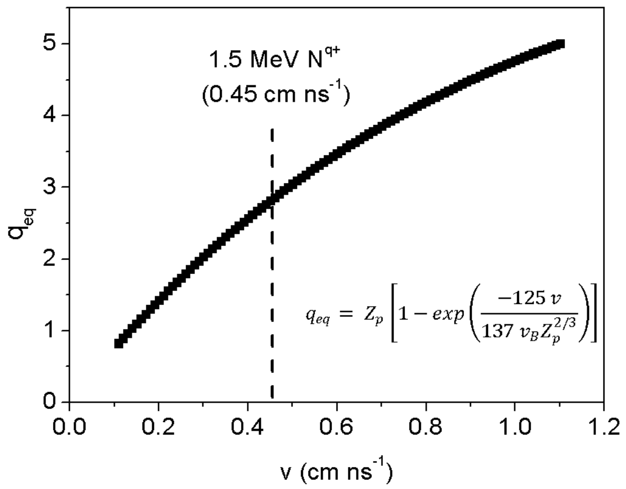

Figure 6.16: Equilibrium charge state in function of nitrogen ions velocities. The vertical dash line indicates the velocity of the beam used in this data set.

The projectile charge evolves asymptotically inside the material from q (the incident projectile charge) to reach q_{eq} (the final projectile mean charge). Between q and q_{eq} the charge has a transient or average value that is a function of the covered distance by the projectile, $q_{av}(s)$. Bohr has proposed that the projectile charge state inside a material should be written as Eq. (6.4) [85]:

$$q_{av}(s) = q_{eq} + (q - q_{eq})exp\left(-\frac{s}{\lambda_q}\right) \tag{6.4}$$

with s being the projectile's covered distance along the track, and λ_q the characteristic relaxation length of the solid. Based on Eq. (6.4), Fig. 6.17 presents $q_{av}(s)$ for 1.5 MeV N^{q+} ion beams with initial charge states q = 1 and q = 3 impinging on a solid of icy water. Both beams reach the equilibrium charge around s = 4 nm inside the sample. Although the λ_q value for valine is not known, the rougthly linear relationship between σ_d^{ap} and q^2 in Fig. 6.15 suggests that λ_q is is much higher than 4 nm and comparable to the sample thickness.

The disagreement by one order of magnitude presented in Figure 6.15 (a) reflects that either an experimental difficulty occurs (e.g., the actual beam charge state impinging on the sample is not well known), or sputtering is relevant. In the latter direction, Figure 6.15 (b) shows the average σ_d^{ap} dependence on q^4. Considering $Y(q) = Y(1)\, q^4$, the surprisingly good linear fitting $\sigma_d^{ap}(q) = \sigma_d^{ap}(0) + (Y(1)/N_0)\, q^4$ provides $\sigma_d^{ap}(0) = 1.5 \times 10^{-13}$ cm^2 and $Y(1)/N_0 = 0.061 \times 10^{-13}$ cm^2.

Since z_{sp} = 25 nm corresponds to $N_0 = 1.6 \times 10^{16}$ molec cm^{-2}, one gets Y(1) ~ 100 molec per impact.

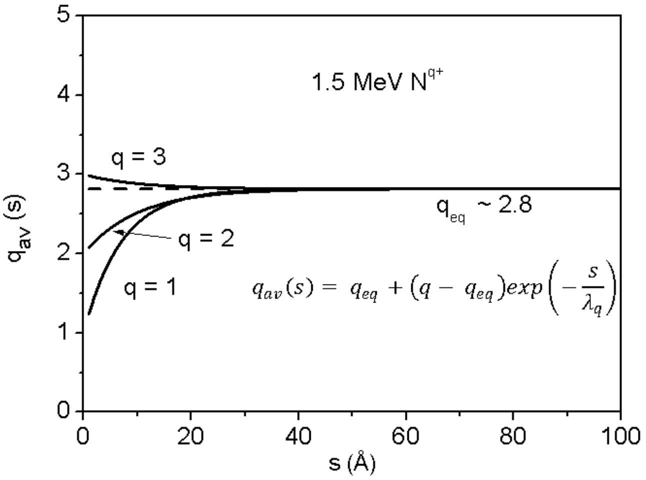

Figure 6.17: Average charge state curves in function of the distances reached inside a solid of icy water (λ_q ~ 10 Å) by 1.5 MeV N^{q+} ion beams with initial charges 1 and 3 [80]. For valine, λ_q is not known, but the order of magnitude is expected to be the same.

Sputtering measurement from distinct thick targets

Fig. 4.21 displays data of valine samples with distinct thicknesses bombarded by 1.5 MeV N$^+$. Figures 6.18 (a) – (c) present the normalized column densities for three samples as a function of F/N_0. The green dashed curves are fittings of the average behavior of the considered bands.

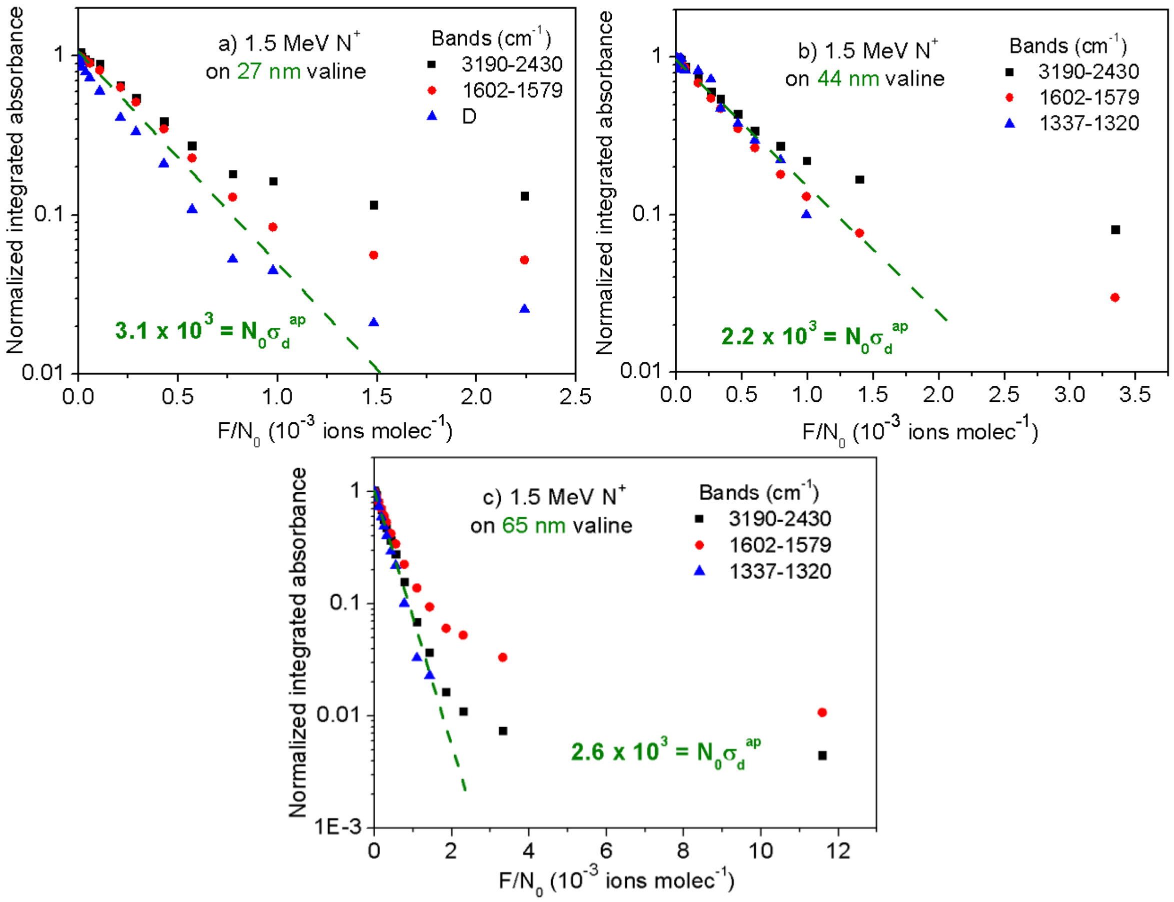

Figure 6.18: Normalized absorbance evolutions of valine (a) 27, (b) 44 and (c) 65 nm thick as a function of F/N_0; evolutions of the 3190-2430, 1602-1579 and 1337-1320 cm^{-1} bands were followed. The values $N_0\sigma_d^{ap}$ are a factor 2 higher than Y_0, evidence that radiolysis dominates over sputtering even for these relatively thin samples.

Another analysis of the same fact is exhibited in Fig. 6.19. The dispersion of the analyzed bands on each measurement is not negligible, see Table 6.7. Since $\sigma_d^{ap} = \sigma_d + Y_0/N_0$, the average σ_d^{ap} is plotted as a function of the inverse of the corresponding initial column density, in an attempt to measure individually σ_d and Y_0. From Fig. 6.19, Y_0 is approximately 1300 ± 700 molecules per impact, and $\sigma_d = (7.0 \pm 3) \times 10^{-14}$ cm^2. For thin and thick films, the sputtering yield is 2 to 20 times lower than the rate $N_0\sigma_d^{ap}$. The finding that $Y_0 \sim 10^3$ molecules per impact is to be compared with the sputtering yield for ices, which are two orders of magnitude higher (e.g., Mejía et al. (2020) [86]).

Table 6.7: Apparent destruction cross sections of 27, 44 and 65 nm valine samples.

Thickness (nm)	**N_0 (10^{16} cm^{-2})**	**σ_d^{ap} (10^{-14} cm²)**				**N_0 σ_d^{ap}**
		Analyzed band (cm^{-1})			**Average**	
		3190-2430	**1602-1579**	**1337-1320**		
25	1.6	9.6	9.6	22	14 ± 8	2240
27.5	1.8	14	14	22	17 ± 5	3060
44	3.0	7.1	7.9	-	10 ± 6	2250
65	4.4	5.4	6.2	6.4	6.0 ± 0.6	2640
230	15	7.2	-	7.6	11^* ± 4	$16x10^3$

*Average performed with the σ_d of the bands presented in the table and those of the 1279-1261, 957-937, 782-763, and 726-705 cm^{-1} bands [61].

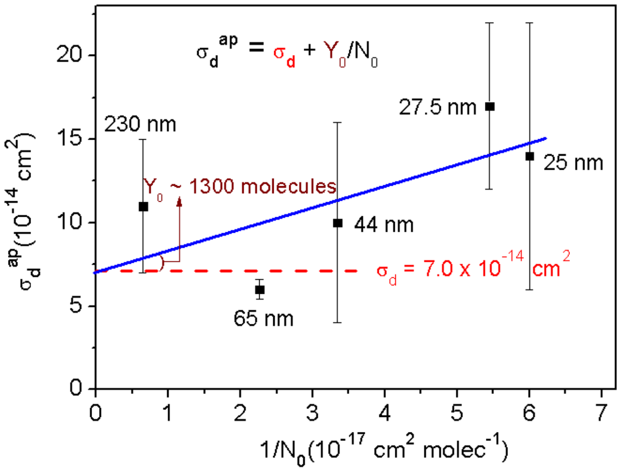

Figure 6.19: Average apparent destruction cross section of valine irradiated by 1.5 MeV N^+ in function of the inverse initial column density. Y_0 ~ 1300 ± 700 molecules/projectile and σ_d = (7.0 ± 3) x 10^{-14} cm^2 are the estimated sputtering yield and destruction cross section, respectively.

6.3
Electron beams

In this section, experimental data with keV electron beams and theoretical predictions from the CASINO-extended model are discussed (see sections 4.3 and chapter 5).

6.3.1
Experimental data

On sections 4.2.1 and 4.3.6, 1.8 MeV protons and 1.0 keV electrons were respectively employed in order to compare the glycine degradation by distinct ionizing projectiles with the same initial velocity and same incident charge (but opposite sign). The predicted ranges for 1.8 MeV protons and 1.0 keV electrons on glycine are about 40 µm and 29 nm, respectively [73, 62]. Though their electronic stopping powers traversing the sample surface are 27 and 26 keV μm^{-1} ([73, 62], respectively), the obtained cross sections differ by one order of magnitude, being (26 ± 15) x 10^{-16} cm^2 for 1.8 MeV H^+ and (2.7 ± 0.2) x 10^{-16} cm^2 for 1.0 keV e^- [63]. Obviously, the H^+ cannot increase its charge inside the target but may be neutralized or transformed, with very low probability, into H^-; anyhow, these charge exchanges do not explain the observations. A possible explanation is to consider the production of δ-electrons by the ion beam. These electrons have velocities comparable with the projectiles ones and are emitted forward, causing additional ionizations [87].

A crucial difference between the two systems is that the ionic projectiles cross a relatively thin sample without losing too much of their kinetic energy, but the electron beam deposits most or all its energy inside the target. For the latter, due to the different collisional energies, average stopping power values should be used: $<S_e> \sim E_0/R$, where E_0 is the incident energy and R the projectile range. Considering E_0 = 1.0 keV, then $<S_e> \sim 35$ keV μm^{-1} [63], a value greater than the initial 26 keV μm^{-1}. Again, this fact does not explain the differences between the measured cross sections, and goes – apparently – in the opposite direction because electron projectiles with greater stopping powers are more efficient for inducing molecular dissociations than protons with the same initial velocity.

Since cross section data from keV electron beams impinging on amino acids are scattered in literature (e.g., [23–26]), a systematic set of irradiations (for valine in particular) were performed in function of beam energy, and for distinct sample thickness and temperature. They are discussed below.

Cross section measurements

The analysis of integrated absorbances in function of beam fluence, S(F), is the same as the previously one described for ions. Data are fitted by Eq. (6.5):

$$S(F) = S_0 e^{-\sigma_d^{eff} F} + S_\infty \qquad (6.5)$$

where S_∞ is the integrated absorbance at high fluences, and $S_0 + S_\infty$ the initial integrated absorbance for a given band. $S_\infty = 0$ if the analyzed band absorbance vanishes when F tends to infinity; σ_d^{eff} is the cross section representative of all collisions inside the solid and should not be confused with the binary collision σ_d, which is well defined for a specific beam energy. σ_d^{eff} is extracted directly from the absorbance evolution, considering no crystallographic corrections due to molecular rearrangements during the irradiation. The average σ_d^{eff} value, calculated from the analysis of several bands, is defined as the destruction cross section of the precursor material. Besides its dependence on energy, σ_d^{eff} *depends on sample thickness.*

Equations (6.1) and (6.5) differ to each other only in concepts of σ_d^{ap} and σ_d^{eff} cross sections. The former (*apparent destruction cross section*) means that two processes exist (radiolysis and sputtering) and their effects are such that can be described by a single quantity, $\sigma_d^{ap} = \sigma_d + Y_0/N_0$. The latter (*effective destruction cross section*) means that, for thick samples, multiple collisions are occurring, each of them with a distinct σ_d, since the projectile energy is varying along the collision cascade; σ_d^{eff} corresponds to the overall radiolysis damage. A consistent way to express concomitantly both concepts is: $\sigma_d^{ap} = \sigma_d^{eff} + Y_0/N_0$.

Dependence on sample thickness

Valine samples with distinct thicknesses were irradiated by 0.1 and 1.0 keV electrons, see section 4.3.2. Figure 6.20 shows that σ_d^{eff} decreases when the sample thickness increases for both beams; this explains, at least partially, why data on literature are so disperse. Indeed, Pilling et al. (2014) [24] and Maté et al. (2015) [25] have found discrepant results when bombarding glycine with 2.0 keV electrons; the former group used a thick sample, ~ 1 µm, while the latter bombarded a thinner one, ~ 0.1 µm. They found the cross sections $(1.8 \pm 0.2) \times 10^{-16}$ cm^2 and $(17.6 \pm 1) \times 10^{-16}$ cm^2, respectively: thicker samples correspond to lower cross sections.

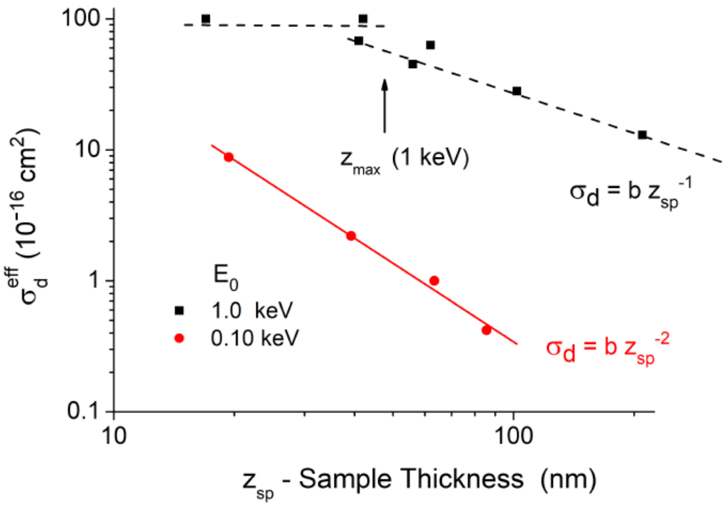

Figure 6.20: Valine σ_d^{eff} dependence on sample thickness z_{sp}. Red circles and black squares correspond to 0.1 and 1.0 keV electron beams, respectively. Lines are just guides; as a reference, z_{max} ~ 50 nm is the maximum depth reached by 1.0 keV electron projectiles, for an incident angle of 40^o.

In Fig. 6.20, it is noticeable that for 1.0 keV electron beam irradiation of samples with thicknesses $z_{sp} < z_{max}$, where z_{max} is the range predicted by CASINO, the σ_d^{eff} values are practically constant. Thickness $z_{sp} > z_{max}$ means that the beam projectiles do not traverse the sample and deposits their entire energy in it. A relevant question is: if projectiles stop before the depth z_{max} (~ 50 nm for 1.0 keV e^-), why σ_d^{eff} changes for thicker samples? We attribute this to the occurrence of sputtering: i) samples become thinner with fluence and may be degraded completely; and ii) during this process, radiolysis proceeds at different rates with depth, so that inhomogeneity of precursor's concentration also varies with depth and fluence.

The $\sigma_d^{eff} = b\ z_{sp}^n$ dependence is found for both energy beams, with n ~ -1 and ~ -2 for 1.0 and 0.1 keV e^- respectively. This empirical relationship indicates that the lower the penetration range of the beam, the lower is σ_d^{eff} and steeper is its decrease with z_{sp}. On one hand, the higher E_0, the higher the number of precursors destroyed per projectile and the higher dN/dF; but on the other hand, for a thick target, the higher E_0, the higher z_{max} and the number of processable precursors, N_{max}. By definition, cross section increases with the number of destroyed precursors but decreases with N_{max}.

Dependence on beam energy

Valine samples with fixed thickness values have been bombarded by beams with various energies. Figure 6.21 presents the σ_d^{eff} dependence on the incident beam energy: $\sigma_d^{eff} = aE_0^n$, with n ~ 1.5. Interestingly, this value of n is about the same as that predicted by Joy & Luo (1989) [62] for the range of keV electrons: $R \sim E_0^{1.6}$.

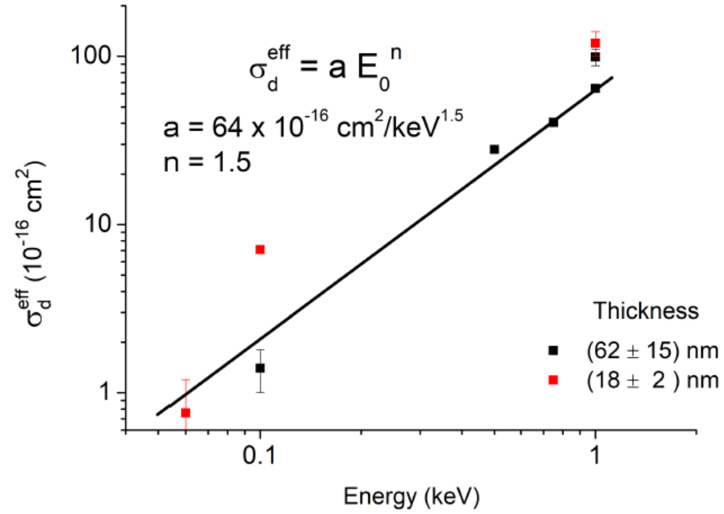

Figure 6.21: Dependence of valine effective destruction cross section on the electron beam energy for samples with 62 and 18 nm, black and red squares respectively.

Although the correlation between σ_d^{eff} and R appears enough to explain observations, the discussion is more complex and not completely clear.

If the beam traverses the sample, then $N_{max} = N_{sp}$ does not depend on E_0; moreover, the depth of highest energy deposition, z_0, is very likely shorter than the sample thickness, z_{sp}. Since $z_0 \sim E_0^{1.6}$ (see Fig. 5.4), it is then reasonable that σ_d^{eff} increases accordingly.

If the electron beam does not traverse the sample, increasing E_0 increases proportionally the number of precursors destroyed but also increases N_{max}. The overall effect is to decrease σ_d^{eff}, contrary to observations (Fig. 6.21). The crucial point here is to know whether S_∞ was correctly determined. Even so, for very thick targets, one should expect that dN/dF would be the same for different sample thicknesses, since precursor molecules at the rear part of the sample act as spectators. This goes against measurements (see Figs. 4.27 and 6.20), which suggest that thick targets are morphologically harder to be damaged (they have lower σ_d^{eff}).

Figure 6.22 points out that, in the energy range of 0.06 – 1.0 keV for electrons impinging on glycine, several models predict that the electronic stopping power (and hence the destruction cross section) presents a maximum and then decreases with the increasing electron energy [78, 62, 88, 89]. Predictions displayed in Fig. 6.22 are however valid only for single energy values (very thin films or gaseous targets), while experimental data obtained from solid targets provides average σ_d^{eff} values that are due to a cascade of elastic and inelastic collisions.

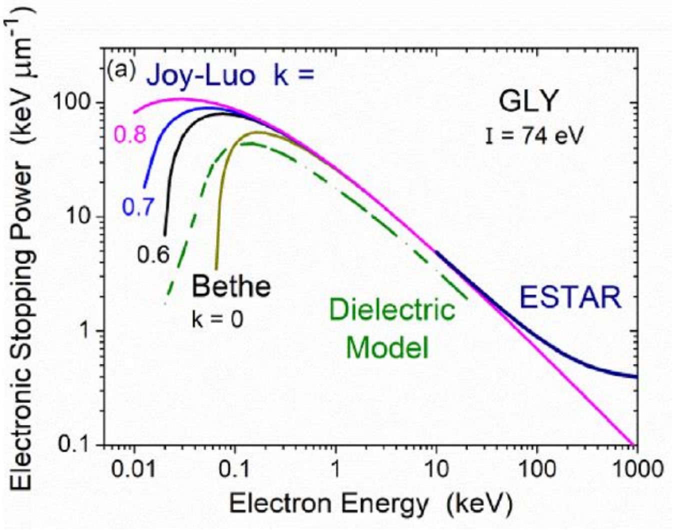

Figure 6.22: Electronic stopping power dependence on energy of electron projectiles bombarding solid glycine, acording to Joy-Luo [62] (for three k values), Bethe [78] and Dielectric model [89] predictions. ESTAR [88] results are also shown.

Dependence on sample temperature

Valine sample ~ 60 nm thick was bombarded by 1.0 keV electrons. Figure 6.23 presents the σ_d^{eff} dependence on sample temperature, analyzed for four selected bands; for each temperature, σ_d^{eff} values vary up to a factor $\lesssim 2$. This characteristic has also been observed by Gerakines et al. (2012) [16], and is evidence that temperature alters the precursor’s chemical environment.

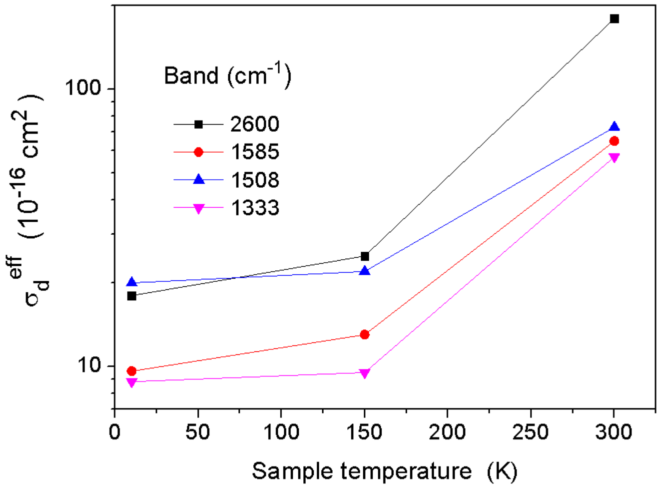

Figure 6.23: σ_d^{eff} dependence on sample temperature of valine samples bombarded by 1.0 keV electron beams.

Cooling down from room temperature to 150 K, valine σ_d^{eff} decreases steeply, and between 150 and 10 K, decreases slowly. A similar tendency has been reported by Maté et al. (2015) [25] and Souza-Corrêa et al. (2019) [26] for glycine at ~ 20 – 300 K being bombarded by 2.0 and 1.0 keV electrons, respectively. The former found that σ_d^{eff} decreases by a factor 2, cooling down the sample from 300 to 20 K.

The apparent destruction cross sections of MeV ions present a distinct behavior compared with those of keV electrons. This fact may be interpreted by the very different defect density produced in the solid by the two beams: electron beams create a higher defect concentration close to the material surface.

6.3.2

Predictions from CASINO-extended model

As presented in chapter 5, simulations carried with CASINO code, complemented by those of the CASINO-extended model, are a powerful tool for studying the degradation of organic targets by keV electron beams. In particular, they depict the electron projectile-atom interaction, predicting damage profiles based on the projectile energy loss inside the material.

Neglecting sputtering effects, the CASINO-extended model mainly predicts that:

i) At a certain fluence, the damage caused on thick samples highlights four regions: a) mildly processed surface, b) heavily degraded bulk, c) slightly processed interface, and d) non-processed rear. At very high fluences, the bulk and the surface ones are completely depleted of precursors, while the interface region slowly becomes thinner and the sample column density, $N_{sp}(F)$, decays asymptotically to the plateau N_∞, correspondent to the region never processed by the beam.

ii) At first, as fluence increases, the column density decays rapidly due to the high dissociation rate of abundant precursor molecules located in between the sample surface and the interface with the non-irradiated region. At higher fluences, the frontal region becomes depleted of precursors and the column density decrease is ruled by the always relatively low degradation rate at the interface.

iii) As shown in Eq. (5.7), N(F) is a sum of exponentials, instead of a single exponential function: in principle, *it is not possible to associate the column density evolution with fluence to a defined cross section*. Nevertheless, at low fluences, the electron beam degrades the sample in a way that a dominant σ_i-group rules over the others in the sum of exponentials. They have cross sections slightly above σ_0 and impose how fast the destruction of the bulk happens. At high fluences, a second dominant group takes over, indicating a slow degradation of the interface region. The average behavior is a function N(F) similar to two decaying exponentials or to one exponential and a constant, as in Fig. 5.8 (a) and Eq. (6.5) respectively.

iv) At low fluences, the net destruction cross section, σ_0, decreases with the initial electron energy as $E_0^{-0.6}$ (Fig. 5.5).

v) The rate $dN/dF = \sigma_d N$ increases with the incident projectile energy, E_0. However, this happens because z_{max} increases with E_0, and so does the number N_{max} of processable molecules, and not because the destruction cross section σ_d increases. Indeed, from Eq. (5.6), σ_0 decreases with $E_0^{-0.6}$, while z_{max} and, N_{max}

increases with $E_0^{1.6}$. In general, fittings with Eq. (6.5) based on data acquired from too short experiments prevent the S_∞ determination, or generate S_∞ attached to huge errors since the interface region has not been well defined yet. The consequence is that the faster decay of dN/dF with E_0 is mistakenly attributed to an increase of the destruction cross section, as seen in Figs. 5.8 (a) and (b).

vi) CASINO takes into account the backscattered electrons; ~ 10% of the beam projectiles, for keV electrons, escape back through the sample surface taking away ~ 5% of the incident energy. In the case of thin targets, the energy loss of projectiles transmitted throughout the sample is also considered by CASINO. Both outputs are important to estimate correctly the deposited energy on the analyzed material.

vii) Temperature effects are not taken into account on CASINO calculations (with exception of minor alterations such as the material density). Nevertheless, σ_0 may disclose those effects, assuming that D_0 depends on temperature (see Eq. 5.6).

viii) In the CASINO-extended model, projectile trajectories do not interfere with each other. No beam current effects are considered, including sublimation. This is not an issue for the current data, since Figure 4.24 shows that, at the nA – µA range, the degradation of two bands of valine has a low dependence on the electron beam current.

The above topics establish the background necessary to compare experimental and predicted data.

From Eq. (6.5), the measured effective destruction cross sections for E_0 = 1.0 keV are about (50 to 100) x 10^{-16} cm^2, a factor ~ 2 to 3 times higher than the predicted $\sigma_0 \approx 30 \times 10^{-16}$ cm^2 (for z_{max} ~ 47 nm).

Figure 4.27 shows that, for E_0 = 0.1 and 1.0 keV, dN/dF decreases if sample thickness increases. This trend agrees with the tendency predicted by the model for the case of samples thicker than 15 nm, see Fig. 5.10. The σ_d^{eff} dependence on valine thickness is summarized in Fig. 6.20, and compared with predictions displayed in Figs. 5.6, 5.10 and 5.11.

There is a good agreement for very thin targets, 10 – 20 nm, when the destruction cross section is relatively high. When the sample thickness increases, the damage at the rear part of the sample is gradually reduced, and the average cross section value decreases.

In Figs. 5.10 and 5.11, the evolutions of experimental $N_{sp}(F)$ are compared with the model predictions. The results for a 62 nm valine bombarded by electrons of 0.1, 0.50, 0.75 and 1.0 keV show that the higher the beam energy, the faster is the sample degradation. Notice that, with exception of 0.1 keV data, the predicted degradation rates are lower than the measured ones, Fig. 5.10. This finding is corroborated by data presented in Fig. 5.11, where the sample thickness varies but E_0 is fixed at 1.0 keV.

Furthermore, even though CASINO estimates z_{max} ~ 47 nm for E_0 = 1.0 keV, thicker target samples are completely depleted at the end of irradiation, as seen in Fig. 6.24. This is evidence that sputtering is also playing a relevant role in valine degradation by electron beams, so that σ_d^{eff} (defined by Eq. 6.5) should also be related to σ_d^{ap}, as for the case of ion beams.

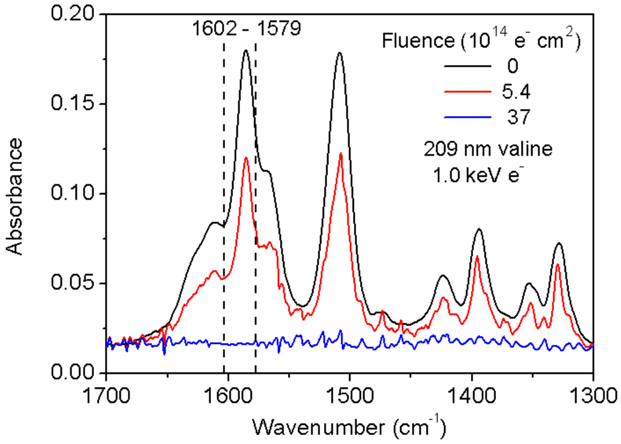

Figure 6.24: Zoom at the 1700 – 1300 cm^{-1} IR region for three fluences of a 1 keV electron beam bombarding a 209 nm valine film.

Sputtering treated by the CASINO-extended model

In section 5.3.1, experimental $N_{sp}(F)$ is compared with CASINO predictions. Figs. 5.11 and 5.12 show that observed degradation occurs faster than the theoretical results and one very likely reason is that the proposed model does not take sputtering effects into account. The way of introducing this process in the model is [63]:

a) The sputtering is a superficial process in which the total atomic sputtering yield is reasonably constant along the irradiation; radiolysis induces molecular modifications in the sample's processable region;
b) The model considers that sputtering removes completely the first sublayer after a certain fluence, independently of its chemical composition. The total sputtering yield corresponds to the emission of Y_0 precursors per impact.
c) For CASINO calculations, the sample is divided into i_{max} sublayers; as an approximation, the surface is considered the 1st sample sublayer (N_i, with i = 1).
d) The partial sputtering yield of precursors decays with beam fluence because radiolysis decreases their concentration $C_1(F) = N_1(F)/N_1(0)$ at the surface. Then, $Y(F) \cong Y_0\ C_1(F) = Y_0 \exp(-\sigma_1\ F)$, where σ_1 refers to the destruction cross section of the 1st sublayer;
e) The FTIR technique cannot discriminate the precursor depletion by sputtering (ejection) or by radiolysis (dissociation). The sum of both effects is represented by a value called apparent destruction cross section, σ_d^{ap} [90, 60].
f) Combing all these considerations, the apparent destruction cross section is applied just for the 1st sublayer: $\sigma_d^{ap} = \sigma_1 + Y_0 /N_1(0)$; for all layers, $\sigma_i = \sigma_0\ i_{max}\ CL_{i.}$.

A rough estimate is done below to investigate the sputtering effects on a valine sample. Since the volume of a single valine molecule is $V_m = 1.478 \times 10^{-22} cm^3$, each monolayer is $z_1 = V_m^{1/3} = 0.5287$ nm (5.3 Å) thick. The molecular area is $A_m \sim z_1^2 = 2.796 \times 10^{-15}\ cm^2$; therefore, there is 3.577×10^{14} valine molecules per cm^2 on the sample surface.

To remove a molecular monolayer, by sputtering, it is necessary a fluence $\Delta F_m = \frac{1}{Y_0 A_m}$, or $\Delta F_m = \frac{3.577 \times 10^{14}}{Y_0}$. To remove 1 nm of material, $\Delta F_1 = 1.89\ \Delta F_m$, since ~1.89 valine diameters correspond to 1 nm depth. For modelling purposes, it is assumed that $\Delta F_1 = 2.5 \times 10^{13}\ e^-\ cm^{-2}$ is the fluence necessary to eject 1 nm of valine; the obtained yield is $Y_0 = 3.577 \times 10^{14}/\ \Delta F_m = 1.89 \times 3.577 \times 10^{14}/\ \Delta F_m$. That is, $Y_0 \sim 27$ molecules per electron impact.

Figure 6.25 presents the predictions of sputtering and radiolysis effects of a valine film, 80 nm thick, being bombarded by 1 keV electrons at $\theta = 40°$. It is considered that each cycle of fluence ΔF_3 removes 3.0 nm of material. After 15 cycles, 45 nm of the sample are ejected – which is approximately the range for 1 keV electrons. The entire region processed by radiolysis since the beginning of the irradiation is then removed by sputtering. Up to this fluence, the sample column density, $N_{sp}(F)$, decreases quickly due to radiolysis and sputtering, both exhibiting an exponential-like behavior: σ_d^{ap} for the first sublayer and the CASINO'S σ_i for the others. The depth profile of precursor concentration changes continuously and "moves" towards the surface because sputtering is removing the sample material (precursor and products) from the surface. The precursor sputtering yield decreases, while those of products increase; the total sputtering remains constant as far as preferential sputtering of chemical elements or functional groups is not considered: $dN_{sp}/dF = Y_0$.

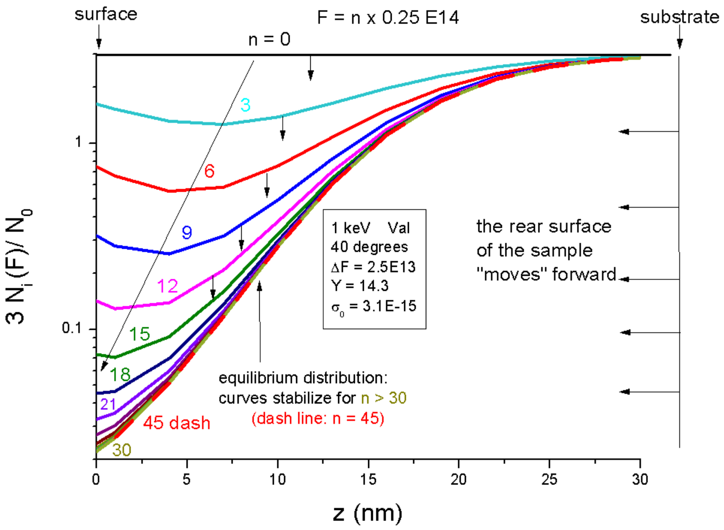

Figure 6.25 (a): Radiolysis degradation profile as a function of depth and for progressive fluences. Maximum degradation occurs at z = 9 nm; maximum penetration: $z_{max} \sim 40$ nm. Each curve corresponds to the ejection of 3 x 0.25 x 10^{14} molecules or 3 nm of valine. Sputtering removes material from the sample surface with the yield $Y_0 = 14$ molec/impact. Since the origin of depth is the beam entrance surface, the degraded material appears to move left, towards the surface.

From the moment that the material initially at the rear part of the sample reaches the surface and starts to be sputtered, the precursor concentration along the sample stabilizes in a sigmoid profile (red dash line in Fig. 6.25 (a)). The transient regime has been converted into the stationary regime: the sputtering yields of precursor and products become individually constant with fluence [91]. The precursor column density, $N_{sp}(F)$, decreases linearly with fluence because both sputtering and radiolysis degradation rates also become constant. It can be demonstrated that the sputtering yield of precursor molecules, which is Y_0 at the beginning of irradiation, decreases and in the stationary regime levels off at:

$$\frac{dN_{sp}^{st}(F)}{dF} = -Y_0\, e^{-\left(\frac{E_0}{D_0 Y_0}\right)} \tag{6.6a}$$

Eq. (6.6a) predicts that, for high fluences, $\exp(-E_0/(D_0Y_0))$ is the survival probability for a precursor molecule, leaving the rear region, reach the sample surface. This probability is high under one or both conditions: i) the molecular radioresistance is high (low σ_d or high D_0) and ii) Y_0 is high and the molecule traverses "quickly" the region damaged by the beam. The assumption that the total sputtering yield is always equal to Y_0 implies that the radiolysis rate must be

$$\frac{dN_{rd}^{st}(F)}{dF} = -Y_0\left[1 - e^{-\left(\frac{E_0}{D_0 Y_0}\right)}\right] \tag{6.6b}$$

Fig. 6.26 illustrates the predicted N(F) behavior when radiolysis and sputtering occur simultaneously in a thick valine sample.

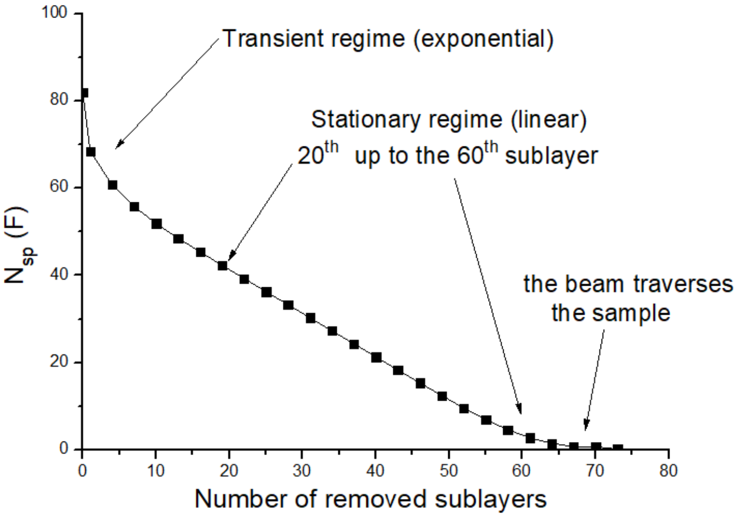

Figure 6.25 (b): Same data as (a), but integrated along the sample depth. The transient regime is the one usually analyzed by researchers. The stationary regime starts when the interface region of the irradiated sample begins to be sputtered and finishes when the beam reaches the end of the sample.

6.4
Data comparison and applications

Physicochemical phenomena require energy to occur, then it is natural to link the material degradation with the beam stopping power (of course, non-linear effects may be involved, but in general they may be treated as second order or, at least, require clear experimental evidence to be considered as first order). Table 6.8 summarizes the experimental results presented in chapter 4. Several distinct projectiles were employed to probe the three selected amino acids, and to obtain their respective apparent destruction cross sections. In turn, Table 6.9 presents literature data of amino acids and the nucleobase adenine processed by MeV and keV ions, and keV electrons.

The MeV ionic projectiles traverse throughout thin samples (beam range >> sample thickness), while keV electron projectiles are usually stopped even in relatively thin targets. S_e values for ion projectiles are obtained by the codes TRIM and CasP [73, 77] – the latter was only employed for S_e calculation of multi-charged beams.

The Joy-Luo expression [62], Eq. (6.7), was used to predict the stopping power behavior of non-relativistic electrons impinging on valine, Fig. 6.26 (a).

$$S_e = -785\,\frac{\rho Z}{EA} ln\left[\frac{1.166\,(E + k\mathrm{J})}{\mathrm{J}}\right]\;eV/\text{Å} \qquad (6.7)$$

where ρ, Z and A are the material density, atomic number and atomic weight, respectively. E is the electron beam energy, J is the mean ionization potential in eV, and k a constant that depends on the material characteristics. Since the predictions of Bethe are not suitable for low energy projectiles, Joy & Luo (1989) [62] have proposed this expression adding the kJ term on Bethe's original stopping power equation [78], which improves the agreement with experimental data. For valine: $\rho = 1.32$ g/cm^3, $Z/A \sim 0.79$, $J = 67.8$ eV according to Bragg's additivity rule, and predictions for several k are shown in Fig. 6.26 (a), k = 0.6 being the chosen value for the obtained stopping power and range information on Table 6.8.

Instead of using the S_e values for specific energies predicted by Joy-Luo, the average stopping power, $<S_e>$, is considered to take into account the projectile slowing down in the sample. The average stopping power is calculated by Eq. (6.7), where E_0 is the incident electron energy, $E_{min} \approx 50$ eV is the projectile energy threshold, below which the induced molecular excitations are extremely weak [92], and R is the range reached by the projectiles according to Joy-Luo predictions shown in Fig. 6.26 (b): $R = \int_{E_0}^{E_{min}} \frac{dE}{S_e}$. For instance, electrons with $E_0 < 1$ keV have ranges R from ~ 1 – 32 nm, which means that ~ 2 – 60 valine molecules can be ionized by a single projectile.

Bethe and Joy-Luo predictions do not give information about the projected range (or average penetration depth), R_p. Monte Carlo codes like CASINO or ESTAR are the right options in this case; the detour factor, R_p/R, is always < 1.

$$< S_e > = \frac{E_0 - E_{min}}{R} \tag{6.8}$$

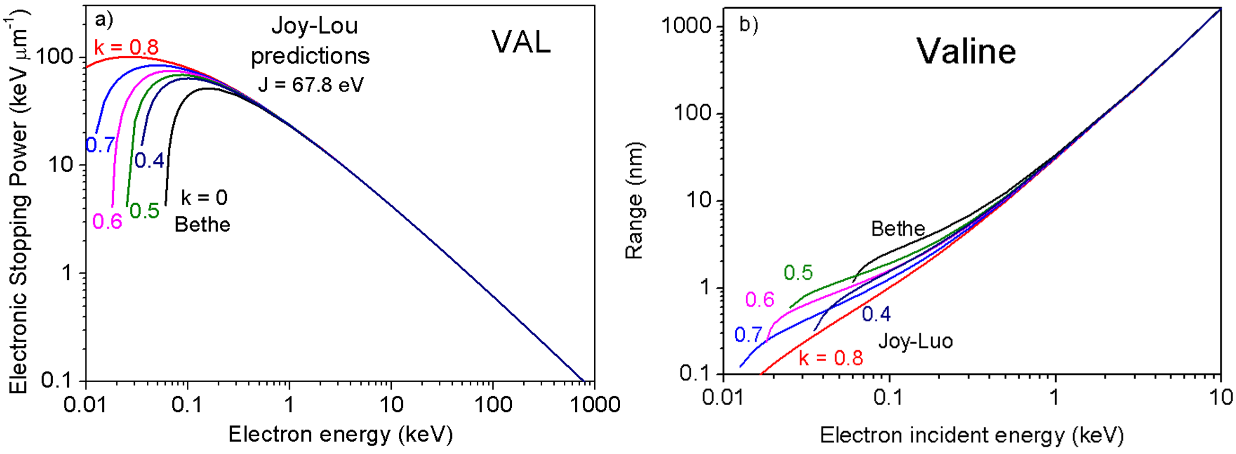

Figure 6.26: Electron beam on valine. (a) Stopping power and (b) range dependence on electron kinetic energy as predicted by Bethe, and Joy-Luo, for five k values.

Table 6.8: Apparent destruction cross section results of amino acids bombarded by MeV ions and keV electrons.

Projectile	Energy (MeV)	Sample	T (K)	Sample Thickness (nm)	Beam Range (nm)	$<S_e>$ (keV μm^{-1})	σ_d^{ap} (10^{-16} cm^2)
H^+	1.8	α-Glycine[1]	300	196	41300	27	26 ± 15
He^+	1.5		300	190	5210	285	250 ± 80
N^+	1.5		300	214	2260	1098	790 ± 200
H^+	1.5	D-valine[2]	300	2400	34900	26.7	26 ± 16

He^+	1.5		300	960	5790	251.7	540 ± 210
N^+	1.5		300	230	2440	998	1100 ± 400
N^+	1.5		300	230	2440	998	1300 ± 100
N^{2+}	1.5		300	618	1900	1134**	1000 ± 70
N_2^+	0.75		300	674	953	1020***	2500 ± 400
N_2^+	0.75		300	643	953	1020***	1500 ± 400
S^{15+}	230		300	580	97320	1690	3400 ± 400
N^+	1.5	L-valine	300	25	2440	998	1700 ± 500
N^+	1.5		300	25	2440	998	1400 ± 800
N^+	1.5		300	27.5	2440	998	1700 ± 500
N^+	1.5		300	44.2	2440	998	1000 ± 600
N^+	1.5		300	64.9	2440	998	600 ± 60
N^{2+}	1.5		300	25	1900	1134**	2300 ± 600
N^{2+}	6.0		300	25	8300	1046**	1500 ± 740
N^{3+}	1.5		300	25	1600	1350	6400 ± 100
H^+	0.5	Phenylalanine[3]	300	241	6760	50.4	95 ± 15
H^+	2.0		300	346	59300	20.4	30 ± 4
H^+	2.0		300	241	59300	20.4	31 ± 5
He^+	2.0		300	346	8480	204	306 ± 72
N^+	0.5		300	346	1210	544	754 ± 15
N^+	2.0		300	346	2980	1082	1380 ± 38
e^-	0.001*	L-valine[4]	300	50	31.9	29.8	0.77 ± 0.02
	0.001		300	50	31.9	29.8	0.6 ± 0.06
	0.0001		300	19.4	1.59	31.4	9.4 ± 0.6
			300	39.2	1.59	31.4	2.2 ± 0.2
			300	63.4	1.59	31.4	1.4 ± 0.5
			300	85.7	1.59	31.4	0.42 ± 0.01
	0.001		300	16.5	31.9	29.8	110 ± 10
			300	40.5	31.9	29.8	72 ± 5
			300	42	31.9	29.8	110 ± 10
			300	56	31.9	29.8	60 ± 4
			300	60.6	31.9	29.8	61 ± 4
			300	100.6	31.9	29.8	22 ± 2
			300	209.1	31.9	29.8	12 ± 1
	0.0001		300	55	1.59	31.4	1.4 ± 0.4
	0.0005		300	55	10.7	42.1	28 ± 1
	0.00075		300	55	19.5	35.9	40 ± 1
	0.00006		300	18	1.05	9.5	0.31 ± 0.01
	0.00006		300	18	1.05	9.5	0.08 ± 0.04
	0.0001		300	18	1.59	31.4	7.1 ± 0.2
	0.001		300	18	31.9	29.8	120 ± 20
	0.001		300	60	31.9	29.8	94 ± 86
	0.001		150	60	31.9	29.8	17 ± 8
	0.001		80	60	31.9	29.8	50 ± 24
	0.001		10	60	31.9	29.8	14 ± 6
	0.001		300	209	31.9	29.8	11 ± 1
	0.001		300	206[a]	31.9	29.8	10 ± 2
	0.001		300	221	31.9	29.8	9.5 ± 0.5
	0.001		300	164[a]	31.9	29.8	14 ± 2
	0.002		300	665	68.6	28.4	0.18 ± 0.02
	0.002		300	289[a]	68.6	28.4	0.032 ± 0.01
	0.001	α-Glycine[1]	300	150	28.8	35	2.7 ± 0.2

*i = 1.5 µA; ^{a} annealed sample; [1]da Costa et al. (2021) [54]; [2] da Costa et al. (2020) [61]; [3]Mejía et al. (2021) [51]; [4] da Costa et al. (2021b) [63]
**Calculated with CasP [77].
***Assuming that $N_2^+ = 1.07 \times 2\ N^+$; with S_e(0.375 MeV N^+) = 476 keV µm^{-1}. The vicinage effect should occur only in the first layers [93, 94].

Figure 6.27 displays the destruction cross sections presented in Tables 6.8 and 6.9 as a function of their respective average stopping powers. Data from ionic projectiles lay around the dashed line representing the proportionality between σ and S_e, while the great majority of experiments performed with electron beams provide cross sections lower than predicted by $\sigma = a\ S_e$.

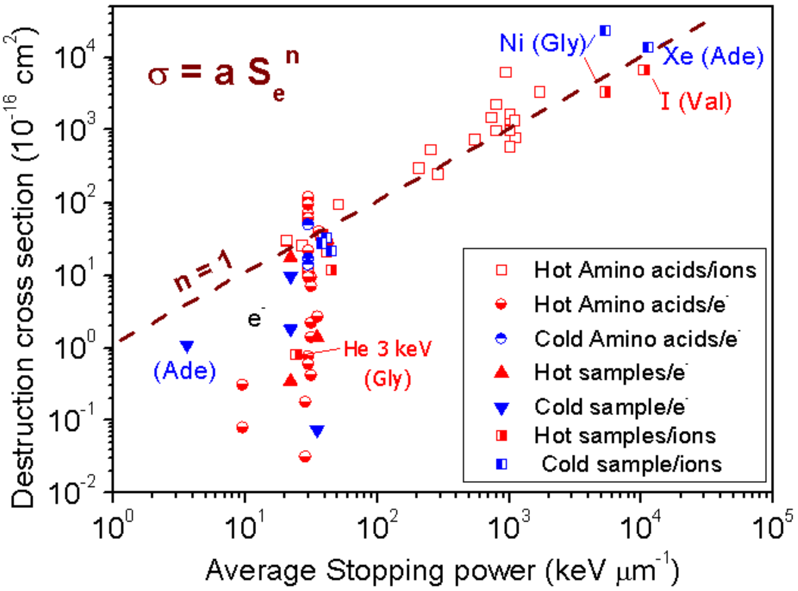

Figure 6.27: Apparent destruction cross section dependence on the average stopping power of electron and ion beams bombarding the amino acids glycine, valine and phenylalanine (this work), and similar organic samples (literature); see Tables 6.8 and 6.9, respectively.

As discussed in section 6.3, the effective destruction cross section of electrons bombarding amino acids depends on sample characteristics (such as its thickness and probably the sample preparation mode). Analyzing the experimental points distribution in Fig. 6.27, it is tempting to associate the absence of data below <Se> ~ 10 keV µm^{-1} to a threshold stopping power, S_e^{th}. The molecular volume V_m for Gly, Val and Phe are presented in Table 6.5; $\sigma_m = V_m^{2/3}$ is the area of the respective molecule in cm^2. Thus, according to Eq. (6.2), $S_e^{th} = (1/a)\ \sigma_m$; in words, S_e^{th} is the minimum stopping power value necessary to degrade, statistically, a molecular column of one length unit. Parameters for the three amino acids are presented in Table 6.10.

Table 6.9: Literature data of different ionizing sources degrading amino acids and the nucleobase adenine.

Ionizing source	**Sample**	**T (K)**	**Sample Thickness (nm)**	**$\langle S_e \rangle$ (keV µm^{-1})**	**σ_d^{ap} (10^{-16} cm^2)**	**Reference**
2 keV e^-	Glycine	20	85	22	9.7 ± 1	Maté et al. (2015) [25]
		40	80		8.2 ± 1	
		90	35		9.5 ± 1	
		90	90		8.7 ± 1	
		300	90		17.6 ± 1	
2 keV e^-	Glycine	14	800	22	1.8 ± 0.2	Pilling et al. (2014) [24]
		300	3500		0.35 ± 0.07	
1 keV e^-	Glycine	40	160	35	0.074 ± 0.004	Souza-Corrêa et al. (2019) [26]
		80			0.072 ± 0.004	
		300			1.4 ± 0.02	
3 keV He^+	Glycine	300	1600	24	0.82 ± 0.2	Deduced from Foti et al. (1991) [29]
).8 MeV H^+	Glycine	15	500 – 2000	44.4	22 ± 2	Gerakines et al. (2012) [16]
		100		44.4	12 ± 1	
		140		44.4	12 ± 2	
	Alanine	15		40.8	33 ± 1	
		100		40.8	19 ± 1	
		140		40.8	21 ± 2	
	Phenylalanine	15		37.3	28 ± 3	
		100		37.3	15 ± 3	
		140		37.3	36 ± 2	
1 MeV H^+	Glycine	300	500	38.5	37 ± 26	Deduced from Pilling et al. (2013) [17]
6 MeV Ni^{11+}	Glycine	14	1700	5270	(24 ± 4)x10^3	Portugal et al. (2014) [18]
		300	500	5270	(3.4 ± 1.8)x10^3	
5 keV e^-	Adenine	11		3.62	1.1 ± 0.3	Evans et al. (2011) [27]
90 MeV I^{14+}	Valine	300		10400	(6.8 ± 1.8)x10^3	Salehpour et al. (1984) [15]
92 MeV Xe^{23+}	Adenine	13	290	11200	(14 ± 1) x 10^3	Vignoli Muniz et al. (2017) [19]

Table 6.10: Glycine, valine and phenylalanine respective minimum area, σ_m, inverse of the deposited energy density, *a*, the apparent deposited dose, D_0^{ap}, and threshold stopping power, S_e^{th}.

Material	**σ_m (10^{-14} cm^2)**	***a* (10^{-20} cm^3 keV^{-1})**	**D_0^{ap} (eV molec^{-1})**	**S_e^{th} (keV µm^{-1})**
Glycine	0.18	0.8	10 ± 4.5	22.5
Valine	0.29	1.0	16 ± 2.0	29.0
Phenylalanine	0.35	1.5	14.3 ± 2.2	23.3

According to Fig. 6.26 (a), the valine S_e^{th} corresponds to electrons with a threshold collision energy E_{th} ~ 700 eV (Observation: 23 eV electrons have also the same stopping power value, but they are not taken into account since their energy is below E_{min}). This means that, in average, projectiles with $E_0 > E_{th}$ have stopping power < S_e^{th} and need to collide a certain number of times to lose energy and reach the energy range where degradation becomes significant. In summary, for $E_0 < E_{min}$, the electron destruction cross sections are negligible, and for $E_0 > E_{th}$, the sample surface is less destroyed than the bulk.

For both glycine and valine, their maximum S_e correspond to the 30 – 100 eV energy range, reason why $<S_e>$ is greater than S_e: $<S_e>/S_e = 35/26 \sim 1.3$ and $29.8/23.6 \sim 1.3$ for 1.0 keV electrons on glycine and valine, respectively (see Figs. 6.22 and 6.26 (a)). The deposited energy predicted by CASINO reproduces this behavior. Figure 6.28 (a) illustrates the energy distribution by depth of a 1.0 keV electron beam impinging on a 40 nm valine film. The sample is divided in 40 layers of 1 nm each. The beam crosses the first layers causing moderate damage, but its higher degradation rate occurs around z = 9 nm deep. This happens not only because this region is the one having the highest stopping power values, but also because of the high electron fluxes, as shown in the region between dashed bars in Fig. 6.28 (b) for a narrow beam. Electrons are repeatedly scattered in this region, which means that they may cross the same layer several times.

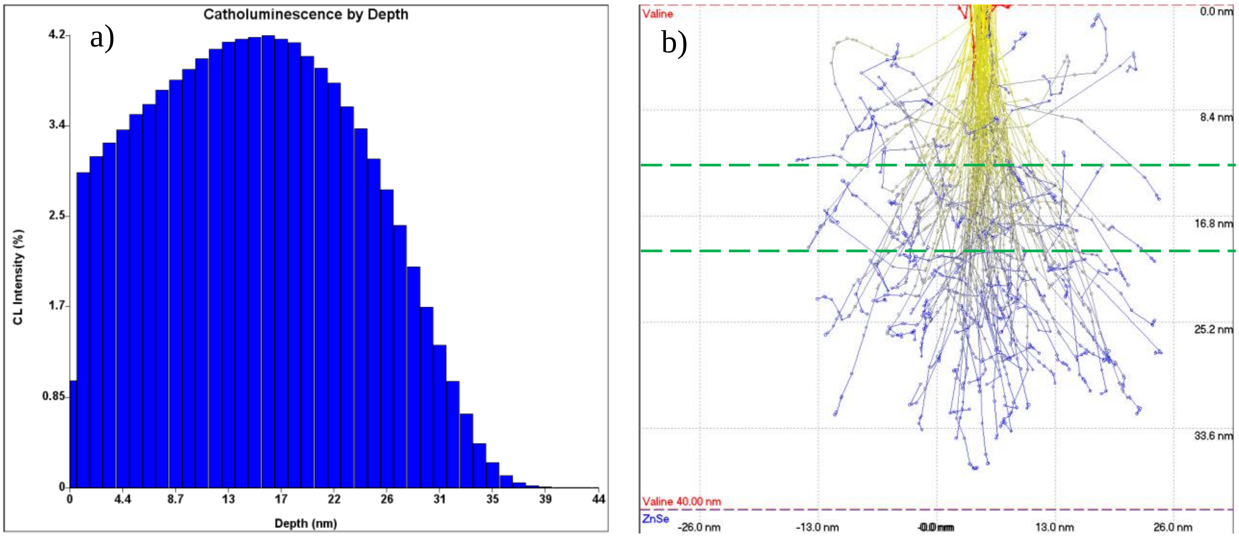

Figure 6.28: CASINO outputs. (a) cathodoluminescence dependence on depth of a valine film bombarded by 1 keV electrons. (b) Electron trajectories inside the sample; high energy: yellow,

low energy: blue; red lines refer to backscattered electrons. Green dashed lines highlight the central region, the one most destroyed by the beam.

Astrophysical implications

The finding that σ_d^{ap} varies linearly with S_e means that the amino acids damage is proportional to the deposited dose. This relationship can be used to predict destruction cross sections, if flux distributions are known (stopping power predictions are reliable within 5 -10 %). In particular, it is possible to calculate half-lives of organic materials exposed to cosmic irradiation. Equation 6.9 writes the partial destruction rate for each cosmic ray species j:

$$R_j = \int_0^\infty \frac{d\Phi}{dE}(E)\sigma_{d,j}^{ap}(E)dE \tag{6.9}$$

where E is the projectile kinetic energy, $\Phi_j(E)$ its flux density, and $\sigma_{d,j}^{ap}(E)$ its apparent destruction cross section. Equation 6.10 is the analytical expression for the GCR (galactic cosmic rays) flux densities [95].

$$\frac{d\Phi_j}{dE_m}(E_m) = C_j \frac{{E_m}^{0.3}}{(E_m + E_0)^3} \tag{6.10}$$

where E_m = E/m is the GCR energy per nucleon, E_0 is a constant parameter with maximum distribution between 200 and 600 MeV u^{-1}, we have adopted it to be 400 MeV u^{-1}. C_j is a coefficient that depends on the j^{th} GCR constituent abundance; the C_j coefficients are obtained from experimental data – as the GCR relative abundances [96] and absolute flux densities are known, Webber and Yushak (1993) [97] suggest that for $C_{j=H} = 9.42 \times 10^4$ ions $cm^{-2}s^{-1}sr^{-1}(MeV\ u^{-1})^{1.7}$.

For the current calculations, we have considered abundances and fluxes presented in table 1 and fig. 2 of Shen et al. (2004) [95]; the fluxes are multiplied by 2π sr, considering an isotropic GCR incidence on a spot located in a flat surface. This is an estimate for a material laying over a large body; in case of small grains where radiation from all directions could reach the material, the fluxes should be multiplied by 4π sr.

Amino acids half-lives in the ISM

For the main elemental constituents of GCR, the flux density dependence on E/m (Eq. (6.9)) is presented in Fig. 6.29 (a). The valine destruction rate dependence on projectile energy is shown in Figs. 6.29 (b) and the phenylalanine destruction rate dependence on E/m in 6.29 (c). For Val, H and He ions are responsible to the highest destruction rates at low GCR energies, while Fe ions dominate the molecular dissociation at high energies. For Phe, protons have the highest destruction rates for all energies, while He and Fe are the second most destructive projectiles for low and high energies, respectively.

The integral in Eq. (6.9) was performed from E/m = 10 keV/u up to 10 GeV/u. From the relative abundances reported [97], the C_j values integrated over 2π sr are determined for the main GCR species; a second integration, over the energies per nucleon, defines the absolute fluxes Φ_j (see Table 6.11). Table 6.11 also displays the partial and total destruction rates and half-lives for pure valine and phenylalanine samples.

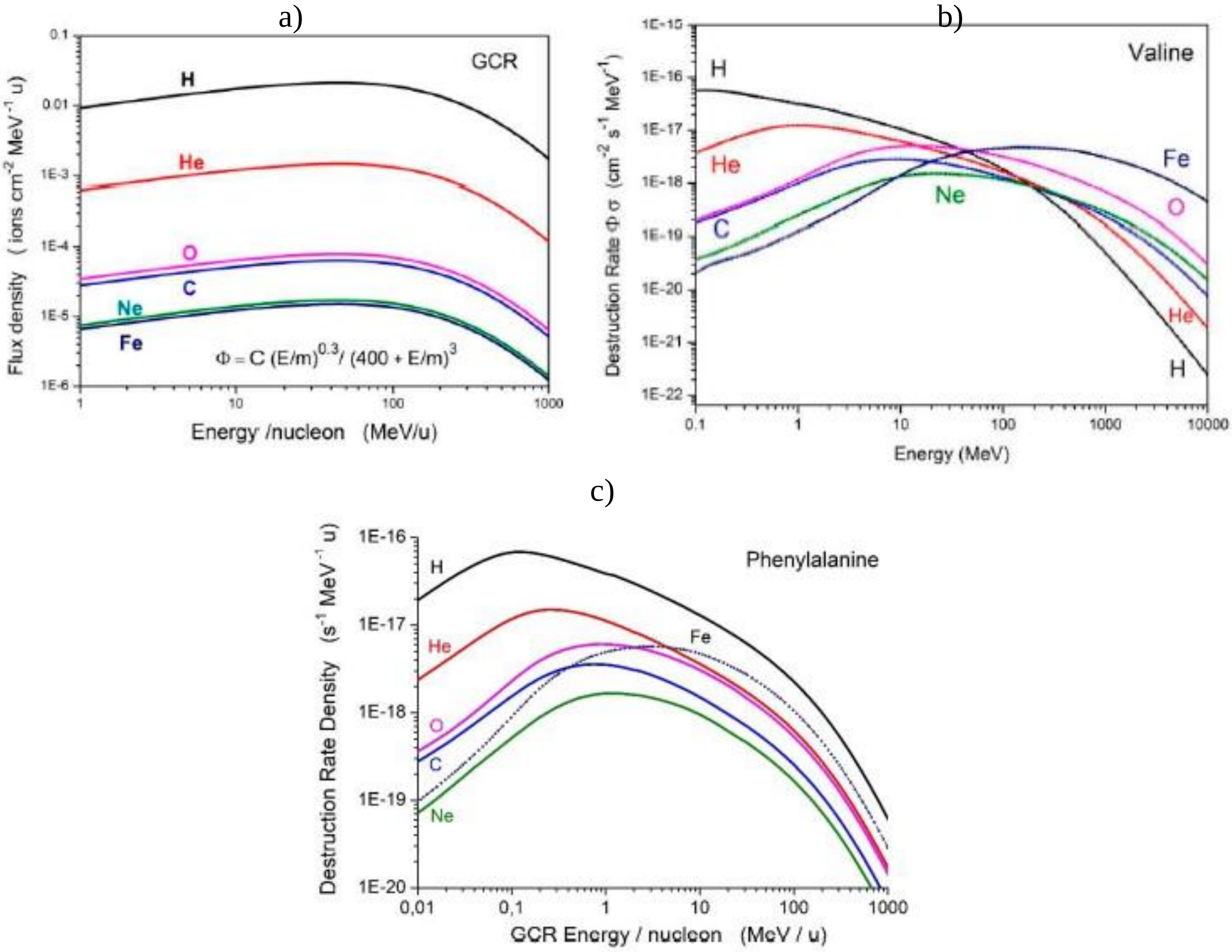
a)

b)

c)

Figure 6.29: (a) Shen et al. (2004) [95] predictions for galactic cosmic ray flux densities.

Destruction rate dependence on cosmic ray energies for the amino acids (b) valine [61] and (c) phenylalanine [51].

Table 6.11: Galactic cosmic ray j, its abundance, the C_j flux parameter, and the respective destruction rates, R_j, and half-lives, $\tau_{1/2}$, of valine and phenylalanine.

j	**GCR relative abundance**[1]	**2π C_j (10^3 ions cm^{-2} s^{-1} (MeV/u)$^{1.7}$)**	**GCR Φ_j (ions cm^{-2} s^{-1})**	**R_j (10^{-16} s^{-1})**		**$\tau_{1/2}$ = ln(2)/R_j (Ma)**	
				Val[2]	**Phe**[3]	**Val**[2]	**Phe**[3]
H	1.0×10^6	592	3.0	7.1	10.2	31	21.4
He	6.9×10^4	41	0.55	7.5	2.83	29	77.5
C	3000	1.9	0.011	8.8	1.13	25	194
O	3720	2.2	0.011	28	2.31	7.9	95.4
Ne	-	0.44	-	12	0.709	18	309
Fe	713	0.42	0.0016	170	4.11	1.2	53
Total				230	2.13	0.94	10.3

[1] Shen et al. (2004) [95]; [2] da Costa et al. (2020) [61]; [3] Mejía et al. (2021) [51].

Gerakines et al. (2012) [16] predicted a half-life of 14 million years for phenylalanine degraded at cryogenic temperatures in the dense ISM, while we have found ~ 10 million years for Phe at 300 K. This difference is mainly due to the material radioresistance dependence on temperature; see Fig. 10 of Mejía et al. (2021) [51]. Gerakines et al. (2012) [16] also estimated half-lives of glycine, alanine, and distinct mixtures of these amino acids with water ice; they have reported that half-lives are in the 11 – 19 Ma range. Vignoli Muniz et al. (2017) [19] have also found 10 Ma as the half-life of adenine, indicating that organic materials having similar atomic constitution behave analogously when exposed to GCR.

Amino acids half-lives in the SS

Figure 6.30 presents the dissociation rate distribution of glycine by solar cosmic rays as a function of the projectile energy per nucleon; data are based on $d^2\Phi/(d\Omega dE)$ experimental data relative to the orbit of Earth [98]. The ionic projectiles and their respective energy ranges considered to obtain $d\Phi_j/d\Omega$ and R_j are shown in Table 6.12. The presented Φ_j flux values (e.g., Bennett et al. (2013) [99]) are similar to the obtained $d\Phi_j/d\Omega$, so we have adopted $\Omega \sim 1$ sr in the dissociation rate calculations. Notice that, for ionic projectiles:

i) All over the energy range, H and He projectiles induce the highest glycine dissociation rates in the Solar System.

ii) At energy ~ 1 keV/u, dissociation rates induced by all elemental projectiles have their maximum values (solar wind with velocity of ~ 440 km s^{-1}).

iii) If the linear relationship for σ_d^{ap} also holds for the nuclear stopping power, S_n, the ion – nucleus contribution to molecular damage becomes non-negligible for O ions with energies below 2 keV/u, where the dissociation rate doubles. For Fe ions the dissociation rates increase a factor 5.8. Dotted lines in Fig. 6.30 represent the dependence on total stopping power contribution ($S_e + S_n$).

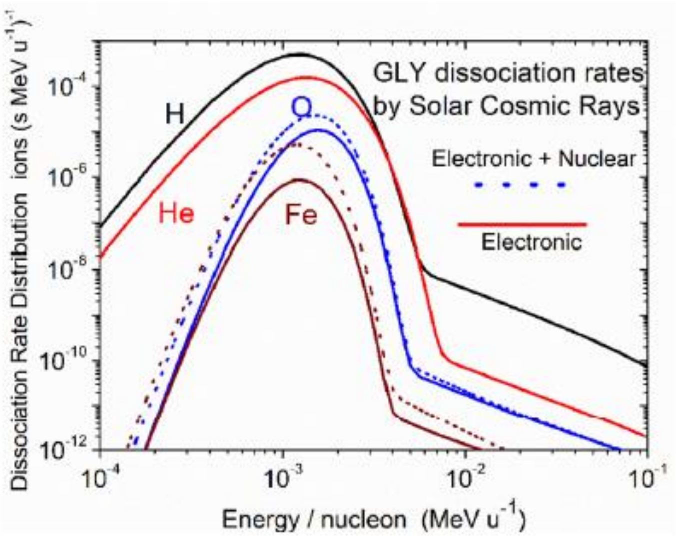

Figure 6.30: Glycine Destruction rate for solar ionic cosmic-ray species. Estimates from the relationship $\sigma_d^{ap} = a$ S and dΦ/dE are based on Mewaldt et al. (2001) [98] data; contribution due to S_e (solid lines) and to $S_e + S_n$ (dotted lines) are represented.

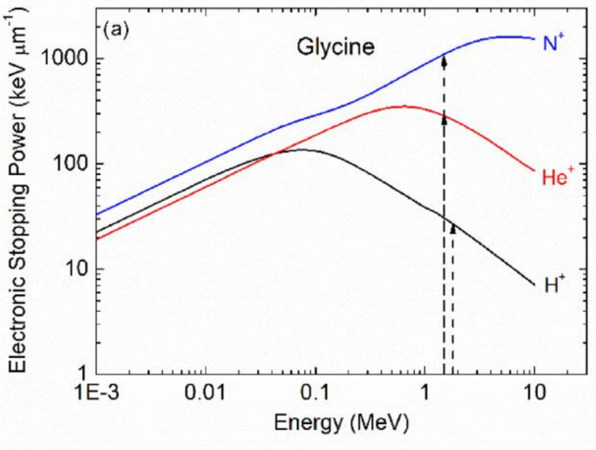

Figure 6.31: Electronic stopping power of H^+, He^+ and N^+ beams in glycine as a function of the projectile energy.

Figure 6.32 (a) shows the electrons solar wind density flux (e.g. Wang et al. (2012) [100]). Black squares are experimental data fitted with a kT = 10.1 eV Maxwellian distribution plus a decaying power function for high energies. The highest flux occur for E ~ 10 eV. Since the maximum stopping power for electrons on glycine occurs at 60 eV (Fig. 6.22), and considering that $\sigma_d^{ap} \leq a\ S_e$ holds for electron beams, then the maximum of the dissociation rate should be between 10 and 60 eV as presented in Fig. 6.32 (b).

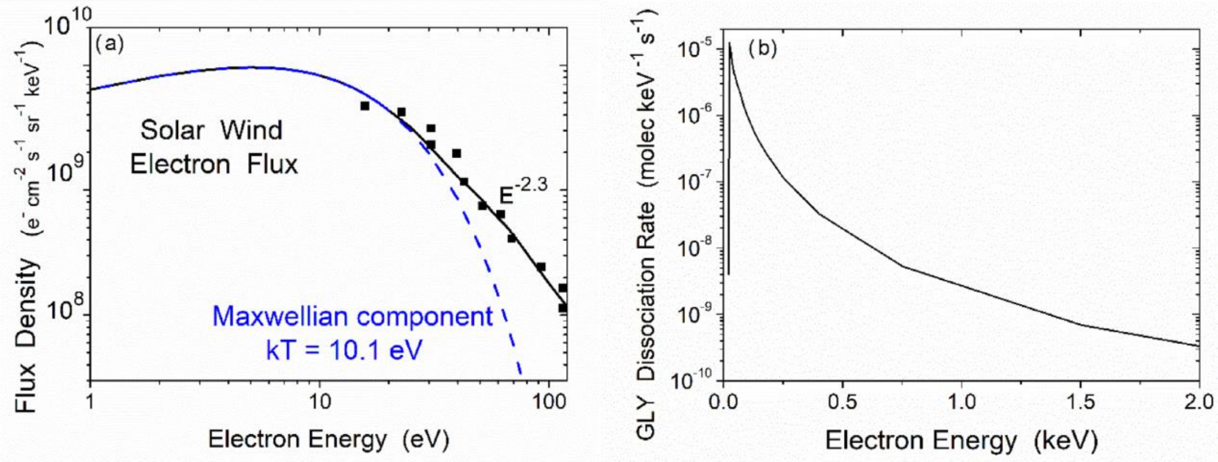

Figure 6.32: (a) Flux density of electrons constituent of the solar wind plasma, measured at 1 au from the Sun; kT = 10.1 eV Maxwellian distribution represented by the dashed line. High energy slope component $E^{-2.3}$ included at the end of solid line (Data from Lin et al (1972) [101]). (b) Glycine destruction rate dependence on energy of electrons at 1 au from the Sun: maximum value at region 25 – 100 eV.

Considering solar wind's most abundant projectiles and their respective fluxes, Table 6.12 displays the R_j and $\tau_{1/2}$ estimates for glycine at one astronomical unit of distance from the Sun. Concerning solar electrons, the half-life of glycine is about 4 days, with < 60 eV electrons being the main elements responsible for such quick destruction. This value should also be considered as an inferior limit, since experimental electron apparent destruction cross sections appear below the $\sigma_d^{ap} = a\ S_e$ curve.

Table 6.12: Solar wind species j, its energy, flux density and experimental flux, and the destruction rate and half-life results for glycine at 1 au from the Sun.

j	**Energy (keV)**	**$d\Phi_j/d\Omega$* (10^7 cm^{-2} s^{-1} sr^{-1})**	**Φ_j** (10^7 cm^{-2} s^{-1})**	**R_j (10^{-6} s^{-1})**	**$\tau_{1/2}$ (D)**
e^-	< 0.060	19	50	1.3	6.2
	0.06 – 0.10	1.1	2.1	0.43	19
	0.10 – 1.0	0.52	0.50	0.18	45
Total e^-		22	52	1.9	4.2
H	0.1 - 10	28	50	S_e 0.69	36
He	0.4 – 40	5.4	2.0	S_e 0.22	36
O	1.6 – 160	0.013	0.016	S_e 0.012 $S_e + S_n$ 0.024	670 330
Fe	5.6 – 560	0.0047	0.0093	S_e 7.4×10^{-4} $S_e + S_n$ 4.3×10^{-3}	11000 1900
Total				2.8	2.8

* Fitting of data from Mewaldt et al. (2001) [98]; ** Bennett et al. (2013) [99].

This prediction of glycine half-life in the Solar System is by far smaller than the values found by Pilling et al. (2014) [24] and Maté et al. (2015) [25]; they reported values between 8 – 10^4 million years, though for more distant locations (Mars and Titan). Even considering that cross sections change by at least a factor 2 when temperatures decrease, probably the huge difference between results lays on the fact that we are considering overestimated σ_d^{ap} values. Consequently, ~ 60 eV electrons swiftly destroy glycine because of their combined high flux and high destruction cross section.

7
Conclusions

This chapter summarizes the main conclusions drawn during the current work and opens perspectives for the continuity of this research line. They concern the study of: i) amino acid band strength - measurements and dependence on temperature; ii) radiolysis and sputtering - measurements and dependence on diverse projectiles as well as sample characteristics; and iii) half-life estimates for amino acids in the Interstellar Medium and in the Solar System.

7.1
Characterization of amino acids

Regarding A-value measurements for valine and phenylalanine selected bands, conclusions are:

i) Combination of infrared spectroscopy and profilometry is an adequate and accurate tool for A-value determination. Requirements are: sample not too thick for avoiding saturation of absorbance and sample not too thin for length determination.

ii) Valine relative A-values, with respect to its 948 cm^{-1} band, increase with the increasing beam fluence (see Table 6.3); this is an evidence that irradiation changes crystallographic properties of samples.

iii) Commercial ZnSe windows are excellent substrates for FTIR measurements: they have polished surfaces (appropriate to profilometry), are not hygroscopic and do not have characteristic peaks for most part of the mid-IR region. They block IR radiation from ~ 700 to 400 cm^{-1}.

iv) Amino acid’s film density may change according to the way it is prepared. Another analytical method needs to be employed for column density measurements.

About the sample characteristics’ dependence on temperature:

i) Sublimation rates of thin samples are higher than those of thick ones. We attribute this to their distinct morphology.

ii) The average sublimation rates increase parabolically with temperature, Fig. 7.1.

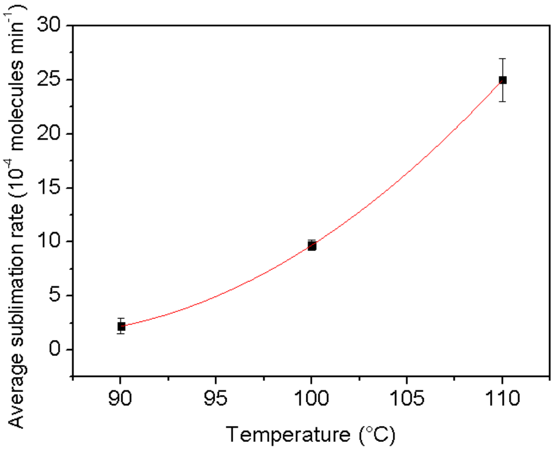

Figure 7.1: Valine sublimation rate dependence on oven temperature at atmospheric pressure.

iii) Absorbance band widths at 300 K are twice those at 40 K. We attribute this to Doppler effect.

iv) A_v increases with the increase of temperature. For instance, A_v of valine band 1408-1380 cm^{-1} increases from 2% to 45% (Fig. 6.7) when the sample temperature goes from 10 – 150 and 150 – 300 K, respectively;

v) No phase transition on the temperature excursion 300 → 40 → 400 → 40 → 300 K has been observed. Peak form and position are restored.

7.2

Radiolysis, sputtering and half-life predictions

Glycine, valine and phenylalanine were irradiated by MeV ion and keV electron beams for distinct conditions: different beam energies, projectile species and charges, sample temperatures and thicknesses. FTIR spectroscopy analysis provides the following conclusions:

i) Changing projectile species has no effect on the sample chemical modification, with exception of their destruction absolute cross sections that depend on the deposited dose.

ii) Radiolysis and sputtering are the phenomena responsible for the amino acids degradation - with the main reactions being decarboxylation and deamination [16, 33, 102]. Column densities decrease exponentially as a function of beam fluence. FTIR technique is not able to discriminate the effects of the two processes, yielding a single quantity that represents the sum of them, $\sigma_d^{ap} = \sigma_d + Y_0/N_0$.

iii) For MeV ion beams, it turns out that σ_d^{ap} is approximately proportional to the electronic stopping power and, consequently, to the absorbed dose. This relationship holds not only for various amino acids, but also for similar organic materials such as adenine (e.g., [16, 19]). It is known, however, that $\sigma_d^{ap} = aS_e^n$ with n = 1.0 is not valid for condensed gases, where values lay in-between $1.3 \leq n \leq 1.5$ [103, 104, 60];

iv) The apparent critical dose, D_0^{ap}, has been determined to be 10, 16, and 14.3 eV per molecule (at room temperature) for glycine, valine and phenylalanine, respectively. These data are in agreement with Maté et al. who measured, for 2 keV electrons on Glycine, $D_0^{ap} \sim 13$ eV/molec at cryogenic temperatures and ~ 7 eV/molec at room temperature.

v) The relationship $\sigma_d^{ap} = a\ S_e$ seems to be overestimated for keV electron data, so that σ_d^{ap} should be taken as an upper limit. Dependence on preparation and thickness of the sample should be investigated.

vi) While results reported for MeV ion beams show that σ_d^{ap} increases by a factor ~ 2 – 7 when the sample temperature decreases [16, 18], literature data of keV electron beams bombarding thin glycine reveal an opposite trend: σ_d^{ap} decreases by a factor 2 to 20 for samples at lower temperatures [25, 26]. Why this is so is under debate; probably the reason is due to the very different trajectory pattern between ion and electron projectiles inside solids. The current results of valine degradation by keV electrons agree with the literature, since we have found that cross sections at 10 K are 5 times smaller than the ones at room temperature;

vii) Experimental σ_d^{eff} values of keV electrons increase when the beam energy increases (at least in the range 60 – 1000 eV), because the number of molecules that can be processed in the sample increases with the beam energy. This is a result is an apparent contradiction with the Bethe and Joy-Luo predictions; however, they have calculated cross sections for binary collisions at specific energies, which is not the case for the presented data where the beam deposits all its energy inside the target.

viii) The obtained destruction cross sections of keV electrons decrease with the increase of sample thicknesses. This might be one of the reasons why pertinent data on literature are so disperse.

ix) Barnett et al. (2012) [21] concluded that CASINO underestimates the damage of keV electrons on pyrene. We have also observed that valine samples with thicknesses greater than the z_{max} predicted by CASINO were completely destroyed, which is an indication that, besides radiolysis, keV electrons also cause sputtering.

x) For five valine samples with different thicknesses, the sputtering yield, Y_0, for the beam 1.5 MeV N^+ is estimated to be around 1300 ± 700 molecules per impact, while the absolute destruction cross section, σ_d, is predicted to be $(7.0 \pm 3) \times 10^{-14}$ cm^2 (see Fig. 6.19).

xi) Preliminary results with multi-charged beams show that experimental data do not agree qualitatively with σ_d^{ap} predictions based on Joy-Luo or CasP calculations. The finding that $\sigma_d^{ap} \sim q^4$ indicates that for charge states $q > 2$ sputtering damaging effects dominate over the radiolysis ones and yields $Y_0 \sim 100$ precursors per impact for 1.5 MeV N^+ beam. This yield is one order of magnitude lower than the one estimated from varying sample thicknesses.

xii) If the incident projectile charge is different from the equilibrium charge, multi-charged beam analysis predicts that radiolysis damage rate varies in the bulk along the characteristic relaxation length λ_q.

xiii) Since measurements were performed with thick targets, molecular beam data results are inconclusive (remember that after a few layers inside the material, the projectile N_2^+ breaks apart and causes the same effects of two N^+ projectiles).

xiv) The predicted half-lives for valine and phenylalanine in the ISM are 1 and 10 million years, respectively. Gerakines et al. (2012) [16] and Vignoli Muniz et al. (2017) [19] found results similar to the latter (both at low temperatures: 14 million years for Phe and 10 million years for adenine, respectively). This difference of one order of magnitude points towards a mistake in the valine calculations.

xv) Considering the σ_d^{ap} upper limit for energetic electrons, glycine located at one astronomical unit from the Sun has a predicted half-life of at least 2.8 days.

xvi) The two conclusions above refer to half-lives calculated for pure samples, though it is possible to estimate values for real cases given the composition of the mixed material. For instance, CASINO predicts that on a sample constituted by a SiO_2 substrate with a 40 nm mixture of ice H_2O:Val (100:1), and covered by 15 nm of icy CO_2, only 2.3% of the energy of a 2 keV electron beam goes to the destruction of valine.

xvii) D_0 calculated doses are much higher than lethal radiotherapy doses, around 10 MGy and 10 – 100 Gy, respectively. However, it is important to keep in mind that the latter is the quantity necessary to stop biological functions by destroying small fractions of DNA, while the former represents the value needed to degrade about 63% of precursor molecules.

xviii) Main exogenesis models on the origins of life propose that prebiotic molecules, formed in the interstellar medium, have been transported to Earth. To calculate the survival probability for this long journey, dissociation rates need to be known, which in turn requires the knowledge of destruction cross sections relative to all ionizing radiation, covering a large energy range, and at different environment temperatures. Results obtained in the current work contribute to this huge database and to set-up algorithms for modelling.

7.3
Perspectives

For the continuity of this research line, it is necessary to carry up new experiments and calculations, in particular:

i) To improve and repeat measurements with multi-charged beams.

ii) To employ other techniques to measure directly sputtering yields (RBS combined with FTIR, for instance).

iii) To increase the complexity of the analyzed materials (peptides, sugars, PAHs, nitrogenous bases, DNA etc…).

iv) To keep improving the CASINO-extended model in order to better describe contributions of sputtering and sample temperature.

v) To consider other approaches for electron transport modeling, PENELOPE for instance [105].

vi) To evaluate the possible contributions to clarify Salam's transitions.

Bibliography

[1] CRONIN, J. R. and MOORE, C. B. (1971). Amino Acid Analyses of the Murchison, Murray, and Allende Carbonaceous Chondrites. *Science* **172** 1327–9.

[2] WOLMAN, Y., HAVERLAND, W. J. and MILLER, S. L. (1972). Nonprotein Amino Acids from Spark Discharges and Their Comparison with the Murchison Meteorite Amino Acids. *Proceedings of the National Academy of Sciences* **69** 809–11.

[3] CRONIN, J. R. and MOORE, C. B. (1976). Amino acids of the Nogoya and Mokoia carbonaceous chondrites. *Geochimica et Cosmochimica Acta* **40** 853–7.

[4] ELSILA, J. E., GLAVIN, D. P. and DWORKIN, J. P. (2009). Cometary glycine detected in samples returned by Stardust. *Meteoritics & Planetary Science* **44** 1323–30.

[5] ALTWEGG, K., BALSIGER, H., BAR-NUN, A., BERTHELIER, J.-J., BIELER, A., BOCHSLER, P., BRIOIS, C., CALMONTE, U., COMBI, M. R., COTTIN, H., DE KEYSER, J., DHOOGHE, F., FIETHE, B., FUSELIER, S. A., GASC, S., GOMBOSI, T. I., HANSEN, K. C., HAESSIG, M., JÄCKEL, A., KOPP, E., KORTH, A., LE ROY, L., MALL, U., MARTY, B., MOUSIS, O., OWEN, T., RÈME, H., RUBIN, M., SÉMON, T., TZOU, C.-Y., HUNTER WAITE, J. and WURZ, P. (2016). Prebiotic chemicals—amino acid and phosphorus—in the coma of comet 67P/Churyumov-Gerasimenko. *Sci. Adv.* **2** e1600285.

[6] CRUZ-DIAZ, G. A., ERICKSON, S. E., SILVEIRA, E. F. da, RICCA, A., DE BARROS, A. L. F., DA COSTA, C. A. P., PEREIRA, R. C. and MATTIODA, A. L. (2019). PAH Products and Processing by Different Energy Sources. *ApJ* **882** 44.

[7] IGLESIAS-GROTH, S., CATALDO, F., URSINI, O. and MANCHADO, A. (2010). Amino acids in comets and meteorites: stability under gamma radiation and preservation of the enantiomeric excess: Amino acids in comets and meteorites. *Monthly Notices of the Royal Astronomical Society* no-no.

[8] CATALDO, F., ANGELINI, G., IGLESIAS-GROTH, S. and MANCHADO, A. (2011). Solid state radiolysis of amino acids in an astrochemical perspective. *Radiation Physics and Chemistry* **80** 57–65.

[9] CATALDO, F., RAGNI, P., IGLESIAS-GROTH, S. and MANCHADO, A. (2011). A detailed analysis of the properties of radiolyzed proteinaceous amino acids. *J Radioanal Nucl Chem* **287** 903–11.

[10] SAGAN, C. and KHARE, B. N. (1979). Tholins: organic chemistry of interstellar grains and gas. *Nature* **277** 102–7.

[11] Strazzulla, G. (1997). Ion irradiation: Its relevance to the evolution of complex organics in the outer solar system. *Advances in Space Research* **19** 1077–84.

[12] Dück, P., Treu, W., Galster, W., Fröhlich, H. and VOLT, H. HEAVY ION INDUCED DESORPTION OF ORGANIC COMPOUNDS. 5.

[13] Salehpour, M., Fishel, D. L. and Hunt, J. E. (1988). Nonlinear effects in desorption of valine with fast incident molecular ions. *Phys. Rev. B* **38** 12320–8.

[14] Barros Leite, C. V., da Silveira, E. F., Jeronymo, J. M. F., Pinho, R. R., Baptista, G. B., Schweikert, E. A. and Park, M. A. (1992). Secondary-ion emission from phenylalanine induced by atomic and molecular MeV ion beams. *Phys. Rev. B* **45** 12218–21.

[15] Salehpour, M., Håkasson, P. and Sundqvist, B. (1984). Damage cross sections for fast heavy ion induced desorption of biomolecules. *Nuclear Instruments and Methods in Physics Research Section B: Beam Interactions with Materials and Atoms* **2** 752–6.

[16] Gerakines, P. A., Hudson, R. L., Moore, M. H. and Bell, J.-L. (2012). In situ measurements of the radiation stability of amino acids at 15–140 K. *Icarus* **220** 647–59.

[17] Pilling, S., Mendes, L. A. V., Bordalo, V., Guaman, C. F. M., Ponciano, C. R. and da Silveira, E. F. (2013). The Influence of Crystallinity Degree on the Glycine Decomposition Induced by 1 MeV Proton Bombardment in Space Analog Conditions. *Astrobiology* **13** 79–91.

[18] Portugal, W., Pilling, S., Boduch, P., Rothard, H. and Andrade, D. P. P. (2014). Radiolysis of amino acids by heavy and energetic cosmic ray analogues in simulated space environments: α-glycine zwitterion form. *Monthly Notices of the Royal Astronomical Society* **441** 3209–25.

[19] Vignoli Muniz, G. S., Mejía, C. F., Martinez, R., Auge, B., Rothard, H., Domaracka, A. and Boduch, P. (2017). Radioresistance of Adenine to Cosmic Rays. *Astrobiology* **17** 298–308.

[20] Howitt, D. G. (1974). *The measurement of radiation damage in organic materials in the range of electron energy between 200 keV and 650 keV.*

[21] Barnett, I. L., Lignell, A. and Gudipati, M. S. (2012). Survival Depth Of Organics In Ices Under Low-Energy Electron Radiation ($\leqslant$2 keV). *ApJ* **747** 13.

[22] Drouin, D., Couture, A. R., Joly, D., Tastet, X., Aimez, V. and Gauvin, R. (2007). CASINO V2.42—A Fast and Easy-to-use Modeling Tool for Scanning Electron Microscopy and Microanalysis Users. *Scanning* **29** 92–101.

[23] MATÉ, B., TANARRO, I., MORENO, M. A., JIMÉNEZ-REDONDO, M., ESCRIBANO, R. and HERRERO, V. J. (2014). Stability of carbonaceous dust analogues and glycine under UV irradiation and electron bombardment. *Faraday Discuss.* **168** 267–85.

[24] PILLING, S., NAIR, B. G., ESCOBAR, A., FRASER, H. and MASON, N. (2014). The temperature effect on the glycine decomposition induced by 2 keV electron bombardment in space analog conditions. *Eur. Phys. J. D* **68** 58.

[25] MATÉ, B., TANARRO, I., ESCRIBANO, R., MORENO, M. A. and HERRERO, V. J. (2015). Stability Of Extraterrestrial Glycine Under Energetic Particle Radiation Estimated From 2 Kev Electron Bombardment Experiments. *ApJ* **806** 151.

[26] SOUZA-CORRÊA, J. A., DA COSTA, C. A. P. and DA SILVEIRA, E. F. (2019). Compaction and Destruction Cross-Sections for α-Glycine from Radiolysis Process via 1.0 keV Electron Beam as a Function of Temperature. *Astrobiology* **19** 1123–38.

[27] EVANS, N. L., BENNETT, C. J., ULLRICH, S. and KAISER, R. I. (2011). On The Interaction Of Adenine With Ionizing Radiation: Mechanistical Studies And Astrobiological Implications. *ApJ* **730** 69.

[28] FOTI, A. M., BARATTA, G. A., LETO, G. and STRAZZULLA, G. (1991). Molecular Alteration and Carbonization of Glycine by Ion Irradiation. *Europhys. Lett.* **16** 201–4.

[29] FOTI, A. M., BARATTA, G. A., LETO, G. and STRAZZULLA, G. (1991). Vibrational spectroscopy of as-prepared and ion-irradiated glycine films. *Infrared Physics* **31** 511–6.

[30] HUANG, W., YU, Z. and ZHANG, Y. (1998). Reactions of solid glycine induced by keV ion irradiation. *Chemical Physics* **237** 223–31.

[31] HUANG, W., WANG, X., YU, Z. and ZHANG, Y. (1998). Research into keV N+ irradiated glycine. *Nuclear Instruments and Methods in Physics Research Section B: Beam Interactions with Materials and Atoms* **140** 373–9.

[32] HUANG, W., JIANWEI, H., XIANGQING, W., YU ZENGLIANG and YUHENG, Z. (1998). keV ion irradiation of solid glycine: an EPR study. *Nuclear Instruments and Methods in Physics Research Section B: Beam Interactions with Materials and Atoms* **140** 137–42.

[33] MESHITSUKA, G., SHINDO, K., MINEGISHI, A., SUGURO, H. and SHINOZAKI, Y. (1964). Radiolysis of Solid Glycine. *BCSJ* **37** 928–30.

[34] LAGO, A. F., COUTINHO, L. H., MARINHO, R. R. T., NAVES DE BRITO, A. and DE SOUZA, G. G. B. (2004). Ionic dissociation of glycine, alanine, valine and proline as induced by VUV (21.21 eV) photons. *Chemical Physics* **307** 9–14.

[35] JUNK, G. The Mass Spectra of the a-Amino Acids. 7.

[36] BEYNON, J. H., LESTER, G. R. and WILLIAMS, A. E. (1959). Some Specific Molecular Rearrangements in the Mass Spectra of Organic Compounds. *J. Phys. Chem.* **63** 1861–8.

[37] PERNET, A., PILMÉ, J., PAUZAT, F., ELLINGER, Y., SIROTTI, F., SILLY, M., PARENT, Ph. and LAFFON, C. (2013). Possible survival of simple amino acids to X-ray irradiation in ice: the case of glycine. *A&A* **552** A100.

[38] CATALDO, F., URSINI, O., ANGELINI, G., IGLESIAS-GROTH, S. and MANCHADO, A. (2011). Radiolysis and radioracemization of 20 amino acids from the beginning of the Solar System. *Rend. Fis. Acc. Lincei* **22** 81–94.

[39] BARRET, G. C. and ELMORE, D. T. (1998). *Amino acids and peptides*. Cambridge University press.

[40] NELSON, D. L. and COX, M. M. (2005). *Lehninger principles of biochemistry*. Ed. New York: Freeman.

[41] ATKINS, P. W. and DE PAULA, J. (2008). *Físico-Química*. vol 1 LTC, Rio de Janeiro.

[42] DA COSTA, C. A. P. (2016). *Radiólise de valina por íons de MeV analisada por espectroscopia no infravermelho*. PUC-Rio, Rio de Janeiro.

[43] SALAM, A. (1992). Chirality, phase transitions and their induction in amino acids. *PHYSICS LETTERS B* **288** 8.

[44] WANG, W., YI, F., NI, Y., ZHAO, Z., JIN, X. and TANG, Y. Parity Violation of Electroweak Force in Phase Transitions of Single Crystals of D- and L-Alanine and Valine. 16.

[45] KOZLOVA, S. G. and GABUDA, S. P. (2017). Thermal properties of Zn2(C8H4O4)2•C6H12N2 metal-organic framework compound and mirror symmetry violation of dabco molecules. *Sci Rep* **7** 11505.

[46] MATÉ, B., RODRIGUEZ-LAZCANO, Y., GÁLVEZ, Ó., TANARRO, I. and ESCRIBANO, R. (2011). An infrared study of solid glycine in environments of astrophysical relevance. *Phys. Chem. Chem. Phys.* **13** 12268.

[47] GUAN, Y. Y., FRAY, N., COLL, P., MACARI, F., CHAPUT, D., RAULIN, F. and COTTIN, H. (2010). UVolution: Compared photochemistry of prebiotic organic compounds in low Earth orbit and in the laboratory. *Planetary and Space Science* **58** 1327–46.

[48] HOLTOM, P. D., BENNETT, C. J., OSAMURA, Y., MASON, N. J. and KAISER, R. I. (2005). A Combined Experimental and Theoretical Study on the Formation of the Amino Acid Glycine (NH_2CH_2COOH) and Its Isomer ($CH_3NHCOOH$) in Extraterrestrial Ices. *ApJ* **626** 940–52.

[49] KUMAR, S. (2011). Spectroscopic studies of valine and leucine molecules a comparative study. *Vibrational Spectroscopy* **39** 4996–9.

[50] FAÇANHA FILHO, P. F., FREIRE, P. T. C., LIMA, K. C. V., MENDES FILHO, J., MELO, F. E. A. and PIZANI, P. S. (2008). High temperature Raman spectra of L-leucine crystals. *Braz. J. Phys.* **38** 131–7.

[51] MEJÍA, C., DA COSTA, C. A. P., IZA, P. and DA SILVEIRA, E. F. (2021). Irradiation of phenylalanine at 300 K by MeV ions. *Astrobiology* **submitted**.

[52] WOLFE, W. L. (1997). *Introducing to Imaging Spectrometers*. Washington: SPIE Press.

[53] GRIFFITHS, P. R. and HASETH, J. A. (2007). *Fourier Transform Infrared Spectrometry*. Nova Jersey: Wiley-Interscience.

[54] DA COSTA, C. A. P., SOUZA-CORRÊA, J. A. and DA SILVEIRA, E. F. (2021). Infrared analysis of Glycine dissociation by MeV ions and keV electrons. *Monthly Notices of the Royal Astronomical Society* **502** 2105–19.

[55] PÉREZ, Y. C. (2017). *Impactos de micrometeoritos com a superfícia da Terra: simulações mediante ablação por laser*. PUC-Rio, Rio de Janeiro.

[56] DA COSTA, C. A. P. and DA SILVEIRA, E. F. (2019). Valine infrared absorbance at cryogenic temperatures. *Low Temperature Physics* **45** 649–55.

[57] ANON. (https://www.ganil-spiral2.eu/). Grand Accélérateur National d'Ions Lourds.

[58] HOVINGTON, P., DROUIN, D. and GAUVIN, R. (1997). CASINO.Available at http://www.gel.usherbrooke.ca/casino.

[59] DEMERS, H., POIRIER-DEMERS, N., COUTURE, A. R., JOLY, D., GUILMAIN, M., DE JONGE, N. and DROUIN, D. (2011). Three-dimensional electron microscopy simulation with the CASINO Monte Carlo software. *Scanning* **33** 135–46.

[60] MEJÍA, C. F., DE BARROS, A. L. F., BORDALO, V., DA SILVEIRA, E. F., BODUCH, P., DOMARACKA, A. and ROTHARD, H. (2013). Cosmic ray–ice interaction studied by radiolysis of 15 K methane ice with MeV O, Fe and Zn ions. *Monthly Notices of the Royal Astronomical Society* **433** 2368–79.

[61] DA COSTA, C. A. P., MUNIZ, G. S. V., BODUCH, P., ROTHARD, H. and SILVEIRA, E. F. da. (2020). Valine Radiolysis by H+, He+, N+, and S15+ MeV Ions. *IJMS* **21** 1893.

[62] JOY, D. C. and LUO, S. (1989). An empirical stopping power relationship for low-energy electrons. *Scanning* **11** 176–80.

[63] DA COSTA, C. A. P. and DA SILVEIRA, E. F. (2021). Infrared analysis of Valine degradation by keV electrons. Measurements and CASINO-extended model predictions. *submitted to MNRAS*.

[64] PEREIRA, R. C., DE BARROS, A. L. F., DA COSTA, C. A. P., OLIVEIRA, P. R. B., FULVIO, D. and DA SILVEIRA, E. F. (2020). Ion irradiation of acetylene ice in the ISM and the outer Solar system: laboratory simulations. *Monthly Notices of the Royal Astronomical Society* **495** 40–57.

[65] ANON. (1989). *The Merck Index*. Merck & Co. Inc.: Rahway, NJ.

[66] BALUJA, S. and GODVANI, J. (2008). Thermodynamics and acoustical studies of aqueous solutions of some amino acids. *Thermodynamics and acoustical studies of aqueous solutions of some amino acids.* **30** 81–5.

[67] GALLEANO, M., BOVERIS, A. and PUNTARULO, S. (2008). Understanding the Clausius–Clapeyron Equation by Employing an Easily Adaptable Pressure Cooker. *J. Chem. Educ.* **85** 276.

[68] EISBERG, R. M. and RESNICK, R. (1974). *Quantum physics of atoms, molecules, solids, nuclei and particles*. J. Wiley.

[69] GOMEZ-ZAVAGLIA, A. and FAUSTO, R. Low-temperature solid-state FTIR study of glycine, sarcosine and N,N-dimethylglycine: observation of neutral forms of simple a-amino acids in the solid state. 8.

[70] RODRÍGUEZ-LAZCANO, Y. (2012). Solid L-α-alanine Spectroscopic properties and theoretical calculations. 10.

[71] WONG, Y. T. A., TOH, S. Y., DJURICANIN, P. and MOMOSE, T. (2015). Conformational composition and population analysis of b-alanine isolated in solid parahydrogen. *Journal of Molecular Spectroscopy* 9.

[72] TAMULIENĖ, J., ROMANOVA, L., VUKSTICH, V., PAPP, A., BALIULYTĖ, L. and SNEGURSKY, A. (2018). ON THE INFLUENCE OF LOW-ENERGY IONIZING RADIATION ON THE AMINO ACID MOLECULE: VALINE CASE. *Lith. J. Phys.* 14.

[73] ZIEGLER, J. F., ZIEGLER, M. D. and BIERSACK, J. P. (2010). SRIM – The stopping and range of ions in matter (2010). *Nuclear Instruments and Methods in Physics Research Section B: Beam Interactions with Materials and Atoms* **268** 1818–23.

[74] CHUSUEI, C. C. and GOODMAN, D. W. (2003). *Encyclopedia of physical science and technology. X-ray Photoelectron Spectroscopy*.

[75] SEPERUELO DUARTE, E., DOMARACKA, A., BODUCH, P., ROTHARD, H. and DARTOIS, E. (2010). Laboratory simulation of heavy-ion cosmic-ray interaction with condensed CO. 7.

[76] Wittkower, A. B. (1973). EQUILIBRIUM-CHARGE-STATE DISTRIBUTIONS OF ENERGETIC IONS (Z ~ 2) IN GASEOUS AND SOLID MEDIA. **5** 54.

[77] Grande, P. L. and Schiwietz, G. (1998). Impact-parameter dependence of the electronic energy loss of fast ions. *Phys. Rev. A* **58** 3796–801.

[78] Bethe, H. A., Ashkin, J. and et al. (1953). Experimental nuclear physic.

[79] Betz, H.-D. (1972). Charge state and charge-changing cross sections of fast heavy ions penetrating through gaseous and solid media.

[80] Toapanta, P. D. I. (2006). *Extensão Do Modelo De Traço Nuclear Para Descrever A Dessorção Iônica: Aplicação Aos Agregados De Água*. PUC-Rio, Rio de Janeiro.

[81] Niggas, A., Creutzburg, S., Schwestka, J., Wöckinger, B., Gupta, T., Grande, P. L., Eder, D., Marques, J. P., Bayer, B. C., Aumayr, F., Bennett, R. and Wilhelm, R. A. (2021). Peeling graphite layer by layer reveals the charge exchange dynamics of ions inside a solid. *Commun Phys* **4** 180.

[82] Nastasi, M., Michael, N., Mayer, J., Hirvonen, J. K. and James, M. (1996). *Ion-solid interactions: fundamentals and applications*. Cambridge University Press.

[83] Montenegro, E. C., Cruz, S. A. and Vargas-Aburto, C. (1982). A universal equation for the electronic stopping of ions in solids. *Physics Letters A* **92** 195–202.

[84] Heckman, H. H., Hubbard, E. L. and Simon, W. G. (1963). Electronic Charge Distributions for Heavy Ions at High Velocities. *Phys. Rev.* **129** 1240–9.

[85] Bohr, N. Velocity-Range Relation for Fission Fragments. 6.

[86] Mejía, C., de Barros, A. L. F., Rothard, H., Boduch, P. and da Silveira, E. F. (2020). Radiolysis of Ices by Cosmic-Rays: CH_4 and H_2O Ices Mixtures Irradiated by 40 MeV ^{58}Ni $^{11+}$ Ions. *ApJ* **894** 132.

[87] Schmidt-Böcking, H., Ramm, U., Kraft, G., Ullrich, J., Berg, H., Kelbch, C., Olson, R. E., Dubois, R., Hagmann, S. and Jiazhen, F. (1992). Delta-electron emission in fast heavy ion atom collisions. *Advances in space research* 7–15.

[88] Berger, M. J., Coursey, J. S., Zucker, M. A. and Chang, J. (2005). ESTAR - NIST.Available at https://physics.nist.gov/PhysRefData/Star/Text/ESTAR.htm.

[89] TAN, Z., XIA, Y., ZHAO, M. and LIU, X. (2006). Electron stopping power and inelastic mean free path in amino acids and protein over the energy range of 20–20,000 eV. *Radiat Environ Biophys* **45** 135–43.

[90] ANDRADE, D. P. P., DE BARROS, A. L. F., PILLING, S., DOMARACKA, A., ROTHARD, H., BODUCH, P. and DA SILVEIRA, E. F. (2013). Chemical reactions induced in frozen formic acid by heavy ion cosmic rays. *Monthly Notices of the Royal Astronomical Society* **430** 787–96.

[91] SOUZA-CORRÊA, J. A. and DA SILVEIRA, E. F. (2021). Space Weathering: Processing Velocities in Organic Materials as a Function of Electron Beam Energies. Solar Electron Erosion Rate Application. *Astrobiology submitted*.

[92] BERGER, M. J. and SELTZER, S. M. (1984). Stopping Power for Electrons and Positrons.

[93] HEREDIA-AVALOS, S. and GARCIA-MOLINA, R. (2007). Reduction of the energy loss of swift molecular ions in solids due to vicinage effects in the charge state. *Phys. Rev. A* **76** 032902.

[94] BRANDT, W., RATKOWSKI, A. and RITCHIE, R. H. (1974). Energy Loss of Swift Proton Clusters in Solids. *Phys. Rev. Lett.* **33** 1325–8.

[95] SHEN, C. J., GREENBERG, J. M., SCHUTTE, W. A. and VAN DISHOECK, E. F. (2004). Cosmic ray induced explosive chemical desorption in dense clouds. *A&A* **415** 203–15.

[96] MEYER, J.-P., DRURY, L. O. C. and ELLISON, D. C. (1998). A cosmic-ray composition controlled by volability and A/Q ratio. SNR shock acceleration of gas and dust. The Advanced Compositions Explorer Mission.

[97] WEBBER, W. R. and YUSHAK, S. M. (1983). A measurement of the energy spectra and relative abundance of the cosmic-ray H and He isotopes over a broad energy range. *ApJ* **275** 391.

[98] MEWALDT, R. A. and ET AL. (2001). Solar and Galactic Composition. **598** 165.

[99] BENNETT, C. J., PIRIM, C. and ORLANDO, T. M. (2013). Space-Weathering of Solar System Bodies: A Laboratory Perspective. *Chem. Rev.* **113** 9086–150.

[100] WANG, L., LIN, R. P., SALEM, C., PULUPA, M., LARSON, D. E., YOON, P. H. and LUHMANN, J. G. (2012). Quiet-Time Interplanetary ~2-20 Kev Superhalo Electrons At Solar Minimum. *ApJ* **753** L23.

[101] LIN, R. P., ANDERSON, K. A. and CLINE, T. L. (1972). Detection of Interplanetary Electrons from 18 keV to 1.8 MeV during Solar Quiet Times. *Phys. Rev. Lett.* **29** 1035–8.

[102] GERAKINES, P. A. and HUDSON, R. L. (2013). Glycine's radiolytic destruction in ices: first in situ laboratory measurements for Mars. *Astrobiology* 647–55.

[103] DE BARROS, A. L. F., BORDALO, V., SEPERUELO DUARTE, E., F DA SILVEIRA, E., DOMARACKA, A., ROTHARD, H. and BODUCH, P. (2011). Cosmic ray impact on astrophysical ices: laboratory studies on heavy ion irradiation of methane. *A&A* **531** A160.

[104] ANDRADE, D. P. P., DE BARROS, A. L. F., PILLING, S., DOMARACKA, A., ROTHARD, H., BODUCH, P. and DA SILVEIRA, E. F. (2013). Chemical reactions induced in frozen formic acid by heavy ion cosmic rays. *Monthly Notices of the Royal Astronomical Society* **430** 787–96.

[105] SALVAT, F., FERNÁNDEZ-VAREA, J. M. and SEMPAU, J. Penelope-2006: A Code System for Monte Carlo Simulation of Electron and Photon Transport. 293.